DISS. ETH Nr. 24376

Heat Treatment Simulation and Experimental Investigation of Thermal Distortion with a Special Focus on Fineblanked Parts

A thesis submitted to attain the degree of
DOCTOR OF SCIENCE OF ETH ZURICH
(Dr. sc. ETH Zurich)

presented by

Maurice Nadim Peterli

MSc in Mechanical Engineering

born on 13.08.1987

citizen of Wil, St.Gallen

accepted on the recommendation of

Prof. Dr. P. Hora, examiner
Prof. Dr.-Ing. W. Volk, co-examiner

2017

Dedicated to my beloved grandparents J.-J. & E. Peterli

Acknowledgements

I would like to express my deepest gratitude for my advisor and Professor Dr. Pavel Hora for the trust placed in me and the opportunity to perform my research and write this theses at the Institute for Virtual Manufacturing at ETH Zürich. His continuous support for my project was very much appreciated.
In addition, I would like to thank my co-examiner Prof. Dr. W. Volk for his valuable input and my advisor and post-doc Dr. Niko Manopulo for his guidance through out my time at the institute. Further, thanks to my students for their help: Minh-Trung Truong for his contribution during the measurement and optimisation of thermal material data and Sebastian Hirsiger for his assistance in developing a quenching experiment for sheet metal. I would also like to thank my colleges for an inspiring and uplifting environment that I will never forget. Finally, many thanks to my friends and family, especially Judith Wemmer for her constant encouragement and support.

Zürich, Juni 2017
Maurice Peterli

Abstract

Most fineblanked components undergo some sort of heat treatment in order to achieve desired mechanical properties. At the same time it causes unwanted changes in size and shape of the workpiece leading to subsequent working steps on tools or parts. The extent of this thermal distortion depends on many factors such as material, geometry, type of treatment and treatment conditions. Thus, accurate numerical distortion prediction has a high complexity but can potentially save time and costs of reworks on manufacturing tools. Although the present work has a special focus on through-hardening processes, developed methods are applicable to other heat treatments, such as case hardening, with some adjustments. The goal is to bring thermal distortion prediction for fineblanked parts to a level where it can be used to reduce the amount of reworks on tools and parts.

In a first step, mechanical and thermal material properties of through-hardenable C60E steel are characterised. The yield curve, anisotropy and continuous cooling temperature (CCT) diagram are experimentally determined. Additionally, a newly developed end quench experiment for sheet metal, a modification of the well-known Jominy-experiment, is used to characterise hardenability. By recording the temperature history during quenching with an infrared camera, the modified Jominy approach can also be used to validated thermal material data in finite element simulations.

Subsequently, several experiment series are carried out to find the major influencing factors on thermal distortion, such as residual stresses from the forming or bending step, geometry and batching. All parts are measured before and after their treatment with digital image correlation technique and are then compared with their target geometry. In order to differentiate between stochastic fluctuations and deterministic relationships, the results are statistically analysed. Opposed to bending operations, which influence distortion results, pure fineblanking shows no significant change in distortion. As a consequence the blanking operation may be neglected for distor-

tion prediction. The observable orientation dependency during quenching with a flat, disk-like specimen could not be reproduced with another similar geometry. An additional experiment indicates the distortion reduction capabilities of batching during quenching. Two of the investigated geometries develop multiple different distortion modi although boundary conditions stay the same. Hence, their occurrence frequency seems random.

All necessary material input data for heat treatment simulations are assessed and either taken from literature, measured or modelled according to current state of the art methods. Transformation kinetics, describing phase transformation behaviour during heating and quenching, prove to be a key factor in successfully describing the emergence of thermal distortion. As a widely accepted approach in estimating transformation kinetics based on the material's chemical composition fails to reproduce results of the previously measured CCT diagram, an optimisation procedure is developed. Hardness values and transformation behaviour are optimised consecutively based on controlled quenching experiments. An additional validation of the modified material model, including the modified Jominy experiment, emphasises the significantly improved prediction capabilities for phase structure and hardness values.

FE-simulations of the previously conducted experiments are set up and carried out. All simulations are realised with the commercially available FE-software Forge by Transvalor. The simulations enable the tracing of residual stresses, temperature, microstructure, and hardness during heat treatment. The computational time of heat treatment simulations is drastically reduced by neglecting the blanking step as remeshing and element deletion can be avoided while maintaining the same quality of predictions. Distortion and hardness of specimens are compared with measured data. Although numerical simulation results are in line with the experiment series, not all experimentally observed deformation modi can be identified. A buckling analysis is carried out which successfully anticipates the additional modi that are not covered by the regular simulation.

Kurzfassung

Die meisten feingeschnittenen Teile werden nach der Umformung einer Wärmebehandlung unterzogen, um angestrebte mechanische Eigenschaften zu erfüllen. Veränderungen in Form und Grösse sind meist unvermeidbar und treten vor allem beim Härteprozesses auf. Dieser thermische Verzug ist von Material, Geometrie und der Behandlungsmethode sowie deren Randbedingungen abhängig. Eine Vorhersage des Verzugs ist äusserst komplex, kann jedoch potentiell viel Geld und Zeit bei der Nacharbeit von Produktionswerkzeugen einsparen. Die vorliegende Arbeit behandelt die Wärmebehandlungsmethode Durchhärten, deren Auswirkungen auf den Verzug und numerische Modellierung. Viele Aspekte sind mit Anpassungen auch auf andere Verfahren, wie beispielsweise auf das Einsatzhärten, übertragbar. Ziel ist es die thermische Verzugsvorhersage von feingeschnittenen Teilen so zuverlässig zu gestalten, dass die Nacharbeit an Werkzeugen und Teilen reduziert werden kann.

In einem ersten Schritt werden die mechanischen und thermischen Materialeigenschaften von C60E Stahl aufgenommen. Die Fliesskurve, Anisotropie und ein kontinuierliche Zeit- Temperatur- Umwandlungsschaubild (ZTU) werden bestimmt. Zusätzlich wird mit einem modifizierten Stirnabschreckversuch für Blech die Härtbarkeit des Materials gemessen. Durch Erfassung der Temperaturentwicklung mit einer Wärmebildkamera können diese Messungen zur Validierung von thermischen Materialdaten für FE-Simulation eingesetzt werden.

Folgend werden Experimente durchgeführt, um die Haupteinflussfaktoren auf den thermischen Verzug zu bestimmen. Primär werden der Einfluss von verbleibenden Eigenspannungen nach Umform- und Schneideprozess, Geometrie sowie Chargierung untersucht. Alle Teile werden dabei vor und nach der Wärmbehandlung optisch vermessen und mit der Soll-Geometrie verglichen. Um zwischen stochastischen Schwankungen und deterministischen Zusammenhängen unterscheiden zu können, werden die Resultate

statistisch analysiert. Im Gegensatz zum Biegeprozess, welcher den Verzug beeinflusst, zeigt reines Feinschneiden keine signifikante Änderung des Verzugs. Als Konsequenz kann die Schneidoperation für die Verzugsvorhersage vernachlässigt werden. Die beobachtete Orientierungsabhängigkeit im Abschreckkäfig einer flachen, scheibenähnlicher Versuchsgeometrie konnte mit einem zweiten, ähnlichen Bauteil nicht reproduziert werden. Ein weiteres Experiment zeigt Möglichkeiten zur Verzugsminderung mit gestapelten Teilen beim Abschrecken auf. Zwei der untersuchten Geometrien weisen bei gleichbleibenden Randbedingungen mehrere mögliche Verzugsmoden auf. Welche der Verzugsform angenommen wird scheint dabei zufällig.

Alle notwendigen Materialparameter für die Wärmebehandlungssimulation werden aus der Literatur entnommen, gemessen oder entsprechend dem aktuellen Stand der Forschung modelliert. Die Phasentransformationskinetik beim Erwärmen und Abschrecken spielt bei der Entstehung von thermischem Verzug eine entscheidende Rolle. Ein weitverbreiteter Ansatz zur Abschätzung der Transformationskinetik, basierend auf der chemischen Zusammensetzung des Stahls, erweist sich als unfähig die vorgängig gemessenen Abschreckpfade des ZTU-Schaubildes angemessen zu beschreiben. Daher wird ein Verfahren entwickelt, welches mit Hilfe von kontrollierten Abschreckexperimenten zuerst die Härte und nachfolgend das Transformationsverhalten optimiert. Mit dem Stirnabschreckversuch wird die daraus erfolgte Verbesserung der Voraussagequalität bezüglich Phasenbestandteile und Härte validiert.

Die FE-Simulationen der Abschreckexperimente werden in der Software Forge von Transvalor aufgebaut und durchgeführt. Somit kann die Entwicklung von Eigenspannungen, Temperatur, Mikrostruktur und Härte während der Wärmebehandlung nachvollzogen werden. Durch Vernachlässigung des Schneideprozesses und den damit verbundenen Remeshing- und Elementlöschvorgängen wird die Simulationszeit der Wärmebehandlung bei gleichbleibender Genauigkeit substantiell reduziert. Der Verzug und Härte werden anschliessend mit gemessenen Daten der Versuchsteile verglichen. Obwohl die numerische Simulation die experimentellen Resultate mit den optimierten Materialdaten gut abbildet, können nicht alle real vorkommenden Deformationsmoden abgebildet werden. Eine Knickanlayse wird durchgeführt, welche die weiteren, von der regulären Simulation nicht abgedeckten, Verzugsmoden erfolgreich erfasst.

Contents

Nomenclature

Latin symbols

A_{c1}	austenite start temperature during slow heating
A_{c3}	austenite finish temperature during slow heating
B_s	bainite start temperature
$\mathbf{C}$	heat capacity matrix
C_{CL}	normalised Cockroft and Latham damage parameter
C^*_{CL}	critical normalised Cockroft and Latham damage parameter
c_p	specific heat capacity
d	deviations before heat treatment
$\overline{d}$	average deviation before heat treatment
D	deviations after heat treatment
$\overline{D}$	average deviation after heat treatment
E	Young's modulus
htc	heat transfer coefficient
HV	VICKERS hardness
$\mathbf{K}$	stiffness matrix
$\mathbf{K}_\lambda$	heat conductivity matrix
M_s	martensite start temperature
M_f	martensite finish temperature
q	heat flow
q''	surface heat flow density
q'''	volumetric heat flow density
$\dot{Q}$	heat flows
R	universal gas constant, $R = 8.314472\,\frac{J}{molK}$
t	time
T	temperature
T_L	Leidenfrost temperature
T_∞	environmental temperature
y	phase fraction

Greek symbols

α	thermal expansion coefficient
ε	emissivity
ε^{pl}	plastic strain
ε^{e}	elastic strain
ε^{th}	thermal expansion strain
ε^{tr}	transformation based strain
ε^{tp}	transformation plasticity strain
λ	thermal conductivity
η	transformation factor
ν	Poisson's ratio
σ_y	yield stress
σ_{vm}	stress equivalent after VON MISES
σ_B	STEFAN-BOLTZMANN constant, $\sigma_B = 5.6704E{-}08\ \frac{W}{m^2K^4}$
ρ	density

Operators

$\dot{x}$	differentiate x with respect to time
$div\, x$	divergence of x
$grad\, x$	gradient of x

Indices

$()_x$	value in x direction
$()_y$	value in y direction
$()_z$	value in z direction
$()_a$	austenite fraction
$()_b$	bainite fraction
$()_f$	ferrite fraction
$()_p$	perlite fraction
$()_m$	martensite fraction
$()_{lying}$	parts that are quenched in lying position
$()_{hanging}$	parts that are quenched in hanging position
$()_{Block}$	parts that are quenched in block formation

$()^{fb}$	refers to fine blanked parts
$()^{wj}$	refers to water jet cut parts
$()^{CW}$	refers to chain wheel parts

Abbreviations

bcc	body centred cubic
CCT	continuous cooling transformation diagram
DOE	design of experiments
fcc	face centred cubic
FE	finite element
FEM	finite-element-method
HV	Vickers hardness
JMAK	Kolmogorov-Johnson-Mehl-Avrami (equation)
TRIP	**TR**ansformation **I**nduced **P**lasticity
TTT	time temperature transformation diagram

1 Introduction

The requirements for modern steel increase as the demand for lighter and stronger construction parts rises. In order to improve mechanical properties, heat treatment is pervasively used but the procedure has disadvantages. During treatment a part is exposed to change in dimensions, shape, internal stresses and phase composition especially during the quenching process. In practice it is favoured to enhance hardness but minimise residual stresses as they can shorten service life and cause distortion of the part. Thermal distortion may leads to subsequent operations on tools or hardened workpieces in order to fulfil stringend tolerance requirements. Those reworks often consist of extensive tryout-loops, delay production and generate high costs. Because of the uncertain shape accuracy of hardened parts they are often overdimensioned, which contradicts the idea of lightweight constructions. In some cases different and more expensive hardening methods have to be used to stay in the desired tolerances.

This work has a special focus on heat treatment and distortion of fineblanked parts and associated process-specific particularities. Usually, fineblanking is used when high quantities but also strict requirements, such as tight tolerances and mechanical properties are demanded. Heat treatment is unavoidable for many of those applications. Being able to estimate change in size and shape, as well as forecasting hardness and phase structure requires a deep understanding of material behaviour, heat treatment process and dependencies on preliminary forming steps. Nevertheless, successfully predicting thermal distortion before manufacturing tools can be useful to reduce tryout-loops and thus has great cost-saving potential.

1.1 Fineblanking Process

Fineblanking is a shearing process and a special form of blanking that results in precise, often ready-for-assembly workpieces. Contrary to regular blanking, surfaces in the blanking zone are smooth and there is often no

burr. By using a counter punch to prevent bending, a v-ring close to the cutting contour and a small clearance between punch and die allows fineblanking to achieve desired tolerances. The process details are more deeply discussed in chapter 2.1.
The scope of products ranges from gears, chain wheels, seat adjusters, brake lining plates and other automotive parts. See figure 1.1 for some examples. The technology is also used to manufacture contact levers for the electrical industry and surgical instruments. Because of relatively low production costs for high volumes while still maintaining good quality, the majority of fineblanked parts are used in the automobile industry. A typical car has up to 200 fineblanked parts installed. Many of those applications require heat treatment to reach all desired mechanical properties.

Figure 1.1: Range of different fineblanking parts (source: Feintool AG)

1.2 Heat Treatment of Steel

Heat treatment processes can be divided into three main groups: annealing, hardening and tempering [71]. The main focus of this work is on the hardening process, which has the goal of raising hardness and resistance to wear and tear but is also responsible for the majority of thermal distortions. DIN EN 10052 defines hardening as heating a specimen above austenitising temperature and cooling it under conditions that increase hardness due to more or less complete phase change from the austenitic phase to martensite and, as the case may be, bainite [37].

Hardening can be performed throughout the entire work piece, referred to as through hardening. Other possible treatments are surface or thermochemical hardening. The latter two only affect a certain depth of the material. Unlike surface hardening, the chemical composition of the skin layer is changed during thermochemical treatment. There exist a multitude of other treatment processes, for example induction hardening, nitriding or carbonitriding [71, 25].

1.2.1 Hardening of Steel

The hardening process is shown schematically in figure 1.2. The initial heating is usually slow and heads to the hardening temperature which depends on the respective treatment and the chemical composition of the material, mainly on the carbon content and other alloying additions.

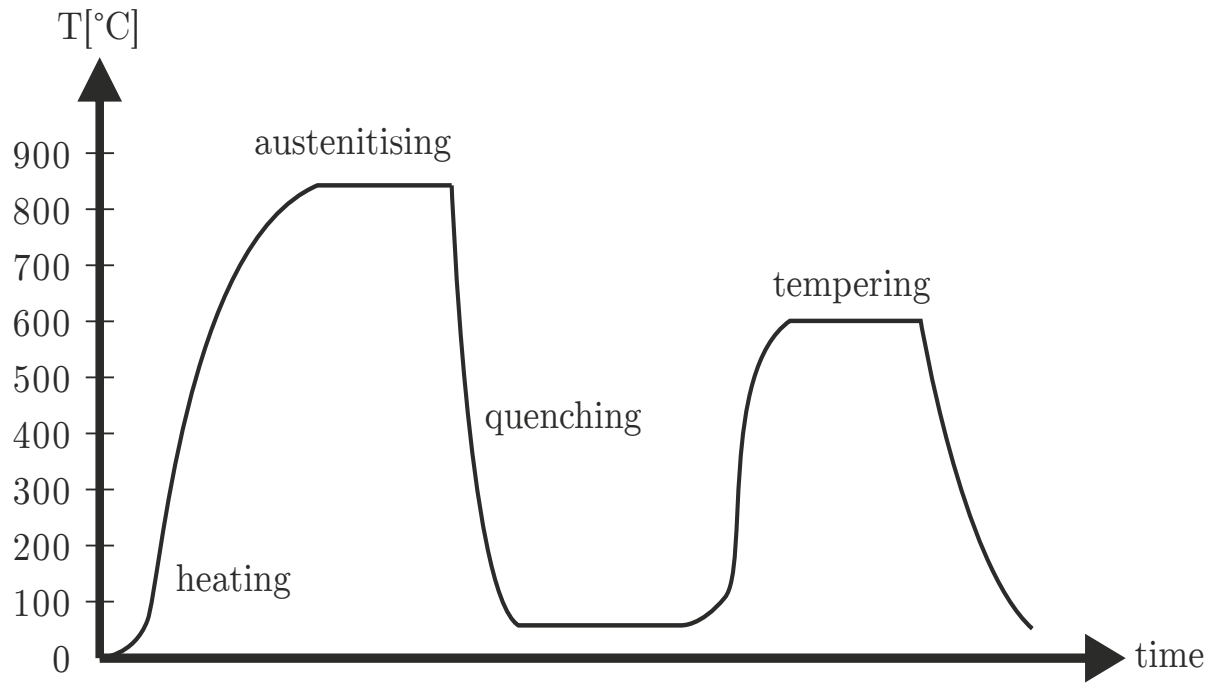

Figure 1.2: Schematic temperature curve during hardening and tempering

After reaching the holding point, temperature is kept constant for a certain time. This so-called holding time depends on the intended treatment and on the dimensions of the part. Typically, the holding time is chosen to be long enough to secure full austenitisation while having no significant changes in grain size.

In some types of treatment, e.g carburisation, this step is used to change the chemical composition of the skin layer. The following cooling step is called quenching. The cooling rate varies with surface-to-volume ratios of the part and is primarily controlled by the heat transfer of the quenching agent. The process details are more deeply discussed in section 2.2.1. Hardness after quenching mainly depends on quenching rate and carbon content and may reach up to 1000 HV. To increase ductility while maintaining resistance to wear, it is common to succeed with tempering. Compared to hardening, tempering is conducted at lower temperatures, with longer holding times and smaller cooling rates, resulting in only minor geometrical changes [71].

1.2.2 Quenching Induced Stresses and Distortion

Hardening does not only influence mechanical properties but causes, generally unwanted, distortion of the part. Thermal stresses emerge during quenching and often result in a change of size, shape or most commonly in a combination of both [44]. There are several reasons for this behaviour during quenching as summarised in figure 1.3.

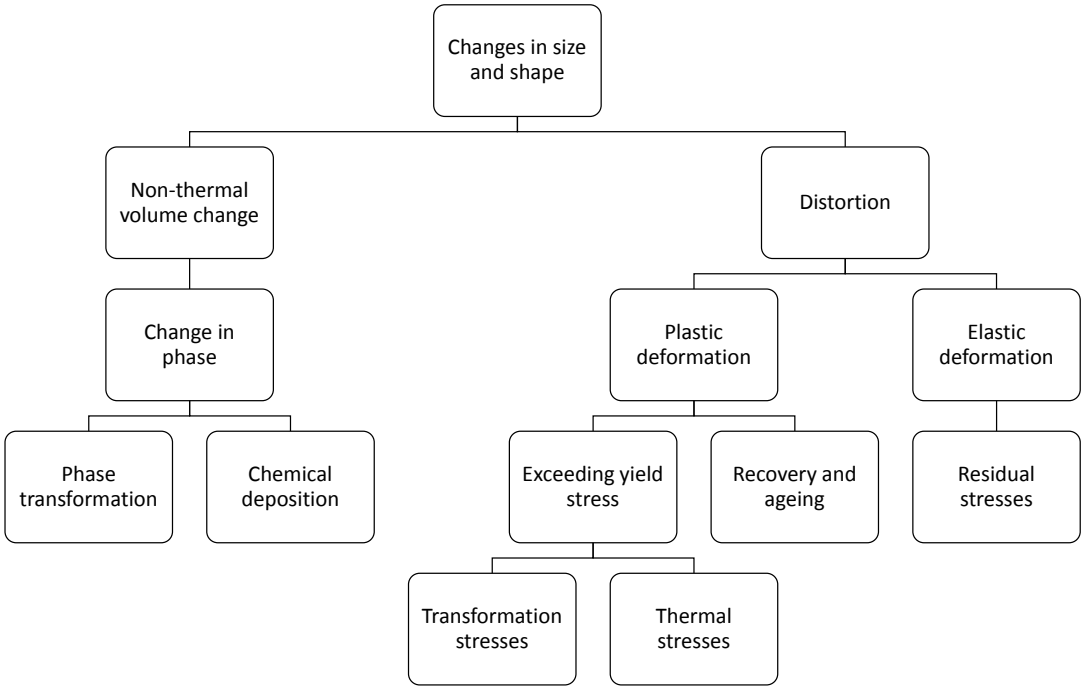

Figure 1.3: Causes of changes in size and shape [52]

A change in phase composition and thus in specific volume can be caused by phase transformations or chemical deposition. The classification of non-thermal volume change refers to the unavoidable mechanism independent of temperature evolution.

Distortion may be divided in plastic and elastic deformations, whereas the latter is exclusively obtained by residual stresses. Some of which occur after every heat treatment and are defined as the remaining stresses in a solid material after all external forces and moments are removed. During quenching, temperature is unevenly distributed over the work piece and as a consequence, the core of the part is subject to smaller cooling rates than the skin layer. The surface contracts faster than the core, which leads to compression in the middle and tensile stresses in the outer layer. If those stresses, combined with phase transformation induced stresses, exceed yield strength, plastic deformation occurs. Recovery and ageing can also lead to irreversible change in plastic deformation [52].

The extent of distortion is process- and part-dependent and increases with greater temperature gradient between core and surface, higher cooling rate, larger specimen size and decreases with smaller heat conductivity and increased structural stability of the part [45, 42, 52]. The influence of geometry and size of a work piece on its thermal distortion will be more deeply discussed in chapter 2.2.3. Further studies have shown that the forming history and potential residual stresses from forming steps may also contribute to the final distortion [73, 90, 1, 32, 60, 20, 46, 75, 29].

Eventhough experimental studies could demonstrate the influence of one or multiple parameters on change in size and shape, results cannot be translated to complex industrial hardening processes in a satisfying manner. When investigating influencing factors on distortion with real experiments, it is important to differentiate between stochastic fluctuations caused by imperfections in material or process and distinct deterministic correlations. Those fluctuations are difficult to anticipate, whereas deterministic relationships are possible to forecast with finite element simulations, providing that boundary conditions and material modelling are capturing all effects involved.

1.3 Simulation of Heat Treatment

Finite element simulation of heat treatment is becoming more important as computational performance and material models advance. Current research focuses on distortion prediction, final material properties as well as optimising treatment procedures, batching and quenching agents.
Accurate simulations require various temperature- and phase-dependent material and process parameters. An extensive study on the simulation of heat treatment of steel indicates the importance of close to reality input data [45]. Some authors already managed to predict process tendencies, perform parameter studies and effect analysis with finite element simulations [52]. Complex geometries still require long and intense computing. State of the art phase transformation algorithms and material models are costly to obtain and often fail to describe reality. Some of the most frequently applied models are discussed in chapter 5.2.

1.3.1 Material Modelling

A general consensus has been reached that, in addition to the heat transfer, accurate material modelling is key to successfully predict distortion effects due to heat treatment [45]. Some material characteristics can be taken from literature, others have to be measured and/or modelled [45, 52]. Close to reality transformation kinetics, which describe phase transformation behaviour, are essential. Because of the importance but at the same time poor applicability of current models, a new approach, based on controlled quenching experiments, is presented in chapter 5. Furthermore, a validation experiment for sheet metal was developed in order to efficiently measure multiple quenching rates at once (see chapter 3.3).

1.4 Motivation and Goal of this Work

Being able to forecast distortion, residual stresses, phase composition and mechanical properties, such as hardness after heat treatment, can reduce costs for manufacturing substantially. Figure 1.4 shows schematically how finite element simulations could potentially be used to compensate for thermal distortion due heat treatment of fineblanked parts.
The first simulation step aims to predict the shape after fineblanking that

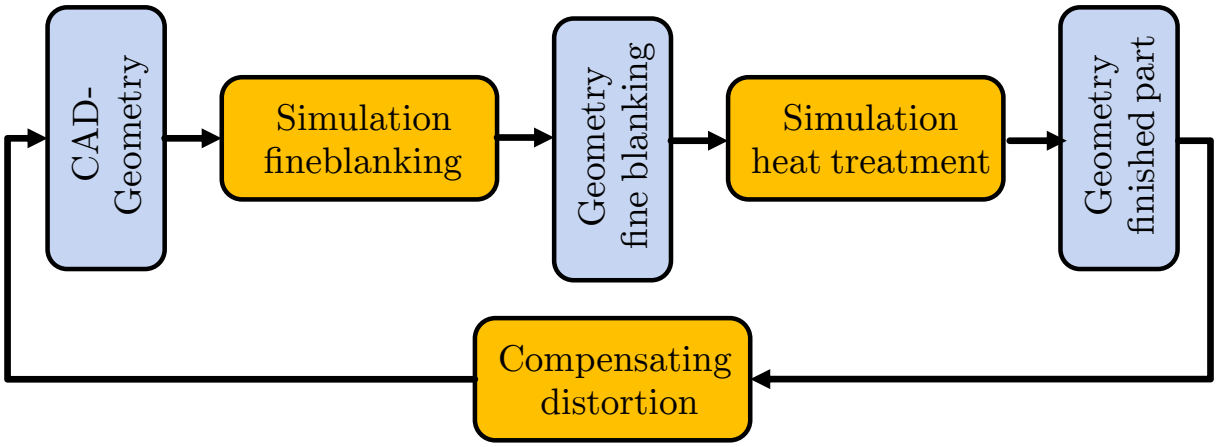

Figure 1.4: Compensating for thermal distortion

has already deviations from CAD-geometry (e.g. die roll). During the subsequent heat treatment simulation changes in shape and size are obtained. The information can thereafter be used to compensate the original CAD-geometry or the geometry of the blanking tools. Successfully predicting thermal distortion may also be helpful for choosing the cheapest heat treatment solution.
In order to predict distortion reliably, especially for fineblanked parts, experimental and virtual investigation are performed in the upcoming chapters. The key issues addressed in this thesis are:

- Investigating the consequences of fineblank and forming operations on thermal distortion. In case of possible simplifications or complete omission of the forming step, a significant amount of computational time can be spared when simulating heat treatment of fineblanked parts.
- Dependencies between process properties and their influence on distortion have to be separated from uncontrollable process variations. Hence, a differentiation between stochastic fluctuations and deterministic correlations during experiments has to be made.
- Identification of material and process parameters that are relevant for finite element simulations of heat treatment processes.
- Determination and validation of relevant unknown material and process characteristics in order to successfully simulate heat treatment behaviour.

2 Basics and State of the Art

The following chapter establishes basic concepts and state of the art regarding main topics addressed in this thesis. Firstly, the fineblanking technology is presented followed by fundamental concepts of the hardening process and its influence on the work piece. Further, finite element simulation basics of coupled forming and heat treatment processes are discussed.

2.1 Fineblanking Process

Fine blanking is a severing process and classified as single stroke shear cutting with a V-ring plate and counter punch in order to manufacture parts with smooth and crack free surfaces [40]. A counter punch prevents bending of the part during the cutting process. Figure 2.1 shows a schematic illustration of the process:

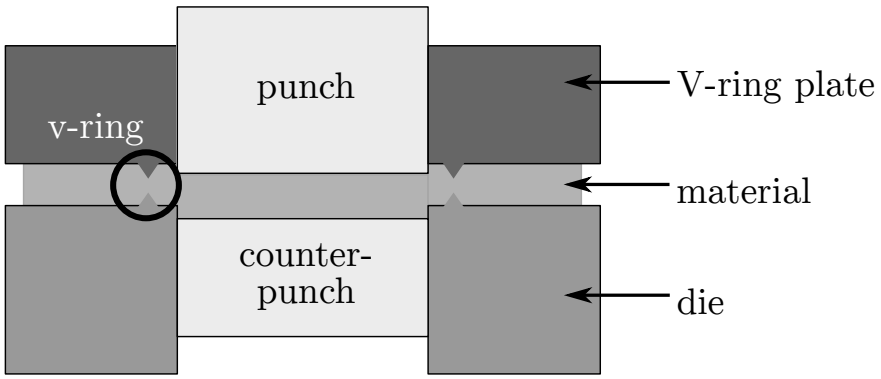

Figure 2.1: Schematic illustration of the fineblanking process

Other distinctive features are small clearance and in many cases an impingment ring (or V-ring) to enhance hydrostatic pressure in the cutting zone. Fineblanked parts typically have die roll but smooth surfaces. A more detailed description of the process and its resulting parts can be found in the works of Wesner and Manopulo [121, 89].

2.2 Heat Treatment of Steel

Relations and interactions of the three main physical fields during heat treatment are visualised in figure 2.2. All fields, heat transfer (thermal field), phase transformations (metallurgical field) and stress-strain evolution (mechanical field), are coupled with each other.

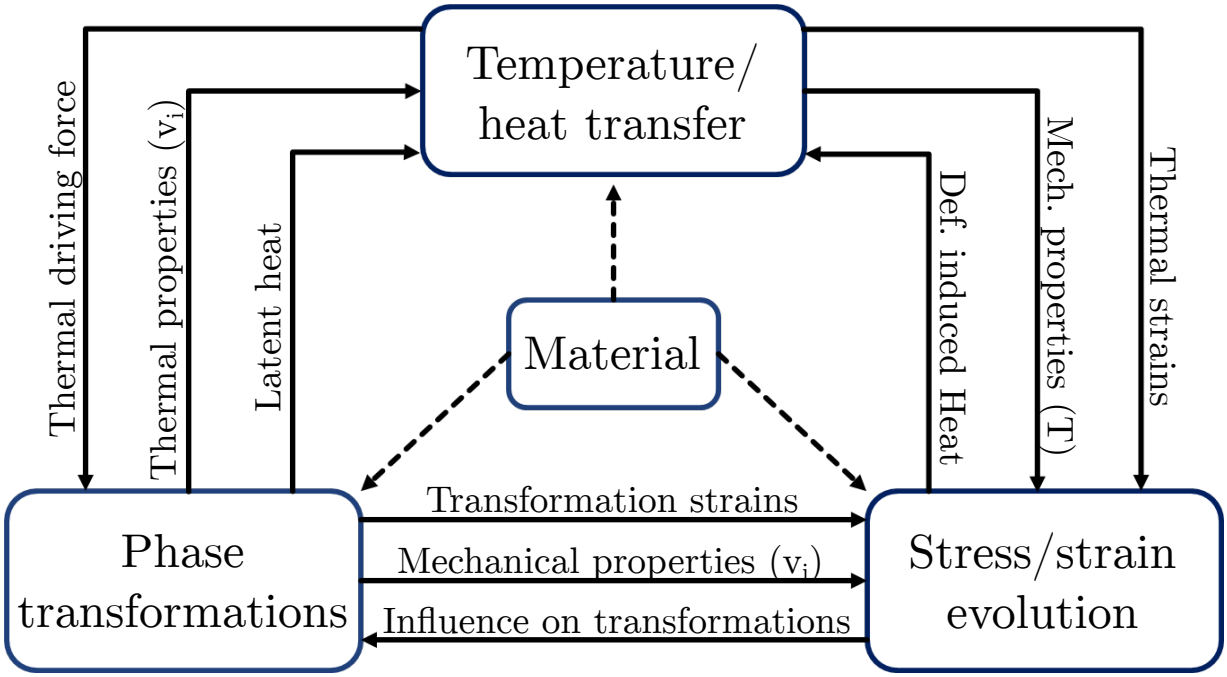

Figure 2.2: Thermo-mechanical and metallurgical interdependency during heat treatment [107]

The temperature profile during heat treatment is the main driving force of phase transformations and strongly regulated by the heat transfer, which itself is material and process dependent (see chapter 2.2.1). By changing the phase composition due to transformations, thermal properties of the material are changed as well. Additionally, latent heat is released or absorbed coincidently. Thermal strains are induced by position and surface temperature dependent heat transfer, which leads to an inhomogeneous temperature distribution. This phenomena and its effect on temperature dependent mechanical properties and ultimately on distortion is further explained in chapter 2.2.3. Thermal stress may exceed yield stress and the resulting plastic deformation leads to additional heating of the material. Phase transformation caused volume change may also elicit in transfor-

mation strains. Mechanical properties depend on the phase fractions and change with phase transformation as well. Eventually, the current stress and strain state may affect transformation speed as reviewed in section 2.2.3. Material properties influence all physical fields and are therefore of major importance while simulating heat treatment. The modelling of material and transformation kinetics for finite element simulations can be found in chapter 5.

2.2.1 Thermal Boundary Conditions

Temperature of a free body decreases due to natural or forced convection, heat transmission within the material and heat radiation. In the following, temperature change of any physical system that results in internal heat transfer and externally driven dissipation processes is discussed with a focus on phenomena during quenching.

Heat Transfer During Quenching

Quenching is defined as cooling at a higher rate than with stationary air [37] and is most commonly performed with pressurised gases or liquids, for example water or oil. Heat transfer of liquid quenching agents changes with falling temperatures and can be divided in three major stages as shown in figure 2.3.
Soon after an austenitised specimen is immersed into the liquid, a stable vapour film is formed. The film works as an isolator and limits heat transfer to the quenching medium, also known as Leidenfrost effect [78]. After passing the Leidenfrost temperature T_L, the vapour film destabilises and the specimen has direct contact with the liquid. During this transition nucleate boiling increases heat transfer up to its maximum. The subsequent stage is dominated by natural convection with significantly smaller heat transfer. Evolution of temperature during quenching and corresponding heat flux density are illustrated schematically in figure 2.4.
The temperature decreases slowly as long as the vapour film is present. But as soon as temperature falls below T_L, transition followed by nucleate boiling is induced. This period is accompanied with high heat flow and therefore strong heat transfer. During this boiling phase, the temperature of the part drops rapidly. The following natural convection phase decreases temperature only slowly.

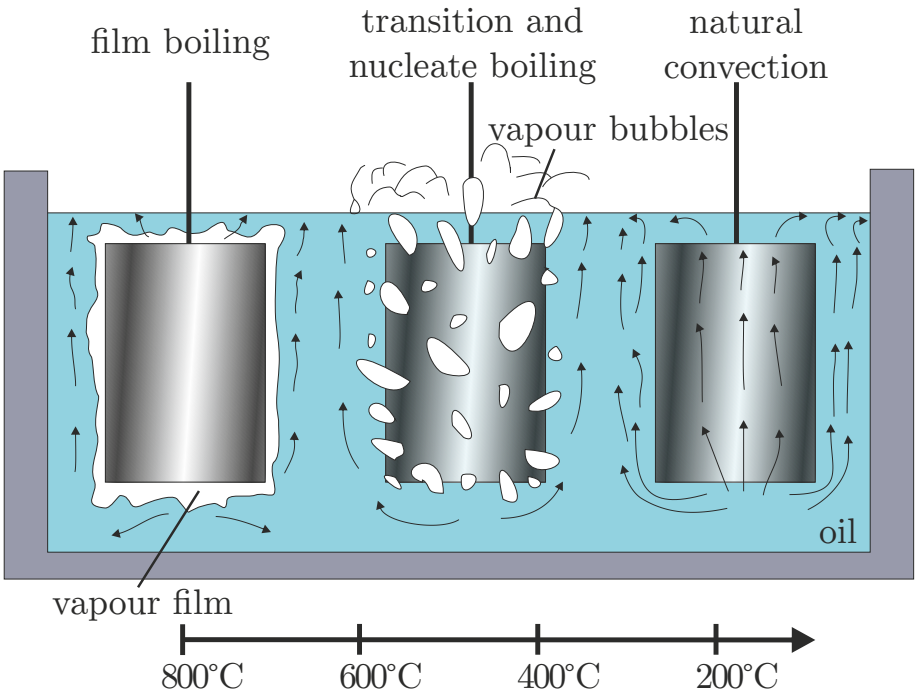

Figure 2.3: Three stages of quenching in liquids [71]

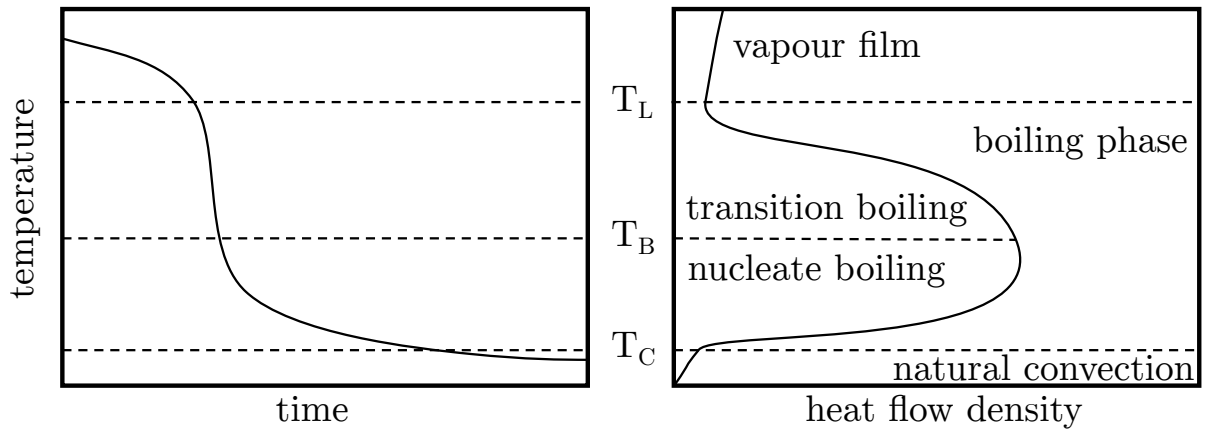

Figure 2.4: Cooling curve and heat flow density during quenching [87]

There are several testing methods to characterise the cooling effect of a quenching agent [14]. However, none is easy to measure accurately as they depend on a multitude of parameters; there are material specific factors, such as thermal conductivity, surface conditions, hardenability and process specific factors such as initial temperature of the specimen and the quenching agent. The heat transfer is also dependent on movement of the liquid or the specimen as well as the geometry and dimensions of the part [71].

Heat Convection

Heat convection q_{conv} is the main driving force of heat loss during quenching and can generally be written as:

$$q_{conv} = hA(T - T_\infty) \tag{2.1}$$

T is the surface-, T_∞ the environmental temperature and A is the body surface area. The heat coefficient h can be surface temperature- and or position-dependent to account for the previously explained effects. Fluid flow direction and speed are also influencing h.

Emissivity

Thermal energy loss through radiation q_{rad} of a grey body (emissivity lower than 1) depends on material properties and specimen geometry and can be expressed as:

$$q_{rad} = \sigma_B \cdot A \cdot \varepsilon \cdot (T^4 - {T_\infty}^4) \tag{2.2}$$

where σ_B is the Stephan-Boltzmann constant with $\sigma_B = 5.670373\frac{W}{m^2K^4}$, ε the emissivity, T and T_∞ the body and surrounding temperatures [110, 23].

Thermal Conduction

The uneven temperature distribution of a body leads to transfer of internal heat. At any given time this thermal dynamic can be expressed with the Fourier heat equation:

$$\rho c_p \frac{\partial T}{\partial t} = \nabla(\lambda \nabla T) + q_{int} \tag{2.3}$$

Where T describes temperature and t the time. The thermal conductivity λ, density ρ and specific heat capacity c_p are material- and temperature-dependent physical parameters. q_{int} represents internal dissipation [12].

2.2.2 Phase Structure and Crystallographic Basics

In order to understand various effects during different stages of heat treatment it is necessary to have a basic crystallographic understanding. The most important concepts and processes that occur during quenching are

summarised in the following. Because of the complexity and broadness of this topic the focus is not on completeness but rather on a general overview. The ASM handbook for steel heat treatment [113] and two other established works by Thelning [112] and Laepple [71] were considered while writing this section.

Iron-Carbon and CCT Diagrams

The iron-carbon diagram is the fundamental basis of any heat treatment process but only describes equilibrium state between carbon and iron. Time, or rather quenching speed, is the most important factor in achieving the desired mechanical properties for most heat treatment processes. Hardening of steel always requires a carbon content of at least 0.2%, steels with smaller carbon concentration require almost unachievable quenching rates and are exposed to crack formation and strong thermal distortion. Furthermore is the achievable hardness unsatisfactory [71]. The phase transformation for different cooling rates can best be described by continuous cooling transformation (CCT) diagrams. The relationship between the iron carbon and the CCT diagram for C60 steel is visualised in figure 2.5.

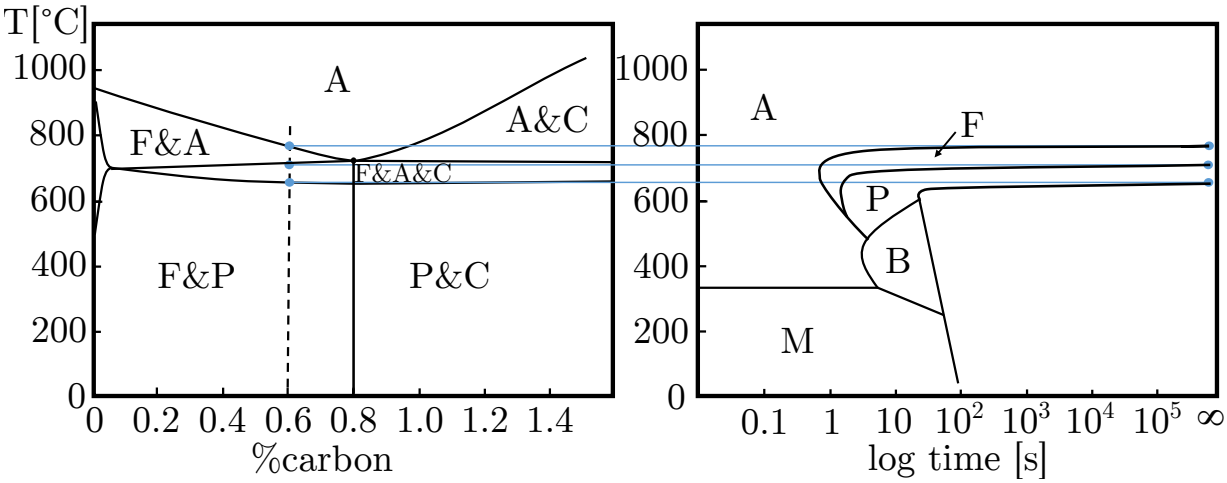

Figure 2.5: Relationship between the iron carbon equilibrium (left) and CCT diagrams (right) illustrated for C60 steel

The iron carbon diagram is only valid for slow cooling so that equilibrium condition between the two components is present (illustrated on the far right side of the corresponding CCT diagram) [71]. The following abbreviations were used; A for austenite, F for ferrite, C for cementite, P for

perlite, B for bainite and M for martensite. The CCT diagram provides information of phase transformations dependent on different quenching paths respectively cooling rates.

Cooling from Austenite

Prior to cooling it is necessary to fully austenitise steel so that carbon atoms are at least partially dissolved in the crystal lattice. Austenitisation is defined as a single step during heat treatment in which a work piece is brought to a temperature such that the structure becomes austenitic. If the transformation of ferrite, or perlite to austenite is incomplete, the austenitisation is termed partial [37]. Due to the polymorphy of steel, the body centred cubic (bcc) structure transforms to face centred cubic (fcc) when cooling from the austenite region [71]. The cooling rate is decisive if carbon diffusion is possible, limited or prevented. Diffusion decreases with increasing cooling rate as transformation of bbc to fcc takes place at lower temperatures. This effect leads to different transformation mechanisms and other phase structure. In the following, a simplified explanation of transformation mechanics is presented. A detailed description of the process can be found in literature [112, 71, 57].

Perlite Transformation

During subcritical cooling of hypo-eutectoid steel ($C < 0.8\%$), ferrite begins to form from austenite and is shortly after followed by the formation of perlite. Perlite transformation is initiated at the boundaries or other disarrays in the austenite grain. The lower the transformation temperature of perlite, the closer the interlamellar spacings. During the formation of perlite from austenite carbon and iron atom diffusion takes place. The resulting structure consists of two crystal components; high carbon cementite and low carbon ferrite. Typical hardness values of perlite are between 200 HV - 350 HV.

Bainite Transformation

Bainite transformation starts at already lowered temperatures of circa 550 °C, hence carbon atom diffusion is decreased and diffusion of the larger iron atoms is almost entirely blocked. Its formation can be understood as a combination of perlite and martensite transformation as both limited diffusion

of carbon and diffusionless lattice shearing of austenitic phase structure, are present. It is differentiated between upper and lower bainite, depending on the formation temperature and thus altered transformation mechanisms [96, 99]. As a result, bainite hardness may lie between 350 HV - 800 HV. In general, upper bainite is brittle and lower bainite has high toughness and rigidity [71]. It can be difficult to optically differentiate bainite from other phase structures as it changes its appearance depending on the formation temperature [112]. .

Martensite Transformation

When the cooling is fast enough, austenite transforms to martensite. The minimum quenching rate in order to get 100% martensitic composition is called the upper critical cooling rate. After reaching the M_S line in the CCT diagram, diffusionless lattice shearing from fcc austenite to bcc crystal structure emerges. The carbon atoms have not enough time to diffuse due to the low transformation temperature. The obtained martensitic structure is a supersaturated solution of carbon in $\alpha - iron$. This transformation is exemplary illustrated in figure 2.6.

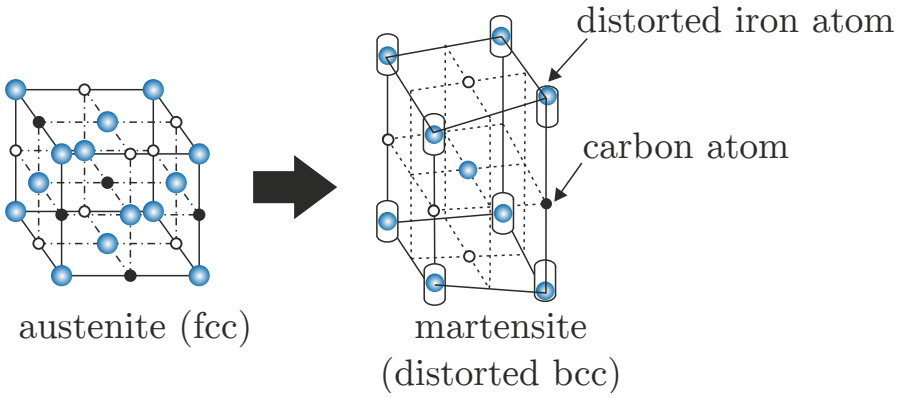

Figure 2.6: Martensite transformation from austenite [71]

The carbon atoms on the edges result in distortion of the crystal lattice. The bcc structure is actually too densely packed for the additional carbon atoms resulting in tensions and tetragonal expansion. The volume increases with an increasing number of carbon atoms [112]. Because of the high tension inside the lattice, dislocation movements are restrained. This leads to a high toughness and lowered plastic formability with hardness values

up to 1100 HV [71]. The formation of perlite, ferrite and bainite happens over time whereas martensite arises suddenly. Hence, every temperature level below M_S corresponds to a certain amount of transformed martensite.

Volume Expansion During Martensitic Transformation

Moyer and Ansell [91] investigated the volume expansion during martensite transformation and showed that the change can be measured reliably using a dilatometer. The level of expansion starting at M_S temperature depends on two separate effects. High carbon content lowers M_S and results in a larger volume expansion. The lattice parameters of martensite and austenite also depend on alloying additions (and carbon content), thus the change in volume due to phase transformation does not only rely on transformation temperature. Therefore two steels with the same M_S but different compositions may have differing volume expansion. It was observed that the volume expansion varies linearly between 2% and 3.1% at carbon content of 0.19 weight-% and 1.01%, respectively [91].

Influence of Alloying Additions

Usually, not pure but alloyed steels are used for industrial applications. Alloying elements such as chrome, molybdenum, nickel and manganese are added in order to reduce the critical cooling rate and therefore making subcritical quenching easier to achieve. This effect can be explained by a reduction of diffusivity of steel by the above listed alloying elements [71]. A more in depth analysis of the effects of alloying addition on the hardenability of steel can be found in further literature [112, 113, 103].

2.2.3 Residual Stresses and Distortion

There are many causes for distortion as already mentioned in chapter 1.2.2, some of them can be avoided under perfect conditions during heat treatment, others are unpreventable. In the following sections the classification of distortion and the main influencing factors are discussed.

Emergence of Thermal Distortion

The classification by Wyss [123] distinguishes between three different base tendencies. Tendency I describes change in size that occurs even without

any plastic deformation but rather because the specific volume correlates with phase structure. For example a transformation from a hardened pure martensitic part to a ferrite and carbide micro structure through a very slow normalizing process leads to an unpreventable decrease in volume. The extent of volume change is mainly dependent on carbon content. Figure 2.7 shows the relationship between specific volume of the compound structure and carbon content [79].

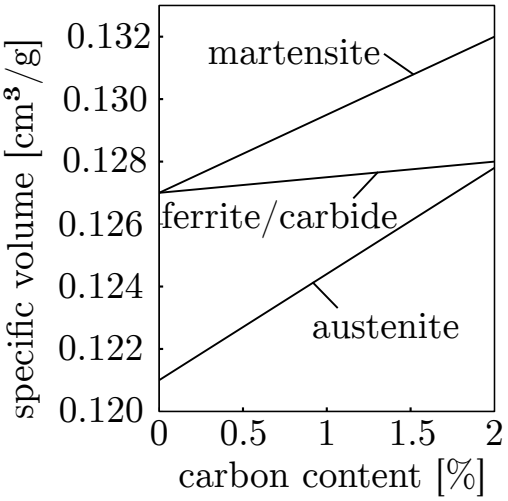

Figure 2.7: Carbon content to specific volume relationship at room temperature after Lement [79]

During quenching, even without phase transformations, thermal stresses develop due to the temperature dependency of the specific volume and the temperature gradient between core and skin of the part as described by [52] and [18]. In the beginning of quenching, the surface temperature decreases and shrinks faster than the core. This process is diagrammatically illustrated in figure 2.8.
Thus, tensile stresses close to the surface and compressive stresses in the core are in equilibrium. With increasing temperature difference, surface stresses can excel the current yield stress (curve b) resulting in plastic deformation (shaded area). After passing the point of highest temperature difference (W), the core shrinks faster than the surface. From this point on the stresses on the surface disintegrate elastically (curve c) until they reach a point, where the stresses reverse (U). After the temperature of core and surface equalise, the surface experiences compression and the core tensile stresses. The stress evolution of the core is represented by curve d. The

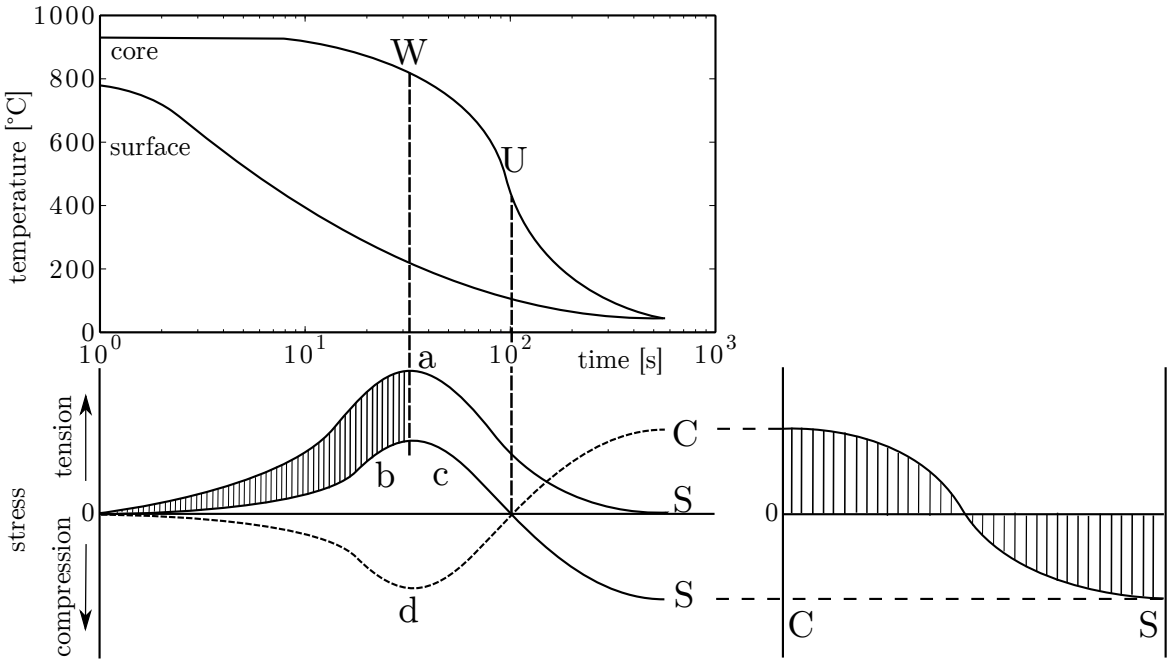

Figure 2.8: Evolution of residual stresses during quenching and remaining stress distribution after Rose [102]

right side of figure 2.8 shows the remaining stresses from surface to core after reaching temperature equilibrium. The resulting change in size and geometry from thermal stresses without phase transformations is classified as tendency II.

Tendency III combines the structural changes and thermal stresses from tendency I and II. Distortion during hardening is caused by overlapping structural changes and thermal stresses. Changes in size and geometry characterised as tendency III have complex interactions discussed by many authors [123, 18, 109, 112, 52, 80, 85]. Schroeder et al. visualised the temperature and stress evolution during distortion as illustrated in figure 2.9 [105].

Three cases; a) fast, b) medium and c) slow cooling are demonstrated. Figure 2.9 shows the impact of the effect of faster cooling on the surface compared to the core (as discussed for tendency II), but also regarding phase transformations that differ for core and surface regions of the part. The upper graphs show the temperature path from fully austenitised structure at T_A to room temperature T_R in a common CCT diagram with different

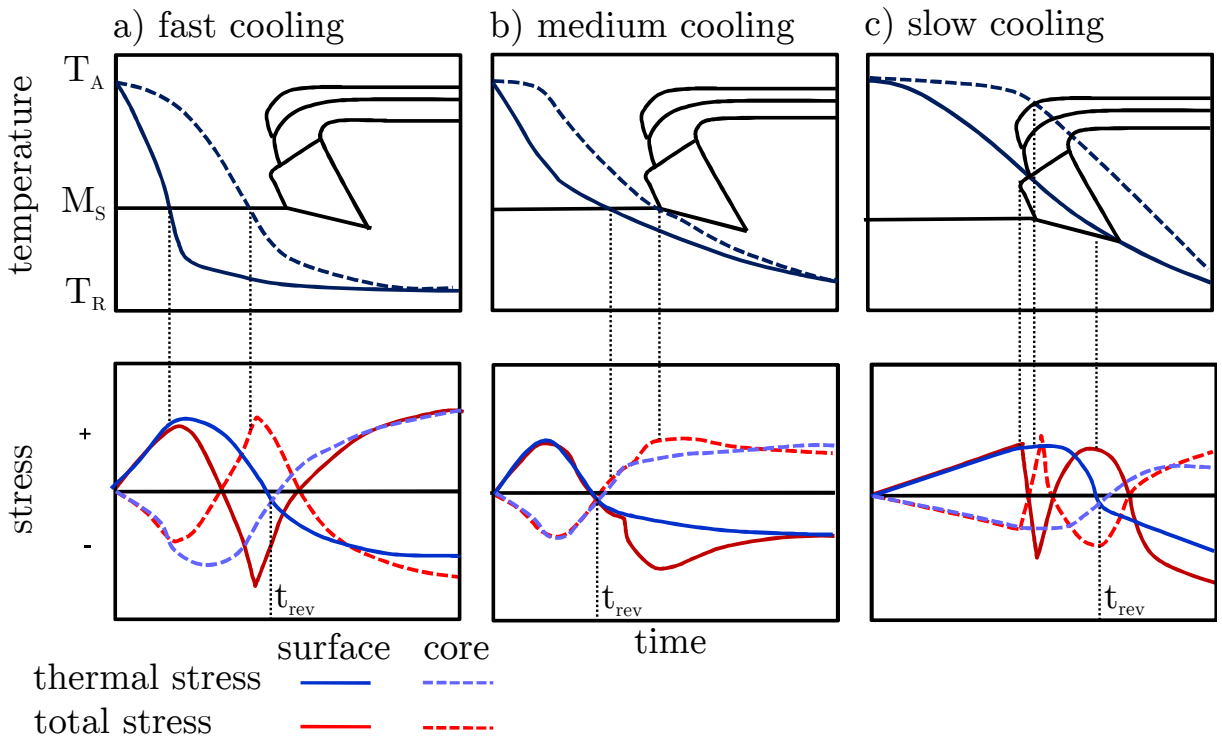

Figure 2.9: Tendency III visualised by Schroeder [105]

phase regions and the martensite start temperature M_S. The dotted line represents the temperature and stress development of the core and the full line shows the same for the surface.

In case a) core and surface transform fully to martensitic structure, but as the core cools down slower its phase transformation occurs later in time. The reversion of stress (t_{rev}) happens earlier compared to pure thermal stress because of additional compression stress caused by an increase in volume due to the start of martensitic transformation in the surface regions. Before the surface temperature reaches M_S the diagram is congruent with figure 2.8 (see blue lines in figure 2.9). In the illustrations of Schroeder it is assumed that the tension stress leads to a yielding in the core because of its high temperatures at that point. The subsequent martensitic transformation in the core leads to an inversion of the stress state. After complete cooling, tension stresses in the surface region and compression stresses in the core remain. This case example shows that the transformation mechanisms have a significant effect on residual stresses after quenching.

Case b) demonstrates the effect on the stress state when the start of transformations is after the reversion of thermal stresses. The volume change of

the surface due to phase transformation leads to a locally intensified surface compression stress and tension stress in the core. Here it is assumed that no transformation induced plastic deformations occur. The stress history is changed compared to pure thermal effects, but the residual stresses after quenching stay quantitatively the same as non transformational cooling.
In case c) phase transformation in the core finishes earlier than on the surface. This leads to three stress inversions during quenching, that finally result in an equilibrium stress state similar to case b) [52, 105].
These three cases show the complex interactions during quenching and their effect on residual stresses. Generally it can be stated that distortion increases with increasing temperature gradient between core and surface during cooling, faster quenching, lower temperature of the quenching agent, larger part dimensions, poor thermal conductivity and lower material strength [45, 52, 42].

Influence of Geometry and Size

One of the most obvious influencing factors on distortion is the geometry and size of the part. The two main aspects are the structural stability of a part, which can promote or inhibit distortion. Thinner parts tend to distort stronger than their thicker counterparts [93]. On the other hand nonuniform heating and quenching caused by varying surface-to-volume ratios within a part provoke distortion as explained in the previous section. During the design stage of a component it is advisable to seek uniform section sizes, but this is often not possible. Gear teeth and other features have unavoidable higher surface-to-volume ratios, which causes them to heat and cool faster than the rest of the part [113].

Influence of Quenching Direction

When submerging a part in the quenching agent, an optimal orientation in the charging rack is essential. Flow effects and build-up of a vapour film, as described in section 2.2.1, can increase distortion drastically. This is why quenching baths usually contain a pump or propeller to amplify the circulation of the fluid to uniform the baths temperature and to break the vapour film on the part [16]. Also, the degree of agitation significantly influences the agents cooling rate. Another important factor is the flow direction. Von Bergen [16] experimented with oil quenching of cylindrical

bearing outer rings and observed that a predominant upward flow trough the charge made the bore collapse near the top of the ring (as seen in figure 2.10) and reversing the flow resulted in the opposite case. A strong relationship of flow direction and distortion can therefore be assumed.

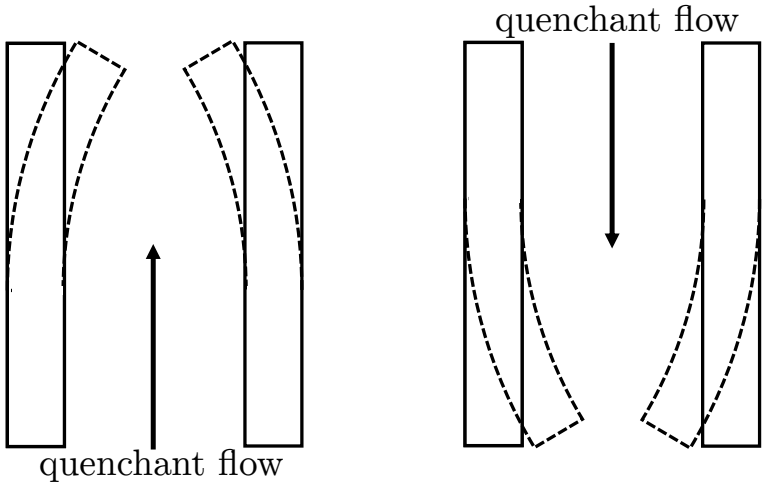

Figure 2.10: Effect of quenching agent flow direction on distortion of bearing outer rings [16]

By reducing the quenching flow to the necessary minimum heat transfer and by mechanically moving the bearing rings up and down, the distortion was brought experimentally to an acceptable level. In general, non-uniform temperature distribution due to quenching flow, vapour film or boiling effects results in more pronounced distortion [113].

Stress Effect on Transformation Kinetics

The stress state can not only lead to distortion during quenching by exceeding the yield stress but has also an effect on the phase transformation kinetics. When phase transformations occur under stress, deviations in deformations opposed to stress free quenching can be observed. Leblond [73] showed experimentally that specimens subject to stress, way below yield stress, show significantly higher deformations than without external stresses. Many studies on the effect of stress state on transformation kinetics were carried out [90, 1, 32, 60]. In summary the mechanisms effecting kinetics can be separated into ones due to hydrostatic pressure and ones due to a stress deviator. Hydrostatic pressure tends to decrease transformation

temperatures and thereby retard transformations, whereas deviatoric stress tends to manifest itself oppositional [107].

Plasticity Effecting Transformation Kinetics

Plasticity prior to heat treatment has, similar to stress, a measurable effect on transformation kinetics as observed in many studies [20, 46, 75, 29]. The retardation of displacive transformations can be explained by the mechanical stabilisation concept. However, there are other more complex effects of plasticity on diffusion controlled transformations dependent on the alloy system [107]. As their influence is rather small and afflicted with many uncertainties, the effect of prior plasticity is usually neglected when performing numerical simulations. An in-depth experimental analysis of the subject was done by Besserdich [19] but will not be discussed in further detail.

2.3 Process Simulation

Accurate predictions of distortion and final phase composition can be used to drastically reduce production costs of industrial parts as mentioned in the introduction. The finite element method is a powerful tool to not only validate experiments and perform parameter studies but also retrace time- and temperature-dependent phase, stress and strain paths. Another advantage is the possibility to separate and identify key influencing factors without the cost of extensive experimental studies.
The process investigated in the scope of this work is divided into fine blanking with or without additional forming operations (e.g. creating an offset) and heat treatment. The second part of the process is consisting, in the case of through hardening, of austenitising, quenching and annealing (whereas the last process step does not result in a change of size or shape and is thereby neglected). The blanking step is mainly a mechanical problem, although an increase in temperature due to the forming process does have an effect on plasticity of the material.
Ideally, the simulation of heat treatment has to account for all effects illustrated in figure 2.2. Only by identifying and accurately modelling the influencing factors of this complex thermo-mechanical interactive system, final distortion and mechanical characteristics such as phase structure and

hardness can be predicted. During the process of forming, a different material model compared to the subsequent heat treatment simulation is used. Therefore, the simulation of the two processes are conducted separately and their coupling is implemented by a transfer of geometry, stresses and strains. The procedure is more deeply discussed in the corresponding chapters.

2.3.1 Finite Element Analysis

The fundamentals of mechanical and thermo-mechanical finite element simulations are discussed in the subsequent sections. Thereafter, the coupling of the mechanical and thermal problem during heat treatment simulations is presented in section 2.3.4. The material modelling (chapter 5) and implementation of process relevant effects for quenching simulations (chapter 6) are main aspects of this work and therefore discussed in individual chapters.

2.3.2 The Mechanical Problem

Relevant principles of continuum mechanics, based on standard works of Bathe [12], Altenbach [4] and Holzapfel [55], are introduced in this chapter. Continuum mechanics is the branch of mechanics that describes the kinematics of deformable bodies that are exposed to external forces. The bodies are modelled as a continuum and microscopic details are neglected. Deformations and strains are connected with constitutive equations (see chapter 3 and 5).

Kinematic

Kinematic describes the displacement of a body from an initial configuration Ω_0 to a deformed configuration Ω_t. The displacement consists of a rigid body movement (translation and rotation) and a deformation (change in shape and size). Kinematic can be described by two different basic approaches. The Eulerian description is mainly used in fluid dynamic problems as the observation point $\mathbf{P}$ is stationary. This allows to trace kinematic properties over time that are located at point $\mathbf{P}$. The Lagrangian description is used to trace position and properties of material points in respect to their reference configuration Ω_0 at $t = 0$. In the case of finite element

discretisation, Lagrangian description allows to account for the history-dependent properties of materialistic points such as strain hardening. This characteristic is essential for describing phase transformation effects during heating and quenching. The body movement can be described with the function $\mathbf{x} = \boldsymbol{\chi}(\mathbf{X}, t)$ by mapping the initial configuration Ω_0 with the current one as seen in figure 2.11.

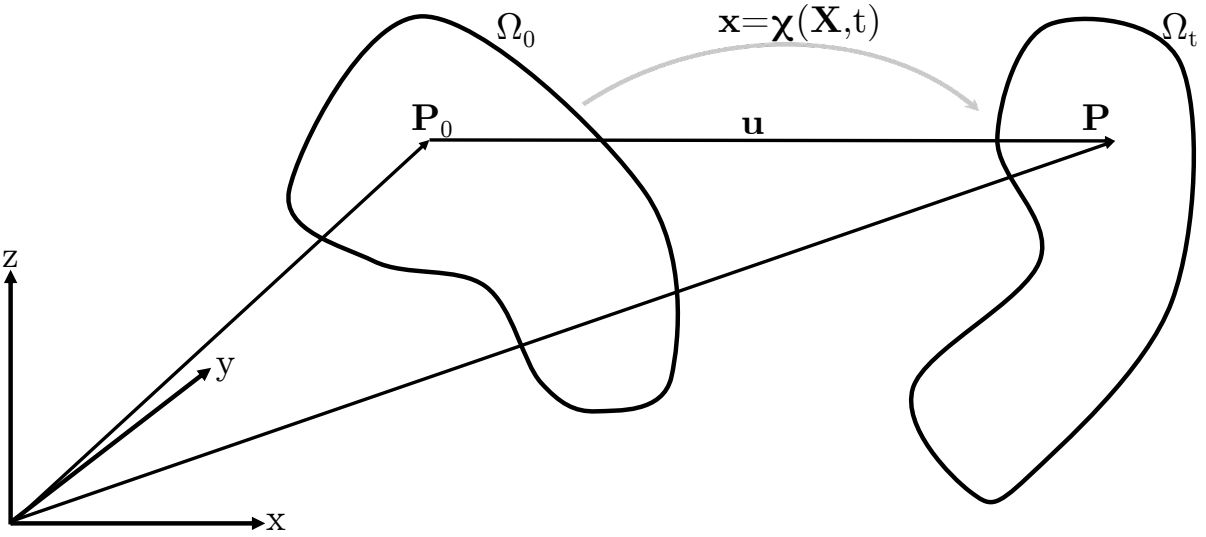

Figure 2.11: System configuration

$\boldsymbol{\chi}$ describes the relationship between the current position $\mathbf{x}$ and the initial position $\mathbf{X}$ of a particle. The displacement $\mathbf{u}$ of a point $\mathbf{P}$ can be expressed as the difference of the current and reference configurations:

$$\mathbf{u}(\mathbf{X}, t) = \boldsymbol{\chi}(\mathbf{X}, t) - \boldsymbol{\chi}(\mathbf{X}, 0) = \mathbf{x} - \mathbf{X} \tag{2.4}$$

The velocity $\mathbf{v}$ is given by the partial derivative of the current position $\mathbf{x}$ with respect to time as the reference position $\mathbf{X}$ stays constant.

$$\mathbf{v}(\mathbf{X}, t) = \dot{\mathbf{x}} = \frac{\partial \boldsymbol{\chi}(\mathbf{X}, t)}{\partial t} \tag{2.5}$$

The acceleration can therefore be written as:

$$\mathbf{a}(\mathbf{X}, t) = \dot{\mathbf{v}} = \ddot{\mathbf{x}} = \frac{\partial^2 \boldsymbol{\chi}(\mathbf{X}, t)}{\partial t^2} \tag{2.6}$$

Deformation, Strain and Stress Gradient

The deformation gradient $\mathbf{F}$ is used to describe stretch and change in angle of a body due to deformation from $t = 0$ to $t = 1$. It can be defined as

$$\mathbf{F} = \frac{\partial \mathbf{x}}{\partial \mathbf{X}} \tag{2.7}$$

and gives the relationship between the infinitesimal $\partial\mathbf{x}$ at $t = 1$ and $\partial\mathbf{X}$ at $t = 0$. The deformation gradient $\mathbf{F}$ can be split in a stretch matrix $\mathbf{U}$ and pure rotation matrix $\mathbf{R}$:

$$\mathbf{F} = \mathbf{RU} \tag{2.8}$$

Deformations can thus be described as an initial stretch and an additional rotation. In order to obtain a suitable strain measure, the right Cauchy-Green deformation gradient $\mathbf{C}$ is introduced:

$$\mathbf{C} = \mathbf{F}^T\mathbf{F} = \mathbf{U}^2 \tag{2.9}$$

There exist several different measures for strain, most important is a neutrality to rigid body motions. Pure motions without any deformation may not result in strains. A measure that matches this condition is the Green-Lagrange strain tensor $\mathbf{E}$.

$$\mathbf{E} = \frac{1}{2}(\mathbf{C} - \mathbf{I}) \tag{2.10}$$

True stress is defined as Cauchy-stress $\boldsymbol{\sigma}$ and can be written as:

$$\boldsymbol{\sigma}(\mathbf{x}, t)\mathbf{n} = \mathbf{t}(\mathbf{x}, t, \mathbf{n}) \tag{2.11}$$

With the stress vector $\mathbf{t}$ as a function of the plane normal $\mathbf{n}$.

Conservation Laws

Conservation laws are the basis to describe thermo-mechanical systems. All laws and their derivations can be found in [12] or [13]. The conservation of mass or continuity equation implies that the mass m of a domain Γ is constant as no material flows through its boundaries and no conversion from energy to mass takes place:

$$\frac{d\rho}{dt} + \rho div(\mathbf{v}) = 0 \tag{2.12}$$

When material is incompressible, as assumed for steel in this context, the material time derivative of the density is zero $div(\mathbf{v}) = 0$.
The conservation of momentum is separated in a linear and angular momentum. The linear momentum is equivalent to Newton's second law of motion and couples the force applied on a body Ω to its acceleration.

$$\rho \frac{d\mathbf{v}}{dt} = div(\boldsymbol{\sigma}) + \rho\mathbf{b} \tag{2.13}$$

The left part of the equation, called inertial or kinetic term, represents changes in momentum. $div(\boldsymbol{\sigma})$ is the net force resulting from the divergence of the stress field and $\rho\mathbf{b}$ is the volumetric force.
The conversion of the angular momentum can be shown by multiplying the cross product of the current position vector $\mathbf{x}$ with equation 2.13. Thereby can be shown that the Cauchy stress tensor $\boldsymbol{\sigma}$ is symmetric [12]:

$$\boldsymbol{\sigma} = \boldsymbol{\sigma}^T \tag{2.14}$$

FEM Formulation

The basic formulations of chapter 2.3.2 are non-linear differential equations that are difficult or impossible to solve analytically. An approximative solution is provided by the finite element method (FEM) by replacing the exact conservations equations with the so-called 'weak form'. The continuum is subdivided into discrete elements with nodes at the edges. Their physical response to external forces or displacements is modelled with shape functions (see section 2.3.2). The more elements are used and the better those shape functions approximate reality, the more exact is the solution. In the subsequent sections, only linear equilibrium problems are presented [12, 4, 55, 13]. In order to account for history-dependent material properties and an updated Langrangian approach is chosen.

Principle of Virtual Power

In the following, the 'weak form' is derived which is used to solve the mechanical problem based on the momentum equation as demonstrated in [13]. The linear conservation of momentum (equation 2.13) frames the strong form together with the velocity and the stress (traction) boundary

condition:

$$\rho\dot{\mathbf{v}} = div(\boldsymbol{\sigma}) + \rho\mathbf{b} \quad \text{in} \quad \Omega \tag{2.15}$$

$$\mathbf{v} = \bar{\mathbf{v}} \quad \text{on} \quad \Gamma_v \tag{2.16}$$

$$\boldsymbol{\sigma}\mathbf{n} = \bar{\mathbf{t}} \quad \text{on} \quad \Gamma_t \tag{2.17}$$

Firstly, the momentum equation 2.15 is multiplied with a test function $\delta\mathbf{v}$ representing the virtual velocity and then integrated over the current domain Ω:

$$\int_\Omega \delta\mathbf{v}\rho\dot{\mathbf{v}}d\Omega = \int_\Omega \delta\mathbf{v}div(\boldsymbol{\sigma})d\Omega + \int_\Omega \delta\mathbf{v}\rho\mathbf{b}d\Omega \tag{2.18}$$

The first term on the right side of equation 2.18 can be converted by applying Gauss' theorem and replacing $\boldsymbol{\sigma}\mathbf{n}$ with $\bar{\mathbf{t}}$:

$$\int_\Omega \delta\mathbf{v}div(\boldsymbol{\sigma})d\Omega = \int_{\Gamma_t} \delta\mathbf{v}\bar{\mathbf{t}}d\Gamma_t - \int_\Omega grad(\delta\mathbf{v})\boldsymbol{\sigma}d\Omega \tag{2.19}$$

By substitute equation 2.19 into equation 2.15 the principle of virtual power is obtained [88]:

$$\int_\Omega \delta\mathbf{v}\rho\dot{\mathbf{v}}d\Omega + \int_\Omega grad\delta\mathbf{v}\boldsymbol{\sigma}d\Omega = \int_{\Gamma_t} \delta\mathbf{v}\bar{\mathbf{t}}d\Gamma_t + \int_\Omega \delta\mathbf{v}\rho\mathbf{b}d\Omega \tag{2.20}$$

Each term represents a virtual power. The first term contains the virtual kinetic power δP^{kin}

$$\delta P^{kin} = \int_\Omega \delta\mathbf{v}\rho\dot{\mathbf{v}}d\Omega \tag{2.21}$$

corresponding to kinetic force. The second term describes the total internal power δP^{int} which can also be expressed as [13]

$$\delta P^{\text{int}} = \int_\Omega grad(\delta\mathbf{v})\boldsymbol{\sigma}d\Omega = \int_\Omega \delta\mathbf{D} :\boldsymbol{\sigma}d\Omega \tag{2.22}$$

with $\mathbf{D}$ as the virtual strain rate tensor. The last two terms represent the total external power δP^{ext} and include all external body forces $\mathbf{b}(\mathbf{X}, t)$ and tractions $\bar{\mathbf{t}}(\mathbf{X}, t)$ acting on Γ_t:

$$\delta P^{ext} = \int_{\Gamma_t} \delta\mathbf{v}\bar{\mathbf{t}}d\Gamma_t + \int_\Omega \delta\mathbf{v}\rho\mathbf{b}d\Omega \tag{2.23}$$

Hence, the principle of virtual power can be written as

$$\delta P = \delta P^{kin} + \delta P^{\text{int}} - \delta P^{ext} = 0 \tag{2.24}$$

which is considered the weak form of the momentum equation 2.13. The advantage of the weak form is the elimination or reduction of the requirements for velocity and stress functions in regard of their differentiability [13].

Finite Element Discretisation

The domain Ω is subdivided into finite elements Ω_e in order to discretise the continuum [13]. This step is necessary to solve equation 2.20 numerically. Adjoining elements are connected through nodes. The motion $\mathbf{x}$ of these nodes can be approximated with a shape function $\mathbf{N_I}$ and the position vector $\mathbf{x_I}$ of node I:

$$\mathbf{x}(\mathbf{X}, t) = \mathbf{N_I}(\mathbf{X})\mathbf{x_I} \tag{2.25}$$

By defining nodal displacements $\mathbf{u_I}$ as

$$\mathbf{u_I} = \mathbf{x_I} - \mathbf{X_I} \tag{2.26}$$

the displacement field can be written as

$$\mathbf{u}(\mathbf{X}, t) = \mathbf{u_I}(t)\mathbf{N_I}(\mathbf{X}) \tag{2.27}$$

and the velocity results in:

$$\mathbf{v}(\mathbf{X}, t) = \dot{\mathbf{u}}(t)\mathbf{N_I}(\mathbf{X}) \tag{2.28}$$

As the test function $\delta\mathbf{v}$ is not time dependent, it can be approximated with:

$$\delta\mathbf{v}(\mathbf{X}) = \delta\mathbf{v_I}\mathbf{N_I}(\mathbf{X}) \tag{2.29}$$

An operator $\mathbf{B_I}$ is introduced and defined by $\mathbf{B_I} = \partial\mathbf{N_I}/\partial\mathbf{x}$. Thus, the weak form (equation 2.24) can be expressed as:

$$\delta\mathbf{v_I}\int_\Omega \mathbf{N_I}\rho\dot{\mathbf{v}}d\Omega + \delta\mathbf{v_I}\int_\Omega \mathbf{B_I}^T\boldsymbol{\sigma}d\Omega = \delta\mathbf{v_I}\int_\Gamma \mathbf{N_I}\bar{\mathbf{t}}d\Gamma + \delta\mathbf{v_I}\int_\Omega \rho\mathbf{N_I}\mathbf{b}d\Omega \tag{2.30}$$

Using the arbitrariness of the test function $\delta\mathbf{v}$, the following nodal force balance equation results:

$$\int_{\Omega} \mathbf{N_I}\rho\dot{\mathbf{v}}d\Omega + \int_{\Omega} \mathbf{B_I}^T\boldsymbol{\sigma}d\Omega = \int_{\Gamma} \mathbf{N_I}\bar{\mathbf{t}}d\Gamma + \int_{\Omega} \rho\mathbf{N_I}\mathbf{b}d\Omega \tag{2.31}$$

Equation 2.31 can be split in $\mathbf{f}^{int}$, $\mathbf{f}^{ext}$ and $\mathbf{f}^{kin}$:

$$\begin{aligned} \mathbf{f}^{\text{int}} &= \int_{\Omega} \mathbf{B_I}^T\boldsymbol{\sigma}d\Omega \\ \mathbf{f}^{ext} &= \int_{\Gamma} \mathbf{N_I}\bar{\mathbf{t}}d\Gamma + \int_{\Omega} \rho\mathbf{N_I}\mathbf{b}d\Omega \\ \mathbf{f}^{kin} &= \int_{\Omega} \mathbf{N_I}\rho\dot{\mathbf{v}}d\Omega \end{aligned} \tag{2.32}$$

The discrete equations for the finite element method implementation are usually expressed in the following form:

$$\mathbf{M}\ddot{\mathbf{u}} + \mathbf{f}^{\text{int}} = \mathbf{f}^{ext} \tag{2.33}$$

$\mathbf{f}^{kin}$ is substituted by the constant mass matrix $\mathbf{M}$ multiplied with the nodal acceleration $\ddot{\mathbf{u}}$ or $\mathbf{a}$. Real systems are usually subject to damping effects which can be implemented with a velocity-dependent damping force [12]. Those effects result mainly from viscous damping or internal friction [122]. The most common implementation consists of a constant damping matrix $\mathbf{D}$ multiplied with the velocity $\dot{\mathbf{u}}$:

$$\mathbf{f}^{damp} = \mathbf{D}\dot{\mathbf{u}} \tag{2.34}$$

$\mathbf{D}$ is usually defined as a weighted combination of mass $\mathbf{M}$ and stiffness matrix $\mathbf{K}$ with weighting factors (α_1 and α_2) [13]:

$$\mathbf{D} = \alpha_1\mathbf{M} + \alpha_2\mathbf{K} \tag{2.35}$$

Together with equation 2.33, the general form for the equation of motion results:

$$\mathbf{M}\ddot{\mathbf{u}} + \mathbf{D}\dot{\mathbf{u}} + \mathbf{f}^{\text{int}} = \mathbf{f}^{ext} \tag{2.36}$$

Incremental Implicit Solution

For quasi static systems, the acceleration and velocity terms can be neglected and equation 2.33 can be expressed as [13]:

$$\mathbf{f}^{\text{int}} = \mathbf{f}^{ext} \tag{2.37}$$

This simplified force balance equation has to be fulfilled at all times. By assuming the external force ${\mathbf{f_I}}^{ext}$ is constant during the time increment Δt, equation 2.37 can be written incrementally as:

$$ {}^{t}{\mathbf{f_I}}^{\text{int}} + \Delta{\mathbf{f_I}}^{\text{int}} = {\mathbf{f_I}}^{ext} \tag{2.38} $$

with

$$ \Delta{\mathbf{f_I}}^{\text{int}} = {}^{t+\Delta t}{\mathbf{f_I}}^{\text{int}} - {}^{t}{\mathbf{f_I}}^{\text{int}} \tag{2.39} $$

Note that ${\mathbf{f_I}}^{ext}$ and ${}^{t}{\mathbf{f_I}}^{\text{int}}$ are known and the incremental internal force $\Delta{\mathbf{f_I}}^{\text{int}}$ is unknown but can be approximated with:

$$ \Delta{\mathbf{f_I}}^{\text{int}} = {}^{t}\mathbf{K}\Delta\mathbf{u_I} \tag{2.40} $$

The tangent stiffness matrix ${}^{t}\mathbf{K}$ is defined as:

$$ {}^{t}\mathbf{K} = \frac{\partial^{t}{\mathbf{f_I}}^{\text{int}}}{\partial^{t}\mathbf{u_I}} \tag{2.41} $$

By combining equations 2.39 and 2.40 we get:

$$ {}^{t}\mathbf{K}\Delta\mathbf{u_I} = {}^{t+\Delta t}{\mathbf{f_I}}^{\text{int}} - {}^{t}{\mathbf{f_I}}^{\text{int}} \tag{2.42} $$

Newton-Raphson Scheme

For an incremental displacement $\Delta\mathbf{u_I}$ this equation can now be solved iteratively by using the Newton-Raphson scheme [12]. As an initial conditions we take ${}^{t+\Delta t}\mathbf{K}^{(0)} = {}^{t}\mathbf{K}$, ${}^{t+\Delta t}{\mathbf{f_I}}^{int(0)} = {}^{t}{\mathbf{f_I}}^{int}$ and ${}^{t+\Delta t}\Delta\mathbf{u_I}^{(0)} = {}^{t}\Delta\mathbf{u_I}$. Now the following equation is iterated for $i = 1, 2, ..$ until a satisfactory convergence is reached (through convergence criteria that are not further discussed here):

$$ {}^{t+\Delta t}\mathbf{K}^{(i-1)}\left({}^{t+\Delta t}\Delta\mathbf{u}^{(i)} - {}^{t+\Delta t}\Delta\mathbf{u}^{(i-1)}\right) = {\mathbf{f_I}}^{ext} - \Delta{\mathbf{f_I}}^{\text{int}(i-1)} \tag{2.43} $$

Figure 2.12 shows the Newton-Raphson iteration by illustrating the load displacement relation.
The tangent stiffness matrix $\mathbf{K}$ is recalculated for every iteration, which can be costly. One possibility to reduce computation effort is the modified Newton-Raphson scheme, where $\mathbf{K}$ is not calculated for every iteration [12] but only in the beginning. This strategy reduces the computation cost for the tangent stiffness matrix but also decreases convergences velocity.

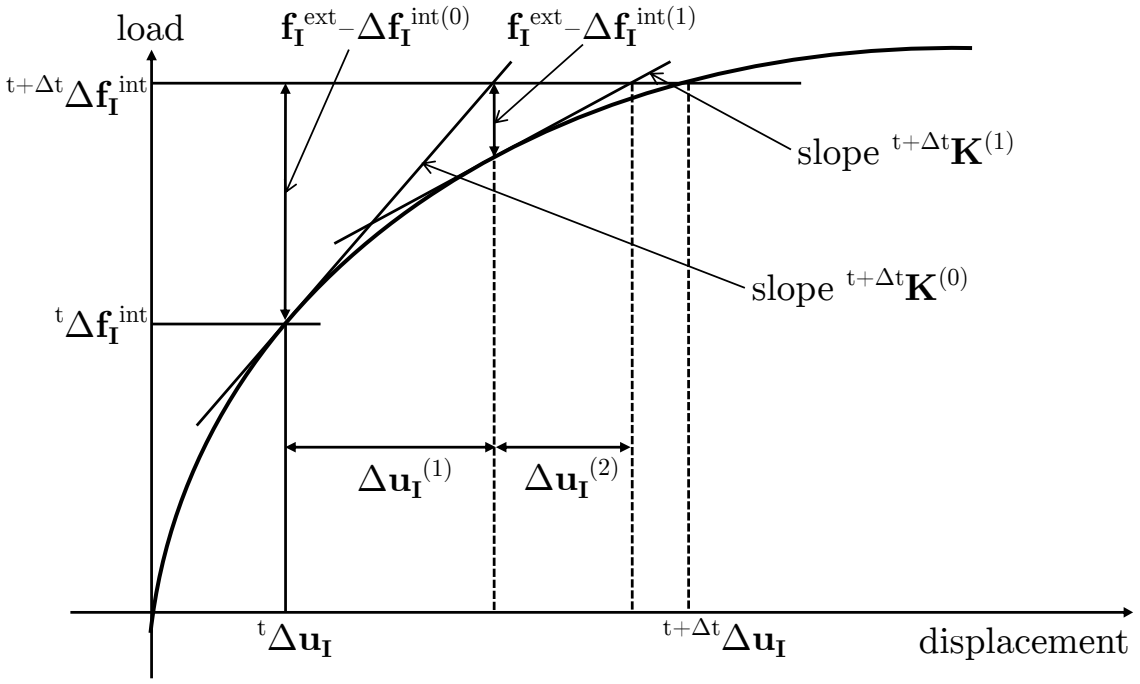

Figure 2.12: Visulisation of the full Newton-Raphsen sheme

2.3.3 The Thermal Problem

The general formulation of the Fourier equation as seen in section 2.2.1 can be written as follows:

$$\rho c_p \frac{\partial T}{\partial t} = div(\lambda grad(T)) + q''' \tag{2.44}$$

q''' is the volumetric generated heat rate. In metal forming processes internal dissipation is mainly generated by irreversible plastic work w_{pl} in form of heat. The transformation factor η can be measured experimentally and set to 0.9 [56]:

$$q'''_{pl} = \eta w_{pl} = \eta \boldsymbol{\sigma} : \dot{\boldsymbol{\varepsilon}} \tag{2.45}$$

During quenching, where phase transformations occur, phase and thus material changes as well as latent heat effects have to be taken into account. Latent heat q'''_{latent} can be included as an internal heat source [59, 114]:

$$q'''_{latent} = \sum_i \Delta H_i(T) \dot{y}_i \tag{2.46}$$

$\Delta H_k(T)$ represents the latent heat that is released during an austenite transformation to a phase i and $\dot{y_i}$ is the corresponding phase growth rate. During heating the latent heat is negative. ΔH is defined in equation 2.47.

$$\Delta H = \int_{T_0}^{T} \rho c_p dT \tag{2.47}$$

An other way to correct for latent heat is trough modification of the term ρc_p [31, 125]. In order to solve the partial differential equation 2.44, an initial condition for the surface temperature

$$T(\mathbf{x}, t = 0) = T_0(\mathbf{x}) \tag{2.48}$$

and additional Dirichlet (first-type) or Neumann (second-type) boundary conditions have to be defined. The Dirichlet condition specifies the Temperature T along a boundary Γ:

$$T_\Gamma = T(\mathbf{x}) \tag{2.49}$$

Alternatively a Neumann condition defines the heat flux q'' to be normal to the boundary of the body. In the case of quenching, q'' consists of convection and radiation. Together with equation 2.1 and 2.2 it can be written as [53]:

$$q''_\Gamma = h(T_\Gamma - T_\infty) + \sigma_B \varepsilon ({T_\Gamma}^4 - {T_\infty}^4) \tag{2.50}$$

h is the heat transfer coefficient and T_∞ the ambient temperature.

FEM Formulation

The heat transfer problem can be solved using the principle of virtual temperatures which is given as [56, 12, 53]:

$$\int_V grad(\delta T) \lambda grad(T) dV = \int_V q''' \delta T dV + \int_\Gamma q'' \delta T d\Gamma + \sum_i \delta T Q^i \tag{2.51}$$

Again, q''' is the combined volumetric and q'' the surface heat flux. The complete derivation can be found in [12]. By introducing the element tem-

perature matrix $\mathbf{H}$ and temperature gradient interpolation matrix $\mathbf{B}$ the terms can be expressed as conductivity $\mathbf{K}_\lambda$ and convection $\mathbf{K}_C$ matrix:

$$\mathbf{K}_\lambda^m = \int_V \mathbf{B}^T \lambda^m \mathbf{B} dV \tag{2.52}$$

$$\mathbf{K}_C^m = \int_\Gamma \mathbf{H}^T h^m \mathbf{H} d\Gamma \tag{2.53}$$

And $\dot{\mathbf{Q}}_e$ the nodal point heat flow contribution:

$$\dot{\mathbf{Q}}_e^m = \int_\Gamma \mathbf{H}_\Gamma^T h^m \mathbf{H}_\Gamma T_\infty d\Gamma \tag{2.54}$$

Similarly internal heat sources $\dot{\mathbf{Q}}_{int}$ and heat flows $\dot{\mathbf{Q}}_C$ are interpolated and integrated across an element:

$$\dot{\mathbf{Q}}_{\text{int}}^m = \int_V \mathbf{H}^T {q_{\text{int}}}^m dV \tag{2.55}$$

$$\dot{\mathbf{Q}}_C^m = \int_\Gamma \mathbf{H}_\Gamma^T {q_C}^m d\Gamma \tag{2.56}$$

The FE-specific formulation for stationary problems can therefore be written as:

$$\left[\mathbf{K}_\lambda + \mathbf{K}_C\right] \mathbf{T} = \dot{\mathbf{Q}}_{\text{int}} + \dot{\mathbf{Q}}_C + \dot{\mathbf{Q}}_e \tag{2.57}$$

Or in short:

$$\mathbf{K}_{th} \mathbf{T} = \dot{\mathbf{Q}} \tag{2.58}$$

In order to account for the transient case heat capacity has to be considered with an additional term:

$$\mathbf{C}\dot{\mathbf{T}} + \mathbf{K}_{th} \mathbf{T} = \dot{\mathbf{Q}} \tag{2.59}$$

The time-dependent numerical integration is conducted with the so-called α-method which relates $\dot{\mathbf{T}}$ and $\mathbf{T}$ with:

$${}^{t+\alpha\Delta t}\mathbf{T} = {}^t\mathbf{T} + \Delta t \left[(1-\alpha)^t\dot{\mathbf{T}} + \alpha^{t+\Delta t}\dot{\mathbf{T}}\right] \tag{2.60}$$

Depending on the choice of α the integration scheme changes:

α	time integration scheme	properties
0	explicit Euler-forward method	conditionally stable
0.5	implicit trapezoidal rule	unconditionally stable
1	implicit Euler-backward method	unconditionally stable

2.3.4 Thermo-Mechanical Coupling

During heat treatment simulations, the used finite element software FORGE solves the mechanical, thermal and metallurgical equations for each time step. This coupling method is called weak coupling. The equations derived in the previous sections are solved in the following sequence [114]:

- Solve mechanical equations
- Solve thermal equations
- Solve metallurgical equations
- Update geometry

Whereas the independent equations for the mechanical part

$$\mathbf{K}(\boldsymbol{\sigma}, \mathbf{T})\Delta\mathbf{u} = \Delta\mathbf{f} + \Delta\mathbf{f}^{th} \tag{2.61}$$

and thermal part

$$\mathbf{C}(\mathbf{T})\dot{\mathbf{T}} + \mathbf{K}_{\lambda}(\mathbf{T})\mathbf{T} = \dot{\mathbf{Q}} \tag{2.62}$$

are solved alternately.

The following nomenclature applies:

$\mathbf{K}$	stiffness matrix
$\Delta\mathbf{u}$	incremental displacement vector
$\Delta\mathbf{f}$	incremental nodal force vector
$\Delta\mathbf{f}^{th}$	thermally induced force vector
$\mathbf{C}$	heat capacity matrix
$\mathbf{K}_\lambda$	heat conductivity matrix
$\mathbf{T}$	temperature nodal vector
$\dot{\mathbf{T}}$	temperature change nodal vector
$\dot{\mathbf{Q}}$	internal and external heat flows

Temperature induced effects on the elasto-plastic constitutive model and thermal strains are included in the mechanical equation 2.61. Furthermore, mechanical properties such as Young's modulus, density and hardening behaviour are temperature dependent. Changes in temperature due to plastic work are considered in the thermal equation 2.62.

Temperature Dependent Plasticity

The strain rate tensor $\dot{\boldsymbol{\varepsilon}}$ consists of an elastic, plastic, thermal, volumetric phase transformation and transformation plasticity part:

$$\dot{\boldsymbol{\varepsilon}} = \dot{\boldsymbol{\varepsilon}}^{e} + \dot{\boldsymbol{\varepsilon}}^{p} + \dot{\boldsymbol{\varepsilon}}^{th} + \dot{\boldsymbol{\varepsilon}}^{tr} + \dot{\boldsymbol{\varepsilon}}^{tp} \tag{2.63}$$

According to the normal rule, the plastic strain increment is proportional to the derivative of the von Mises yield function f with respect to the stress tensor [17]:

$$\dot{\boldsymbol{\varepsilon}}^{p} = \dot{\lambda}\frac{\partial f}{\partial \boldsymbol{\sigma}} \tag{2.64}$$

In the von Mises case, the plastic multiplier $\dot{\lambda}$ is equivalent to the plastic strain rate $\dot{\varepsilon}_{eq}$:

$$\dot{\lambda} = \dot{\varepsilon}_{eq} = \left(\frac{2}{3}\dot{\boldsymbol{\varepsilon}}^{p} : \dot{\boldsymbol{\varepsilon}}^{p}\right)^{\frac{1}{2}} \tag{2.65}$$

In order to relate the stress increment to the strain increment, the fourth order elastic material modulus $\mathbb{C}^e$ is introduced and combined with equation 2.63:

$$\dot{\boldsymbol{\sigma}} = \mathbb{C}^e : \dot{\boldsymbol{\varepsilon}}^e = \mathbb{C}^e : (\dot{\boldsymbol{\varepsilon}} - \dot{\boldsymbol{\varepsilon}}^p - \dot{\boldsymbol{\varepsilon}}^{th} - \dot{\boldsymbol{\varepsilon}}^{tr} - \dot{\boldsymbol{\varepsilon}}^{tp}) \tag{2.66}$$

which can be rewritten and expressed with the total material modulus $\mathbb{C}$ as [17]:

$$\dot{\boldsymbol{\sigma}} = \mathbb{C} : \dot{\boldsymbol{\varepsilon}} \tag{2.67}$$

Note that $\mathbb{C}$ is temperature dependent and may change in each iteration.

Thermal Strain

Thermal expansion or contraction caused by temperature changes induces internal strains $\boldsymbol{\varepsilon}^{th}$ and can be written as [56]:

$$\boldsymbol{\varepsilon}^{th} = \alpha \Delta T \mathbf{I} \tag{2.68}$$

The thermal strain increment can be expressed as:

$$\dot{\boldsymbol{\varepsilon}}^{th} = \alpha \dot{T} \mathbf{I} \tag{2.69}$$

Together with a mixing rule for all present phases [44]:

$$\dot{\boldsymbol{\varepsilon}}^{th} = \sum_i y_i \alpha_i \dot{T} \mathbf{I} \tag{2.70}$$

with α_i as the temperature dependent thermal expansion coefficient of phase i.

Volumetric Phase Transformation Strain

By altering the crystal structure of the materials during phase transformations, the volume may also be affected. For example austenite to martensite transformation leads to an increase in specific volume of almost 5% (shown in section 2.2.2) [79]. The change in volume is modelled to happen instantaneously with the transformation rate. The expansion leads to a spherical deformation $\boldsymbol{\varepsilon}_{tr}$ of finite elements [36]. Incrementally it can be written as

$$\dot{\boldsymbol{\varepsilon}}^{tr} = \sum_i \dot{y}_i \varepsilon_i^{tr,0} \mathbf{I} \tag{2.71}$$

where $\varepsilon^{tr,0}$ is the incremental expansion due to austenite transforming to phase i.

Transformation Plasticity

When phase transformations occur under stress loading, deviations from stress free deformations can be observed. This is true for both diffusive [51] and diffusion-less martensite transformations [86]. Many authors showed experimentally that specimen subject to stress, even way bellow the plastic limit, show significantly higher deformations than ones without external stresses [73, 35, 33, 34, 32, 48]. Deviatoric stress seems to increase transformation temperatures and slowing transformation kinetics, whereas hydrostatic pressure does the opposite. Therefore several works suggest shifts of transformations temperatures, changing transformation constants (see equations 5.2 and 5.5) or modifying the additivity principle due to either deviatoric stress or hydrostatic pressure [58, 1, 32, 106, 90, 60]. The implementation of the transformation plasticity effect was modelled according to [48, 119] where $\boldsymbol{\varepsilon}^{tp}$ is defined incrementally as:

$$\dot{\boldsymbol{\varepsilon}}^{tp} = \frac{3}{2} K f'(y_i) \dot{y}_i \mathbf{s} \tag{2.72}$$

With K as a material parameter, $f(y_i)$ is a growing function and $\mathbf{s}$ as the deviatoric stress tensor. The formulation accounts for the directional influence of transformation plasticity. The f function depends on the phase that is transformed and is either

$$f(y_i) = y_i \tag{2.73}$$

for austenite to ferrite/perlite and

$$f(y_i) = y_i(2 - y_i) \tag{2.74}$$

for austenite to bainite/martensite transformations.

Temperature Dependent Material Behaviour

Phase transformations as well as temperature and strain rate dependencies lead to a highly complex material behaviour during quenching. In order to account for phase transformations it is reasonable to describe the plastic and elastic behaviour as a combination of its current phase composition.

Temperature and phase dependent Young's moduli and Poisson's ratios are used to describe elastic behaviour. A suitable law for the plastic behaviour, one for every phase i, can be written as [114]:

$$\sigma_{y(i)} = \sigma_{0(i)} + H_i {\varepsilon_v}^{n_i} + K_i \dot{\varepsilon}_v^{m_i} \tag{2.75}$$

with σ_0, H, n, K and m as temperature and phase dependent parameters. This model accounts for strain rate and temperature. An equivalent plastic behaviour for k phases is calculated with a mixing rule:

$$\sigma_y^{tot} = \frac{1}{k} \sum_{i=1}^{k} y_i \sigma_i \tag{2.76}$$

Note: during pure forming simulations (blanking or bending), a temperature and strain rate independent material model was used (see section 3).

2.3.5 Buckling Analysis

Observations during quenching experiments hint that some distortion patterns may have their roots in buckling (see chapter 4). The prediction of bucking modi can be conducted with two methods: incremental FE- or buckling-analysis. The incremental approach is closer to reality but costly in terms of computational time. Furthermore, its solution represents solely one single buckling mode. The buckling analysis is able to predict all possible buckling modi and is far less expensive to conduct. However, the method can not identify the exact displacements but only the general mode shape and corresponding buckling load conditions.
The subsequent buckling analysis method is not based on the previously presented incremental finite element method but on a finite element eigenvalue-eigenvector solution [3, 122]. Firstly, an initial reference load and boundary conditions in order to avoid rigid body motions are applied. By conducting a linear static analysis, the stresses are obtained which are needed to form the additional geometric stiffness matrix $\mathbf{K}_G$. The tangent stiffness matrix $\mathbf{K}$ can be split into $\mathbf{K}_G$ and the linear stiffness matrix $\mathbf{K}_L$:

$$\mathbf{K} = \mathbf{K}_L + \mathbf{K}_G \tag{2.77}$$

Ensuing, buckling loads are calculated by solving the following eigenvalue problem:

$$[\mathbf{K}_L + \lambda \mathbf{K}_G]\, \boldsymbol{\varphi} = 0 \tag{2.78}$$

The equation expresses the relationship between the stiffness matrix and the buckling load factor λ which is a multiplier of the reference load. The solution of equation 2.78 yields in m eigenvalues λ_m with corresponding eigenvectors $\boldsymbol{\varphi}_m$ containing the buckling displacement shape of the m-th mode. The amount of possible solutions m is defined by the degrees of freedom of the system, but only the lowest eigenvalues are relevant as they represent the most likely buckling modi. The problem is usually solved using the Lanczos method (see [12]).

3 Thermo-Mechanical Material Characterisation

As mentioned in chapter 2, the material properties are interconnected with all three physical fields: mechanical, thermal and metallurgical. Therefore it is apparent that a profound material description is essential. In the following sections various tests are presented to characterise the material in respect to the mechanical and thermal properties. All experiments were realised with cold rolled C60E/1.1221 steel. The material is well hardenable and hardness values can achieve between 700 HV - 900 HV depending on the quenching process [43]. Its main field of application lies in general mechanical and automotive engineering. A chemical analysis was performed according to EN 10204 [39], the results are listed in table 3.1. All measured values are in the nominal range.

Table 3.1: Measured chemical composition in % of C60E steel

element	actual	nominal
Fe	98.209	-
C	0.613	0.57-0.65
Cr	0.27	0.00-0.40
Mn	0.678	0.60-0.90
Si	0.204	0.00-0.40
P	0.017	0.00-0.02
Ni	0.007	0.00-0.40
Mo	0.001	0.00-0.10
S	0.001	0.00-0.01

3.1 Mechanical Properties

The most important mechanical properties including strain hardening behaviour and anisotropy are measured. The hereby obtained data is later used to predict the geometry and stress evolution during forming processes in finite element simulations (see chapter 6). This includes bending and fineblanking operations.

3.1.1 Yield Curve

The yield curve was measured with standard tensile tests DIN 50125 geometry G with an initial measuring length of 120 mm and a material thickness of 3 mm [41]. As all experimental forming processes are performed at room temperature, the yield curve was also measured at 20 °C. In order to avoid high strain rates and temperatures, the blanking experiments were performed at the lowest setting of 3 mm/s. Temperature and strain rate dependency of the yield curve are assumed to have only small influence in the operating window and were therefore neglected.
The yield curve is cut at 4% strain (because of a pronounced yield point) and at the force maximum. The measured curve is then extrapolated with a simplified Hensel-Spittel approximation, which neglects strain rate and temperature dependencies:

$$\sigma_{yield} = A\varepsilon^{m_1}e^{m_2\varepsilon} \tag{3.1}$$

σ_{yield} is the yield stress for the corresponding strain ε. A, m_1 and m_2 are the fitting parameters whose values can be found in table 3.2.

Table 3.2: Hensel-Spittel Fitting parameters

A	m_1	m_2
819.01	0.149	0.0028

The measured curve and the Hensel-Spittel approximation is illustrated in figure 3.1.

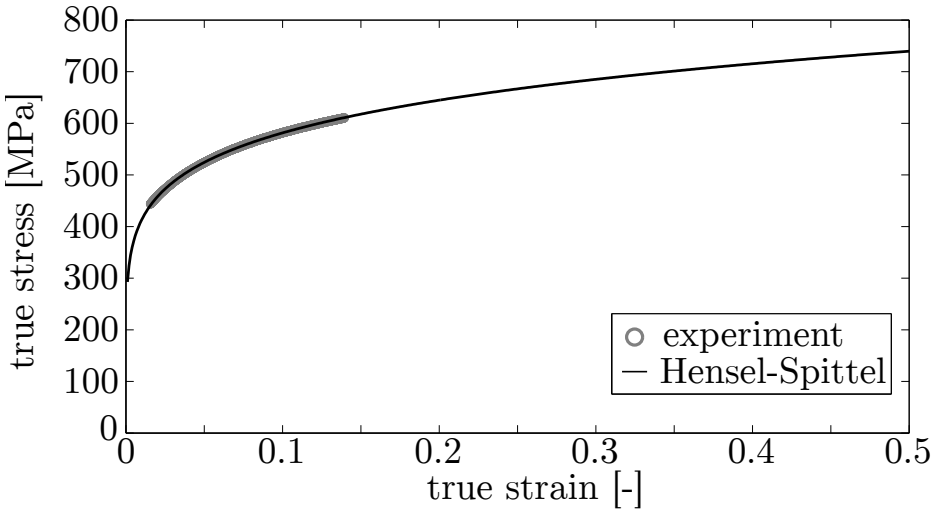

Figure 3.1: Yield curve approximation with Hensel-Spittel

3.1.2 Anisotropy

The R-values or Lanford coefficients were measured for 0°, 45° and 90° in order to characterise the plastic anisotropy of the material [70]. R_α for linear strain paths is defined by

$$R_\alpha = \frac{\varepsilon_{yy}}{\varepsilon_{zz}} = -\frac{\varepsilon_{yy}}{(\varepsilon_{xx} + \varepsilon_{yy})} \tag{3.2}$$

and the normal R-value R_M

$$R_M = \frac{1}{4}(R_{0^\circ} + 2R_{45^\circ} + R_{90^\circ}) \tag{3.3}$$

An R-value close to one means an isotropic hardening behaviour. All measured values in table 3.3 are taken at a true strain of 0.2 and averaged from three independent tensile tests.

Table 3.3: Measured R-Values for C60E

R_{0°	R_{45°	R_{90°	R_M
0.97	0.95	1.36	1.05

With an R_M value of 1.05 isotopic hardening behaviour will be assumed in the forthcoming investigations.

3.2 Thermal Properties

Important thermal properties are quenchability, thermo-mechanical material laws and transformation kinetics. The CCT diagram is a standard method to characterise quenching behaviour. The temperature is accurately controlled and the dilatation during quenching is measured. This change in length of the specimen can be used to identify transformation regions. Additionally, the final hardness and phase structure is determined. The Jominy experiment, a standardised end quench test used to measure quenching behaviour, is modified in order to be applicable for sheet metal. The gradient cooling rate from full water contact to heat exchange mainly with air produces a great amount of information with one single experiment. Both methods have their benefits but also some disadvantages as explicated in the respective sections. The modelling for FE-simulations on basis of those measurements is conducted in chapter 5.

3.2.1 CCT Diagram for C60E Steel

In order to predict phase composition and hardness after heat treatment the continuous cooling transformation diagram for C60E steel was measured. The CCT diagram displays the transformation start and finish points for different phases after continuous cooling from full austenitic structure. The specimen is therefore austenitised and subsequently quenched with different cooling rates. Transformation points can be identified by characteristic dilatation curves as further explained in the experimental procedure. The following measurements were carried out on a DIL 805A/D quenching dilatometer from TA instruments (the sample chamber can be seen in figure 3.2). The cylindrical specimens with a diameter of 4.5 mm and a height of 4 mm are wire cut. Prior to each experiment a thermocouple is welded on the specimen before being placed between the dilatation rods located in the middle of the induction coil.

Experimental Procedure

Firstly, the A_{C3} temperature has to be measured in order to specify a suitable holding temperature that guarantees full austenitisation for all subsequent experiments. The specimen is heated slowly with 3 K/min in the vacuum chamber. During this process the dilation is measured as seen in

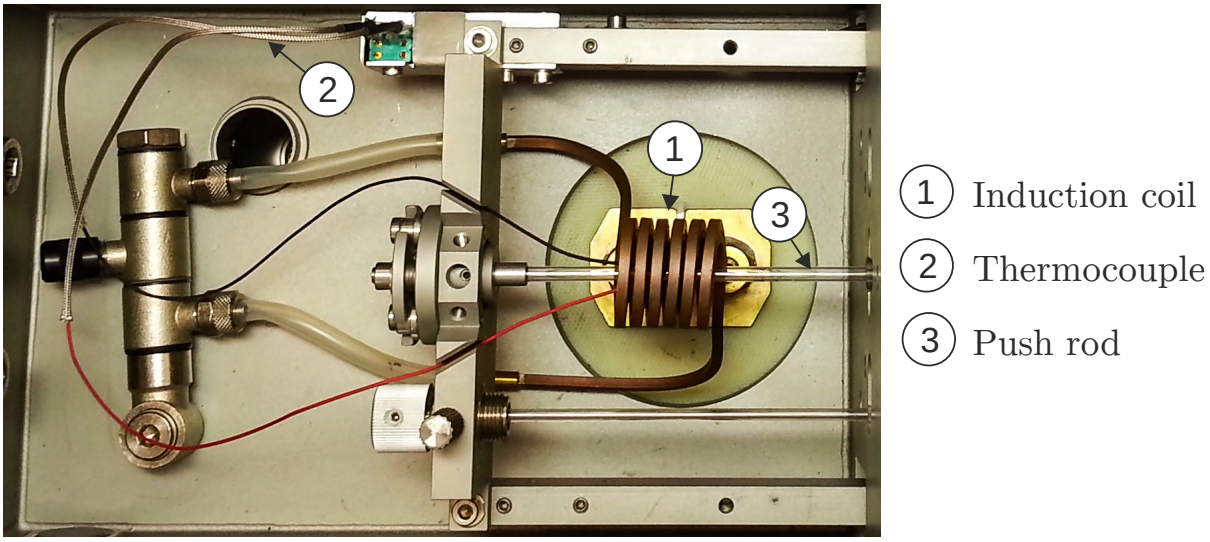

Figure 3.2: Sample chamber of the dilatometer

figure 3.3. Note that this procedure is standardised by the steel test specifications SEP1680 [117]. The correct preparation of specimens, execution of the tests and evaluation of the dilatometric transformations are predefined by SEP1681 [118].

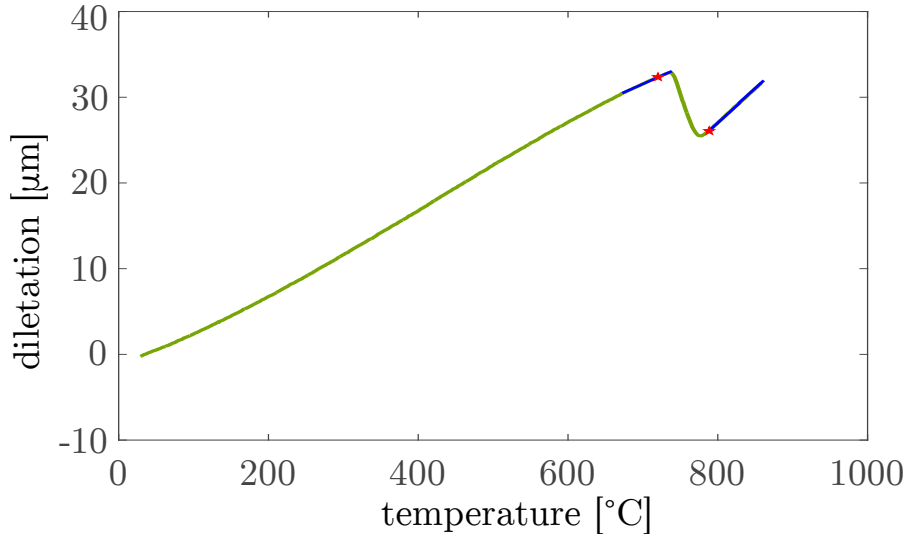

Figure 3.3: Experimental identification of A_{C1} and A_{C3}

As soon as the A_{C1}-temperature is reached, the initial structure of the material transforms to austenite which can be observed by a decreasing length (first red star from left). After complete austenitisation, when A_{C3}-temperature is achieved, positive dilatation resumes (second red star). A_{C1}-

temperature can be identifies at 720 °C and A_{C3} at 790 °C.
In agreement with the standard [117] and the measured A_{C3}-temperature, the design of the experiments was done as shown in figure 3.4. The austenitisation temperature has to be above A_{C3} and is set to $T_{aust} = 850\,°C$. The probes are heated to T_{aust} within two minutes. After a ten minute holding time, to ensure full austenite phase structure, the quenching with various cooling rates takes place.

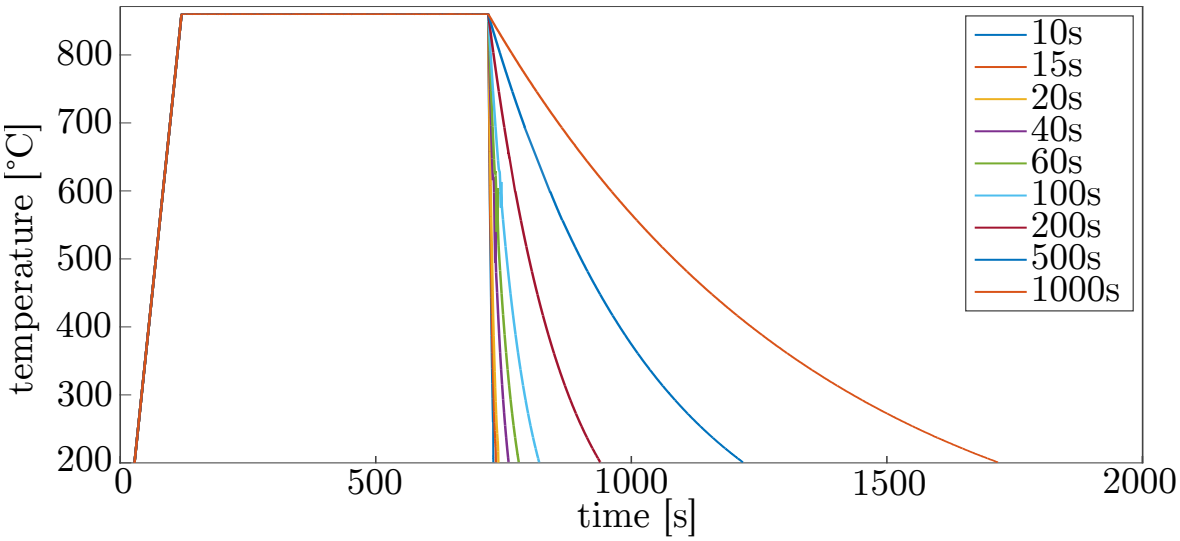

Figure 3.4: Design of experiments for the CCT diagram

The experiments were carried out within the scope of a preliminary investigation [115]. After each quenching experiment the Vickers hardness (HV10) was measured and the phase composition was determined with micrographs. Figure 3.5 shows the microstructure of two distinctive specimens quenched from 850 °C to 200 °C in 10 s respectively 100 s with 500 times magnification. Due to the fast quenching (left micrograph) austenite is transformed to almost pure martensitic structure. The ferritic/perlitic structure of the right micrograph results from slower, diffusion controlled transformation.
Transformation points for all phases are determined the same way as shown for the austenitisation. The identification during transformation from full austenite to perlite and ferrite, at the example of a 40 s quenching time experiment, can be seen in figure 3.6. The red crosses represent transformation points. The graph has to be read from right to left, starting with full austenite at 850 °C. The first deviation from a straight line at 644 °C

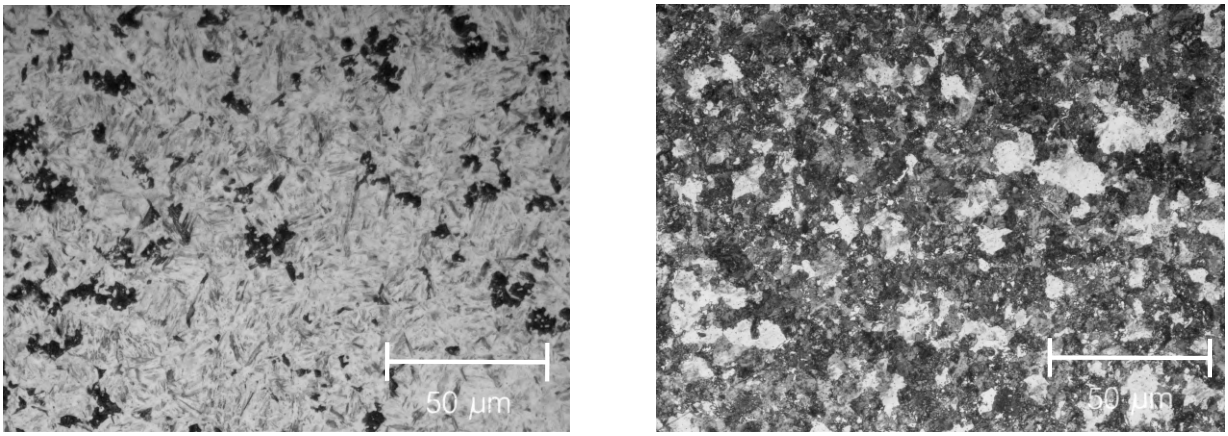

Figure 3.5: Micrographs for 10 s and 100 s quenching time (scale bar 50 µm)

is the beginning of austenite to ferrite transformation. Shortly after, at 320 °C, perlite transformation starts. As soon as the measured data begins to follow a straight line again, at 605 °C, the transformation is assumed to be finished. Finally, all austenite is turned into ferrite and perlite.

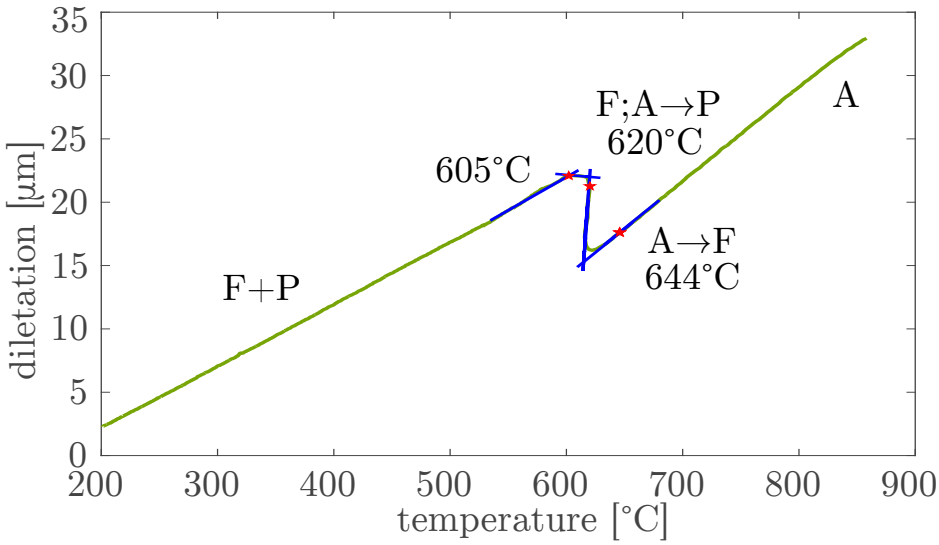

Figure 3.6: Example for identifying transformation points

Assembly of the CCT diagram

As soon as all transformation points for every experiment are identified, the CCT diagram can be assembled by connecting the points to phase areas. After each temperature path, the measured hardness after quenching is

added in white circles. The fully assembled CCT diagram for C60E can be seen in figure 3.7.

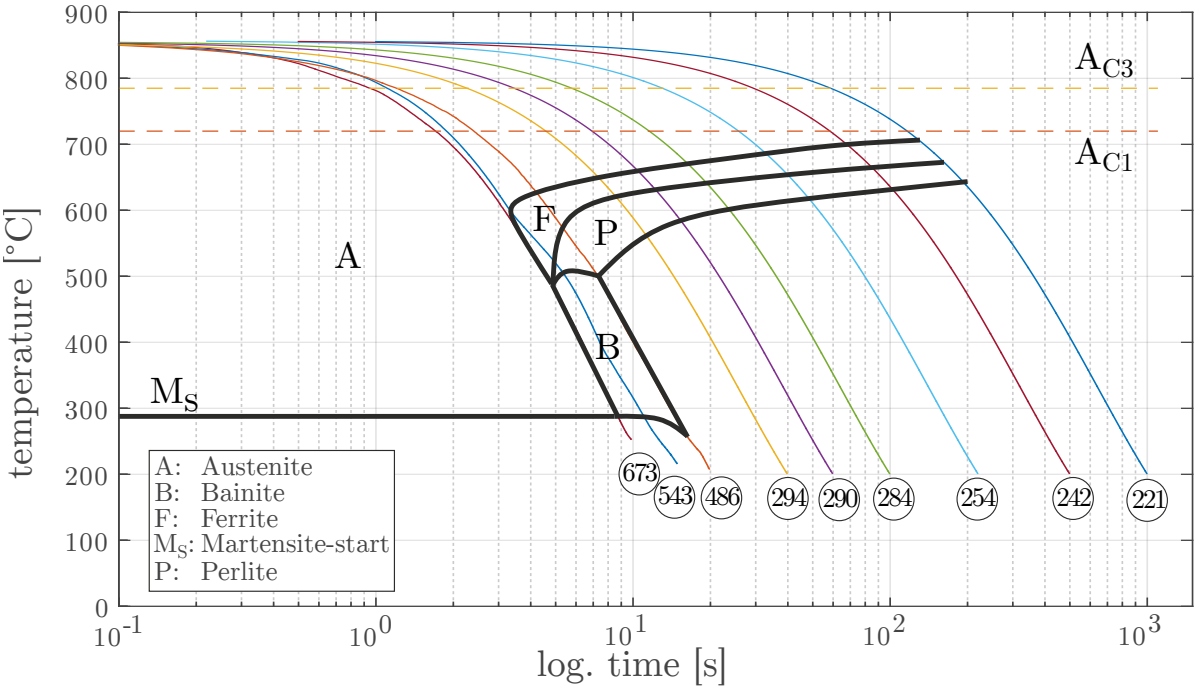

Figure 3.7: CCT diagram for C60E

3.3 Modified Jominy Experiment for Sheet Metal

The original Jominy test aims to measure hardenability of a material, is well established and DIN standardised [38]: A 100 mm long cylindrical specimen with a diameter of 25 mm is austenitised and then quenched at one end with pressurised water. The material close to the quenching surface has a much greater cooling rate than material at the other end of the cylinder, which is mainly exposed to heat transfer with the surrounding air. The thereby resulting gradient in hardness after the test procedure allows to draw conclusions to the hardenability of the material. Because of the amount of information within one single experiment, the test is widely used to validate numerical quenching simulations [92, 81, 26, 94].
In the following, the Jominy test is modified to handle sheet material specimen. The change from cylindrical to sheet material induces some modi-

fications not only in the specimen geometry but also in the experimental setup. A mount was designed to hold the rectangular sheet in its position with a single screw. To prevent the water from wetting anything other than the quenching face, a plate with a slit is placed at one end. The modified Jominy setup is pictured in figure 3.8.

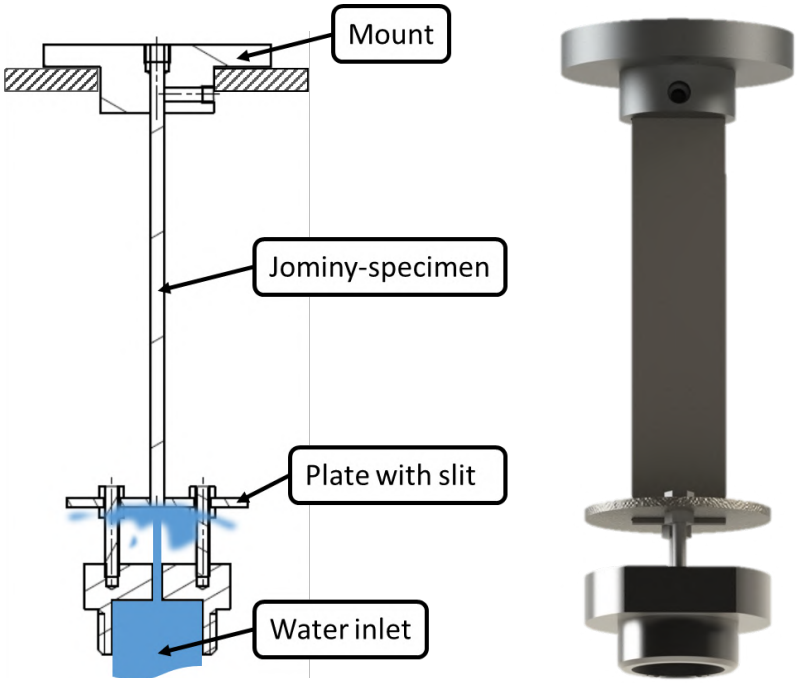

Figure 3.8: Jominy setup (side view on the left and front view on the right)

3.3.1 General Experimental Setup

The general procedure for the test tires to follow all process relevant terms set by the standard despite of modifications. The Jominy specimen is put in an oven and brought to 30 °C - 50 °C above A_{C3} temperature. To ensure full austenitisation, a suitable holding time should be chosen. Kenyeri et al found no impact of initial grain size on final hardness or distortion of regular Jominy specimen, thus a longer holding time may affect grain size but will not alter the test results significantly [65]. When the specimen is ready to be quenched it is inserted into the quenching apparatus. The setup is figuratively shown in figure 3.9.
The transfer from the oven to the quenching apparatus should be as quick as possible to prevent unnecessary temperature loss before quenching. The

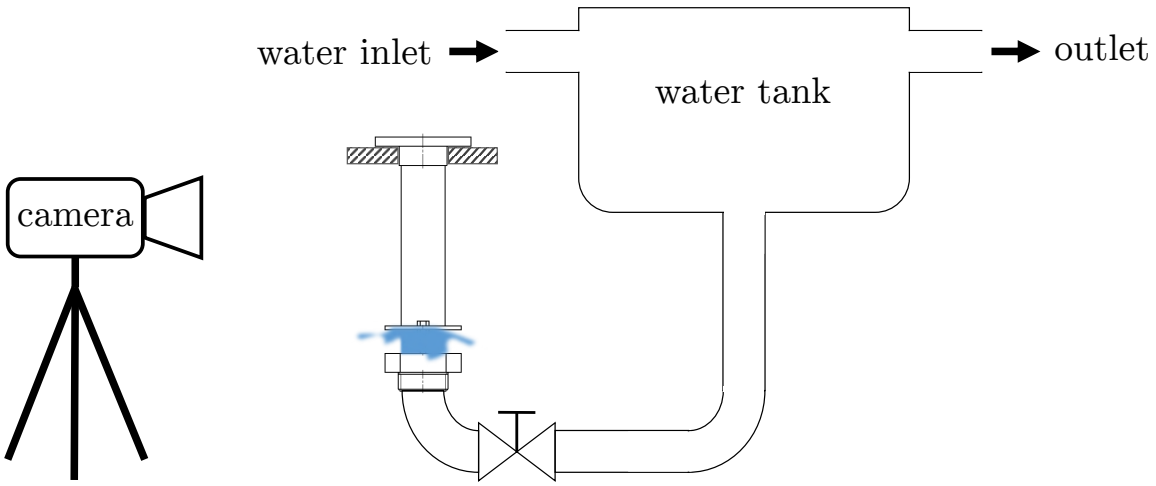

Figure 3.9: Schematic Jominy setup with thermo-camera

water pressure is controlled by an external tank, which has a constant inlet flow of water and an overfall to maintain the same level of water.
By using a thermo-camera type Vario-Therm Head II by Jenoptik it is possible to measure cooling curves for several points (max. 256 x 256 pixel) on the specimen at once. The camera is able to capture data with 50 Hz and an accuracy of <0.1 °C, provided that the emissivity ϵ of the material is known. The camera is positioned to point perpendicular to the wider side of the specimen. As soon as the specimen is transferred from the oven to the mount, the water valve can be opened to begin the quenching process.

3.3.2 Experimental Jominy Procedure for C60E Steel

The rectangular specimens are wire cut of a C60E sheet metal strip. They have the following dimensions: 98 mm x 20 mm x 3 mm. The to-be-quenched specimen is fixed with a setscrew in the mount, before being austenitised in the oven at 98 mm for 15 minutes. The experimental setup is pictured in figure 3.10 with a to-be-quenched hot specimen on the right.
After the experiment the setscrew and the transport hook have to be removed for hardness measurements and micrographs. As the two tend to get stuck they should be covered with antiseize paste prior to the heating. To make sure the oven is on target temperature it was monitored with a thermocouple. The temperature varied from 845 °C-865 °C during the austenitisation process. The transfer from the oven to the quenching apparatus can be accomplished in circa 10 s, which exceeds the standardised

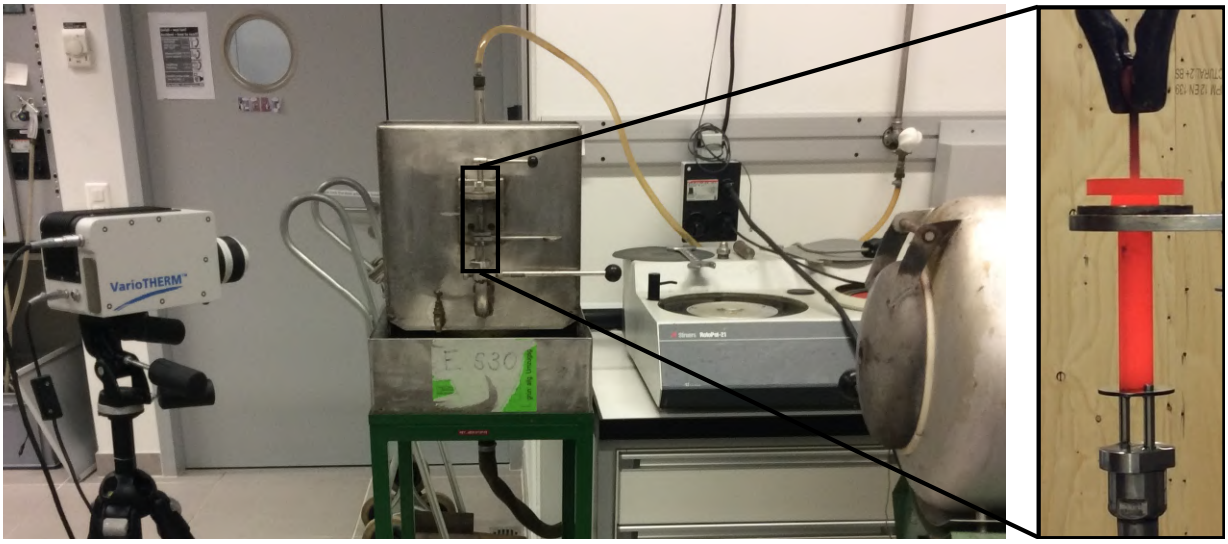

Figure 3.10: Jominy setup with thermo-camera, quenching apparatus, oven and a specimen before quenching

maximum of 5 s for the non-modified Jominy-experiment. The extended transfer time can be explained by the extra effort that is necessary to get the specimen through the slit of the plate. A poka yoke connection between mount and quenching apparatus could possible reduce the transfer time.

Emissivity of C60E steel

In order to get correct temperature information from the camera, the emissivity for the recorded data has to be known. The emissivity ε of steel materials can vary from $\varepsilon = 0.07$ for polished steel, to $\varepsilon = 0.98$ for steel with a strongly oxidised surfaces [11]. To calibrate the emissivity, a heated specimen was recorded with the infra-red camera and an additional welded on thermocouple measured the temperature during slow air cooling. The exact temperature at the measuring point t_t can then be compared to the recorded temperature of the camera εt_c. The measurement of the thermocouple equals to the value of the infra-red camera multiplied with ε:

$$t_t = \varepsilon t_c \tag{3.4}$$

An averaged emissivity of $\varepsilon = 0.76$ was identified.

Test Evaluation

After the experiment, picture data of the camera can be evaluated with the IRBIS Professional software[1]. Figure 3.11 shows the emissivity-adjusted temperature distribution of the specimen during quenching for different stages in time.

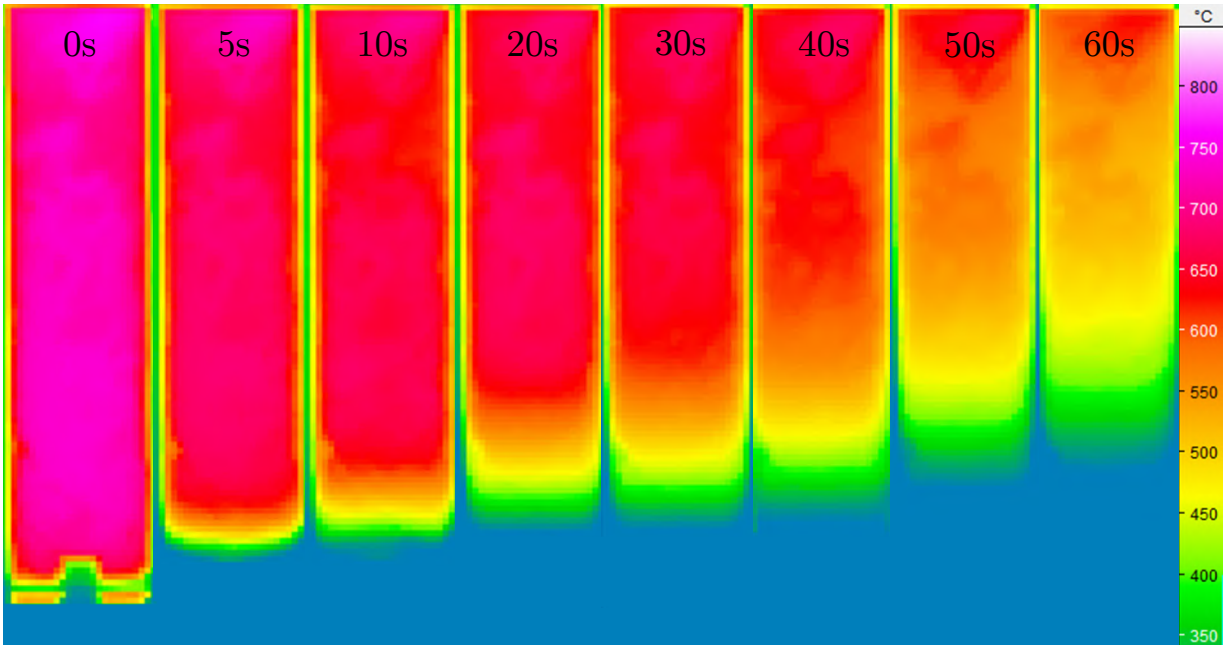

Figure 3.11: Temperature distribution during the first minute of quenching

The first picture from left shows the moment when the water valve is opened. The plate with the slit and its mounting screw are visible in the lower part of the picture. The temperature is close to homogeneous across the specimen in the beginning, but is already slightly below 800 °C. This can be explained by heat loss due to radiation, which is increasing with the surface temperature and the rather long transfer time of 10 s - 15 s. In the lower section, which is closer to the water, temperature drops faster than in the upper area, which is close to the mount where convection is the main cooling force.
To characterise the quenchability for a material, the fast cooling regions are more interesting as they include the most likely cooling rates during industrial applications. The first measurement point that is visible for the camera is located 11 mm from the quenching face. Anything before

[1] www.infratec-infrarot.ch

that point is blocked by the mounting screw and the plate with the slit. The temperature history over time for 11 mm, 25 mm and 35 mm from the quenching surface is shown in figure 3.12. All measurement points are taken in the middle of the specimen as the edges tend to cool faster.

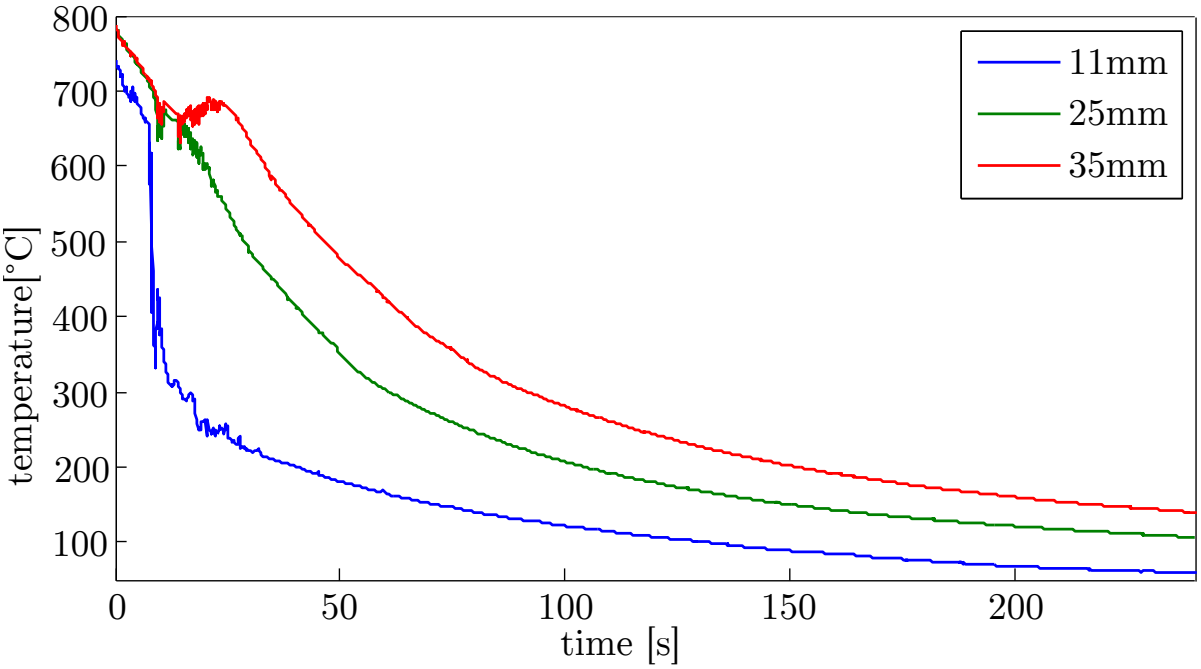

Figure 3.12: Temperature path for three distinct measurement points

During the first 10 s - 15 s of cooling, all three measurement points show similar behaviour. After the water valve is opened, the temperature of the first point (at 11 mm) decreases rapidly, whereas he two points further from the quenching face cool down more slowly. The 35 mm point even increases its temperature after 20 s, which can be explained by a possible exothermic phase transformation. This effect can also be seen after circa 10 s for the 11 mm measurement point. Those results can later be used to validate simulation data by assuring the same temperature paths for experiments and simulations (see section 5.3.3).

3.3.3 Hardness Measurement and Metallurgical Micrographs

After the specimen has reached room temperature, hardness is measured at predefined distances from the quenching face. The measurement points are

shown in figure 3.13 and are taken in the middle of the specimen and are chosen according to the Jominy standard [38]. Additionally, phase content is determined optically with polished micrographs for each measurement point. The hardness distribution after quenching is shown in figure 3.14.

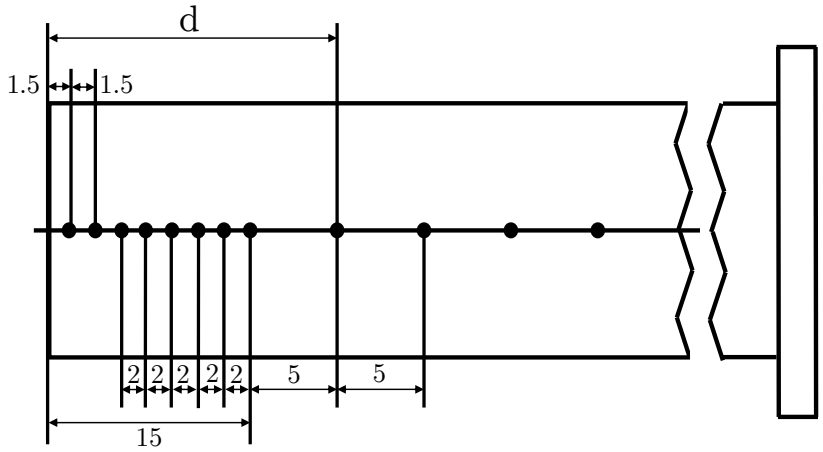

Figure 3.13: Jominy measurement points (quenching face is on the left)

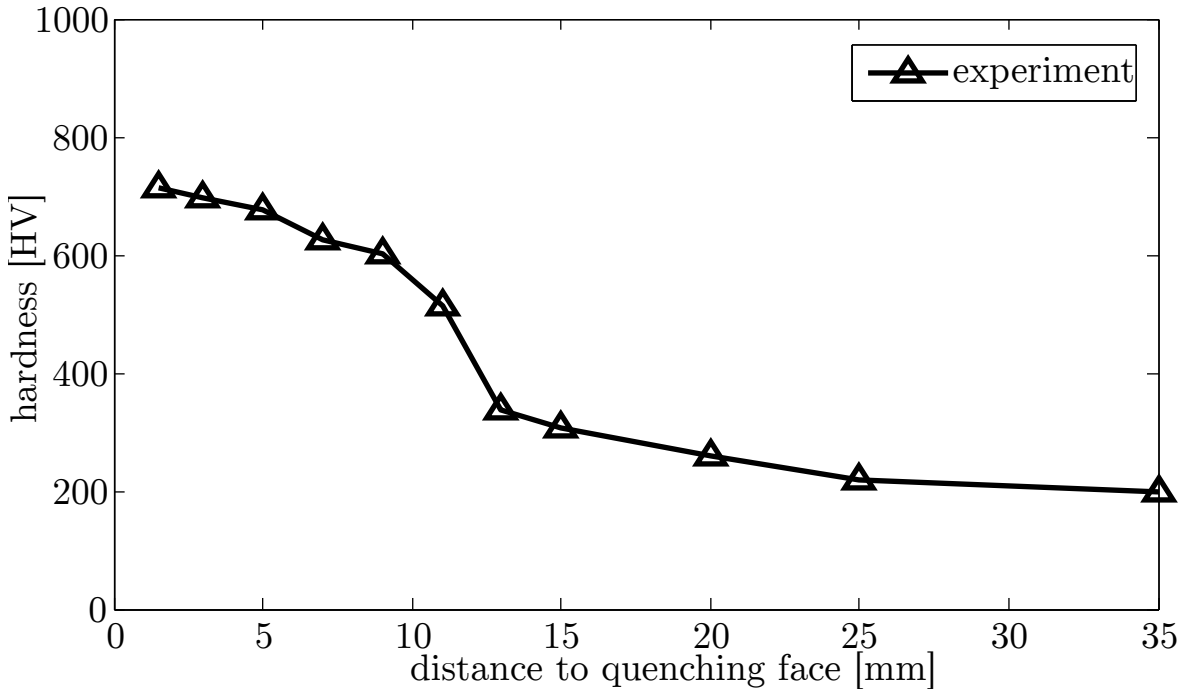

Figure 3.14: Jominy experiment hardness distribution

The hardness achieves its maximum of circa 700 HV at the first measurement point at 1.5 mm. The corresponding micrograph shows full marten-

sitic transformation (see figure 3.15 on the left). The further from the quenching face, the more hardness declines. At 11 mm a steep drop suggests a change in phase composition. In the micrograph on the right of figure 3.15, at 11 mm, combination of martensite and bainite phases are visible. In all micrographs before this point only pure martensite can be determined. Beyond the 35 mm measurement point a dual phase is present consisting mainly of perlite and ferrite with a hardness of circa 200 HV (as seen in figure 3.16).

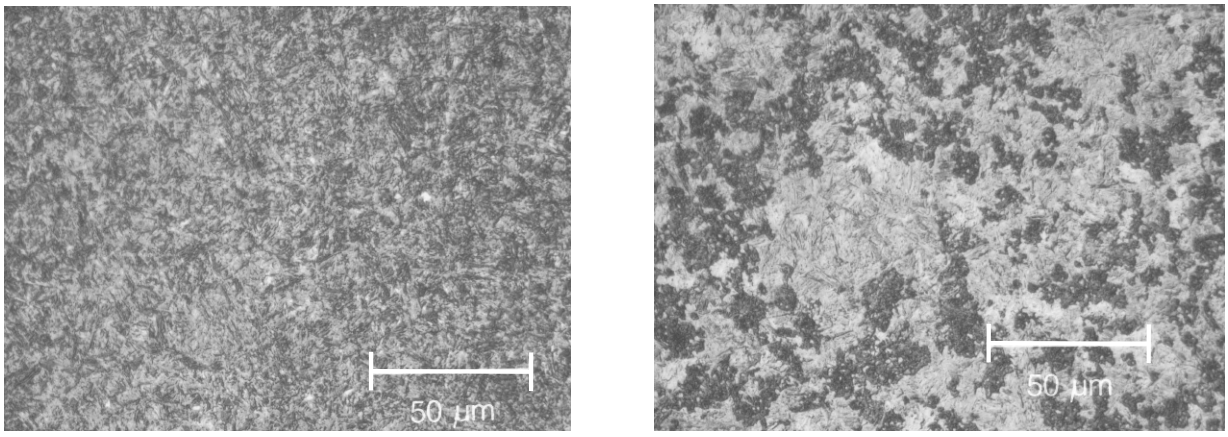

Figure 3.15: Micrographs after quenching at 1.5 mm (left) and 11 mm (right) from the quenching face (scale bar 50 µm)

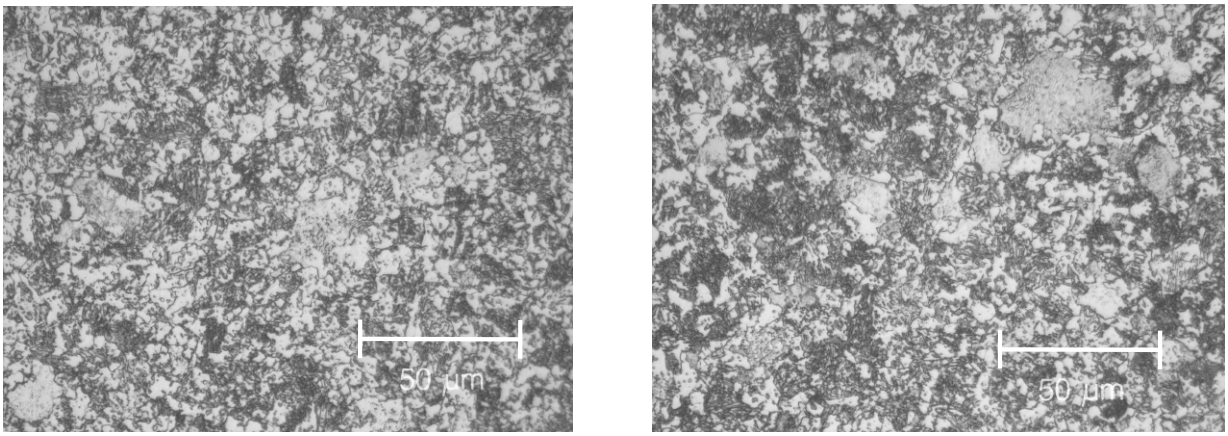

Figure 3.16: Micrographs after quenching at 25 mm (left) and 35 mm (right) from the quenching face (scale bar 50 µm)

The results are consistent with the measured CCT diagram of section 3.2.1.

Figure 3.17 summarises the phase composition after cooling for the measurement points up to 35 mm from the quenching face.

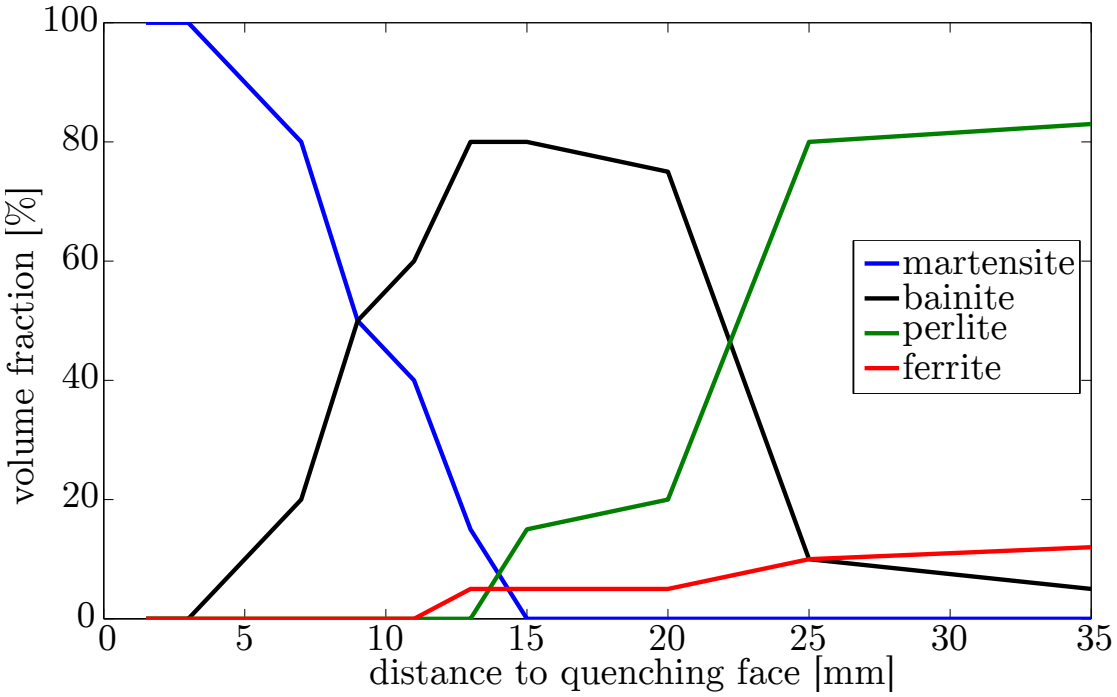

Figure 3.17: Jominy experiment phase composition

The decreasing hardness can be explained by the decline in martensite volume fraction. As mentioned in section 2.2.2, bainite structure depends on transformation temperature and its hardness can reach from 250 HV - 650 HV. This is why bainite content increases, but hardness still decreases steadily. It gains volume fraction from 3 mm and has its peak at 15 mm before declining back towards 0%. Perlite and ferrite both appear after circa 13 mm and increase their volume fraction until reaching an equilibrium after 35 mm that stays constant until the end of the specimen. The results also indicate that, in order to obtain pure martensitic structure, quenching from A_{C3} to the martensite finish temperature has to be faster than what was measured in figure 3.12 for the 11 mm point.

3.3.4 Discussion on the Applicability of the Modified Jominy Experiment

The modified Jominy experiment allows to use sheet metal specimens on an ordinary Jominy quenching apparatus. In combination with a thermal

camera, the setup can be used to measure temperature evolution of numerous points on the specimen with different quenching rates in one single experiment. The gathered data is also valuable to validate finite element simulation data (see chapter 5.3.3). Despite the promising results the author sees room for improvement.
Firstly, the reproducibility of the results strongly depends on the transfer time; the more time passes before the water valve is opened, the bigger the shift of the hardness curve to the left. Transfer times of 20 seconds or more result in a lack of martensite transformation, reducing the meaningfulness of the experiment drastically. By introducing a poka yoke system at the mount and the quenching apparatus, the transfer time could be reduced and at the same time reproducibility could be improved. The screws, which hold the plate with the slit, prevent the camera from capturing temperature paths closer to the quenching face. By shifting the screws to the side, temperature paths resulting in full martensitic structure are measurable. Finally, measurement errors caused by ascending water vapour in front of the camera should be prevented. By increasing the size of slitted plate or by other equivalent measures, vapour can be hindered from blocking the view of the camera.

4 Quenching Experiments to Identify Stochastic and Deterministic Influences

Three different geometries with increasing complexity were chosen in order to identify the main influences on distortion after oil quenching. The experiment series aim to recognise distortion behaviour and separate changes that are either reproducible, and therefore of deterministic nature, or underlay a randomness that is of stochastic origin. As no part is exactly like the other there will always be an amount of unpredictability. Variations may derive from material inequalities or thermal boundary conditions during quenching. The latter is among other factors depending on the position of the part in the quenching basket.

All parts are made of C60E steel, which was characterised in chapter 3. Digital image correlation is used to characterise distortion. In order to track changes in shape and size, specimens are measured before and after heat treatment with the ATOS GOM system. All three parts are illustrated in figure 4.1.

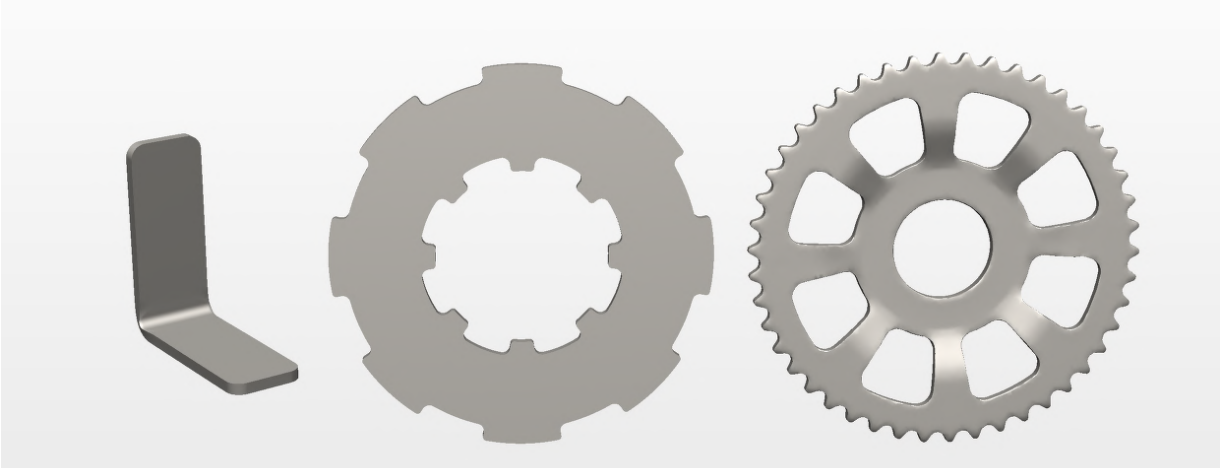

Figure 4.1: Visual representation of the three quenching geometries

In the following, the geometries are introduced. The bracket experiment aims to investigate the influence of residual stresses, induced by a bending process, on thermal distortion. Therefore the angular alteration between both wings before and after quenching is tracked. By eliminating residual stresses with an annealing process prior to quenching, a comparison study with stress free parts can be conducted.
The second geometry, a flat fine blanking part, was created to study the influence of the cutting process and the quenching orientation in the oil bath on distortion. By comparing the fineblanked- with wire cut parts of the same geometry, the influence of fine blanking is analysed. From now on this part will be refereed as the fineblanking test specimen.
The third and last geometry is a part taken from an industrial application. The chain or sprocket wheel congregates bending, cutting and high complexity with several holes and gearing. As both bending and cutting are present, this part is a suitable reference geometry to test the prediction capability of the finite element simulation. The quenching orientation as well as distortion minimisation by heat flow control are investigated.

4.1 Methods

Before presenting detailed experimental procedures and results for each part, the utilised press for fineblanking and bending is presented. The quenching oil and its surface temperature dependent heat transfer coefficient are specified. Two applied positions in the quenching basket are shown. Furthermore, the digital image correlation measurement method and the procedure for evaluating distortion are introduced.

4.1.1 The Press

The bending of the bracket and the fine blanking of the second geometry were performed on a hydraulic Feintool HLT 1250 triple action press with a maximum total force of 4000 kN (illustrated in figure 4.2). The total force is distributed to the effective blanking, the v-ring and the counter punch force. A modular tool allows to change its tool inserts from the blanking part to the bending of the bracket. The technical data of the press is summarised in table 4.1. All bending and blanking parts are produced in manual operation, thus the maximum blanking speed was never used.

Figure 4.2: Feintool HLT 1250 triple action press

Table 4.1: Technical data of the Feintool HLT 1250 press [89]

Characteristic	Value	Unit
Maximum total force	4000	kN
Maximum v-ring force	2000	kN
Maximum counter force	1000	kN
Size of mounting table(length x width)	1250x900	mm
Ram stroke height (min/max)	150/190	mm
V-ring stroke height	40	mm
Counter punch stroke height	40	mm
Tool mounting height (min/max)	370/410	mm
Stroking rate	60	strokes/min
Blanking speed (min/max)	8/80	mm/s

4.1.2 Quenching Agent

Durixol W71HC quenching oil was used for all experiments. It is originally designed for automotive gears and thin walled blanking parts. It is characterised through a low evaporation and a small vapour film phase.

According to the data sheet its optimal operating point is between 50 °C - 110 °C [27]. In order to minimise distortion during quenching it is important to stay in this bandwidth [54]. The initial temperature was held at 55 °C and rose due to the heat transfer during quenching by up to 5 K. The oil bath was permanently agitated. Upon request, Burgdorf GmbH measured the temperature dependent heat transfer coefficient as seen in figure 4.3.

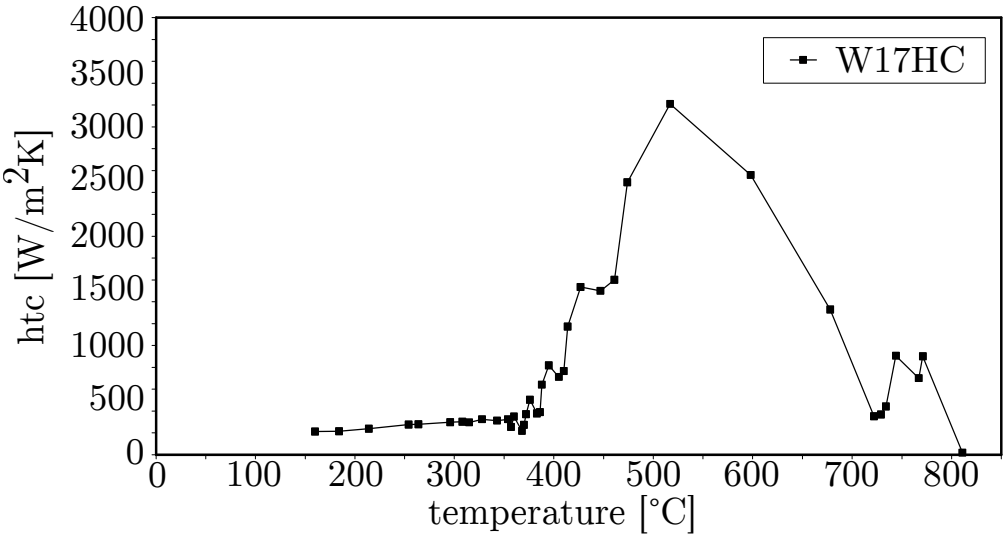

Figure 4.3: Heat transfer coefficient (htc) of Durixol W71HC

The measurement was performed according to the standard ISO 9950 with a cylindrical specimen ($d = 12.5\,\text{mm}$, $l = 60\,\text{mm}$) made of INCONEL 600 on a ivf smart quench testing apparatus. The oil bath was held at a temperature of 60 °C with no agitation. The heat transfer of the oil is subject to thermal effects explained in chapter 2.2.1 which results in the typical bell-shape. The three stages; natural convection at lower temperatures to nucleate boiling and film boiling at higher temperatures are clearly present.

Quenching Direction

Different positioning in the basket during quenching results in an altered heat transfer. Effects of separation and possible vortex build-up may change the parts temperature path significantly. Due to the high surface temperature dependency of the used quenching-oil some of those effects may even be accelerated. Figure 4.4 shows two different placements of the chain wheel in the basket prior to quenching. The left picture shows parts in an upright position and the one on the right shows them lying down.

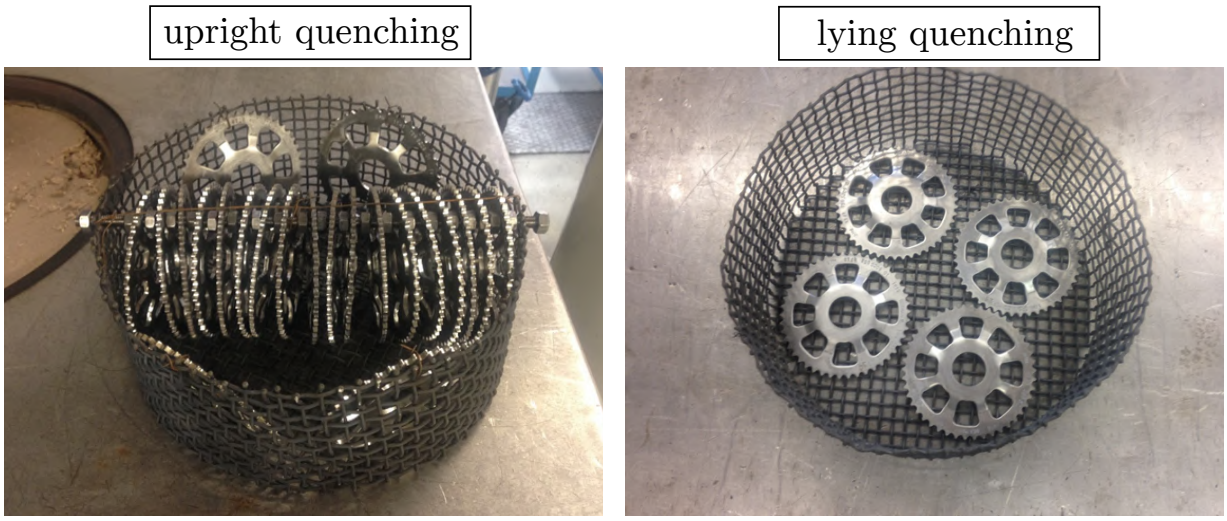

Figure 4.4: Positioning during quenching: lying (left) and upright (right)

All parts in the basket were austenitised before being dropped in the quenching bath. To ensure the same position throughout the whole cooling process, the parts were fixed with wires.

4.1.3 Measurement and Characterisation of Distortion

The majority of the distortion measurements were performed with the ATOS Core 135 system by GOM (see figure 4.5).

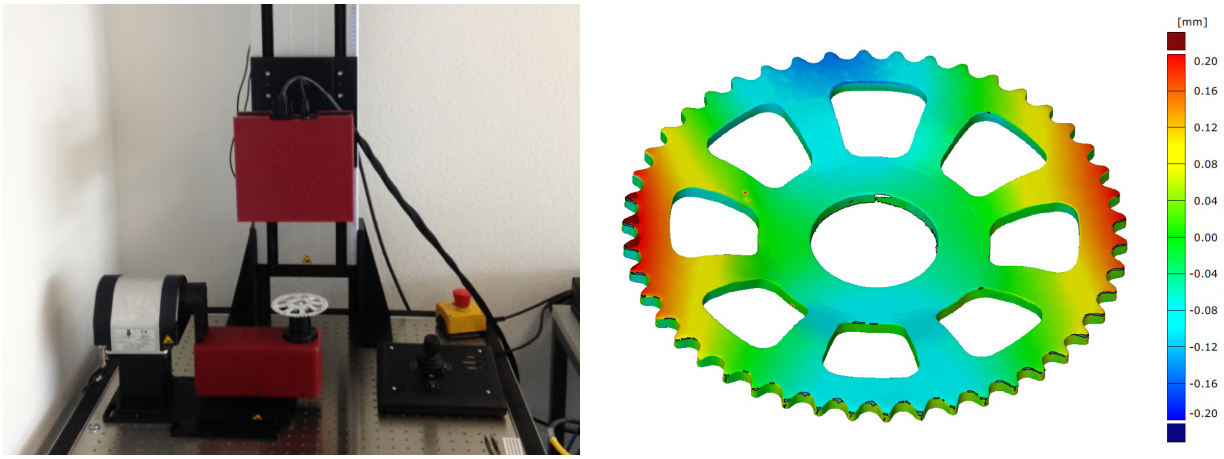

Figure 4.5: ATOS GOM measurement setup

The stereo camera metrology system allows fast and precise surface measurements also for large experiment series. The collected data points are

converted to a 3D polygon mesh on which measurements can be performed. The surface data can be used to characterise distortion by comparing the measured mesh with CAD-data from the reference geometry. Visualising deviations are helpful in understanding the general direction of distortion. Additional measurements, such as roundness or flatness can be done directly on the polygonised mesh. The characteristic properties of the ATOS-system are summarised in table 4.2:

Table 4.2: Technical data of the ATOS CORE 135 system

Characteristic	Value	Unit
Measuring area	135x100	mm
Working distance	170	mm
Point spacing	0.009	mm
Sensor dimensions	206x205x64	mm

To test the process safety, respectively the reproducibility of the system, a chain wheel specimen was measured several times. Before each measurement the cleaned part was sprayed with titanium oxide nano particles for optimal measurement results. Metallic and shiny surfaces are treated that way in order to minimise unwanted reflections during the scanning process. The system shows excellent reproducibility as the maximal deviation between measurements did not exceed 0.004 mm.

4.2 Bending Experiment

The bending experiment aims to investigate the influence of residual stresses from bending on the angular distortion after trough hardening heat treatment. The bracket specimen is a simple bending part formed from a 100 mm x 20 mm rectangular billet with a thickness of 3 mm (as shown in figure 4.6). The material used is the same C60E steel as characterised in chapter 3 and the billets are waterjet cut. Some results of this study were published in 2015 [94].

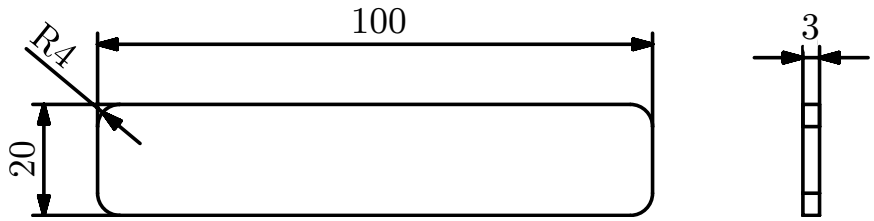

Figure 4.6: Top and side view of the bracket billet before bending

4.2.1 Experimental Design

In total 20 brackets are bended and then equally split into two groups: In the first group, called group A, parts have no further treatment before being through hardened. All residual stresses which are still present after spring-back remain in the brackets. The second group, group B, is subject to stress relief annealing prior to the austenitising and quenching. The annealing process is realised by heating the brackets in an oven up to 600 °C and holding the temperature for 90 minutes. It shall be assumed that remaining stresses from the bending process are thereby mostly being disintegrated. The design of experiments is schematically illustrated in figure 4.7.

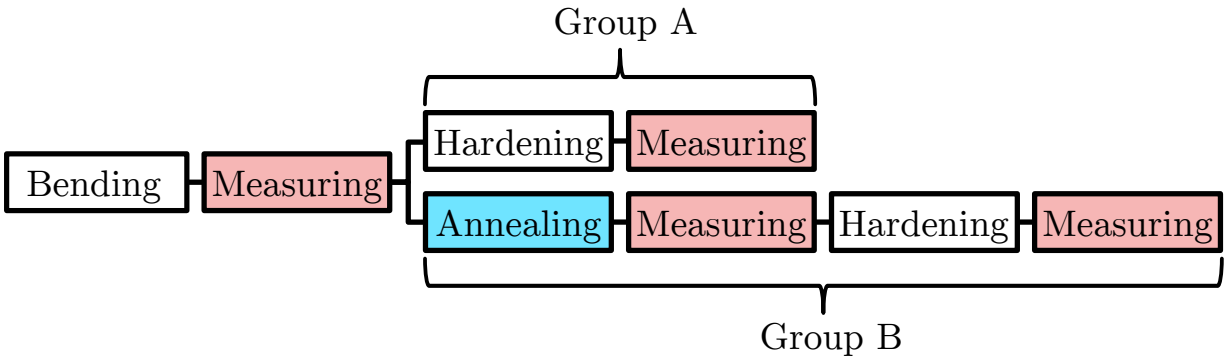

Figure 4.7: Design of experiments for the bracket part

All 20 brackets are measured the first time after bending. The angle from Group B is additionally determined after annealing before undergoing the same through hardening process as group A. All brackets are measured one last time after quenching. The bending and heat treatment process are further explained in the subsequent chapters before the results are discussed.

4.2.2 Bracket Bending

The billets are water jet cut to prevent unwanted forming stresses in the edge region. The bending process is done on the Feintool HLT 1250 press (see chapter 4.1.1) with tools made by Feintool. The tool setup can be seen in figure 4.8. The punch pushes the billet into the two-part die, which is made of two separate pieces for easier installation. The surrounding die plate is constructed in a way that the billet has enough space in the bending zone to flow in width direction. Succeeding the bending process the tools open and the bracket elastically unloads.

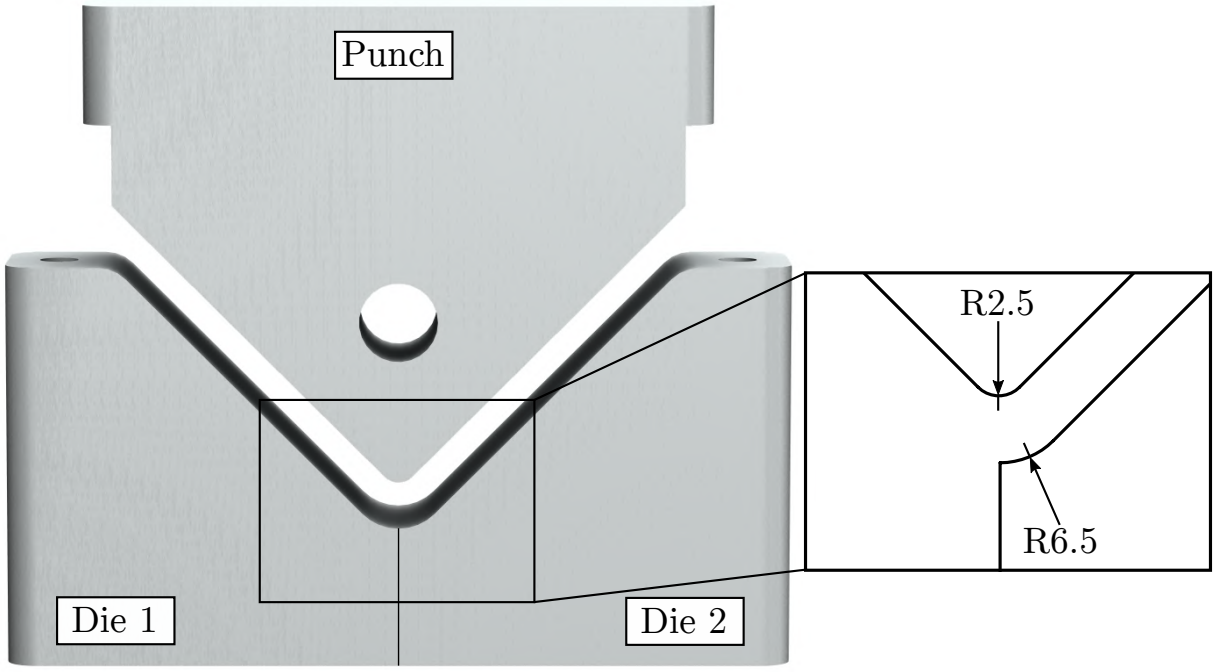

Figure 4.8: Bracket forming tools (only active elements)

4.2.3 Angle Measurement

After bending, the angle between the two sides is determined with the Atos GOM system. The angle was measured by fitting two planes with a Gaussian best fit approximation and subsequently calculate the angle between the two resulting plane normals as seen in figure 4.9. A preliminarily study found this to be to most accurate method to determine the angle [82]. The maximal deviation between four independent measurements of the same bracket was 0.01°.

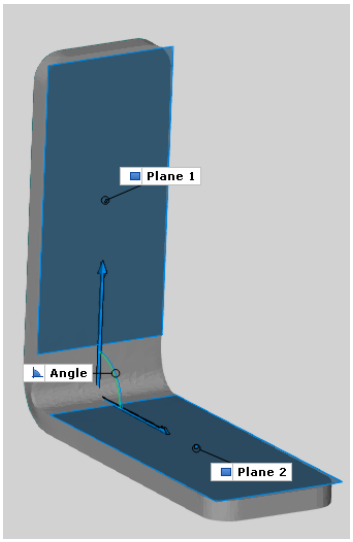

Figure 4.9: GOM measurement of the bracket angle

4.2.4 Bracket Heat Treatment

Group A (see chapter 4.2.1) is austenitised for 30 minutes and then quenched in an oil bath with agitation at 55 °C. Group B is subject to the same heat treatment but undergoes an annealing process prior to the hardening. During which the temperature has to stay below A_{C1} in order to prevent changes in the material but still reliving the residual stresses from the bending process. According to Bargel et al. the temperature has to be set between 580 °C - 650 °C [10]. The temperature was set to 600 °C and the holding time to 90 minutes[1]. The brackets are subsequently slowly air-cooled to room temperature before entering the through hardening process.

4.2.5 Bracket Results and Discussion

The results of the angle measurements before and after hardening for Group A and with an additional measurement point after annealing for group B are shown in figure 4.10.
The blue line in both graphs shows the initial angle after bending. The green line (only in group B) shows the angle after annealing and the red line the final angle after through hardening. These are the main observations:
Although the absolute angle after bending has some fluctuations, the change from the initial to the final angle shows smaller changes in group B com-

[1] As recommended by Bodycote Wärmebehandlung Schweiz AG

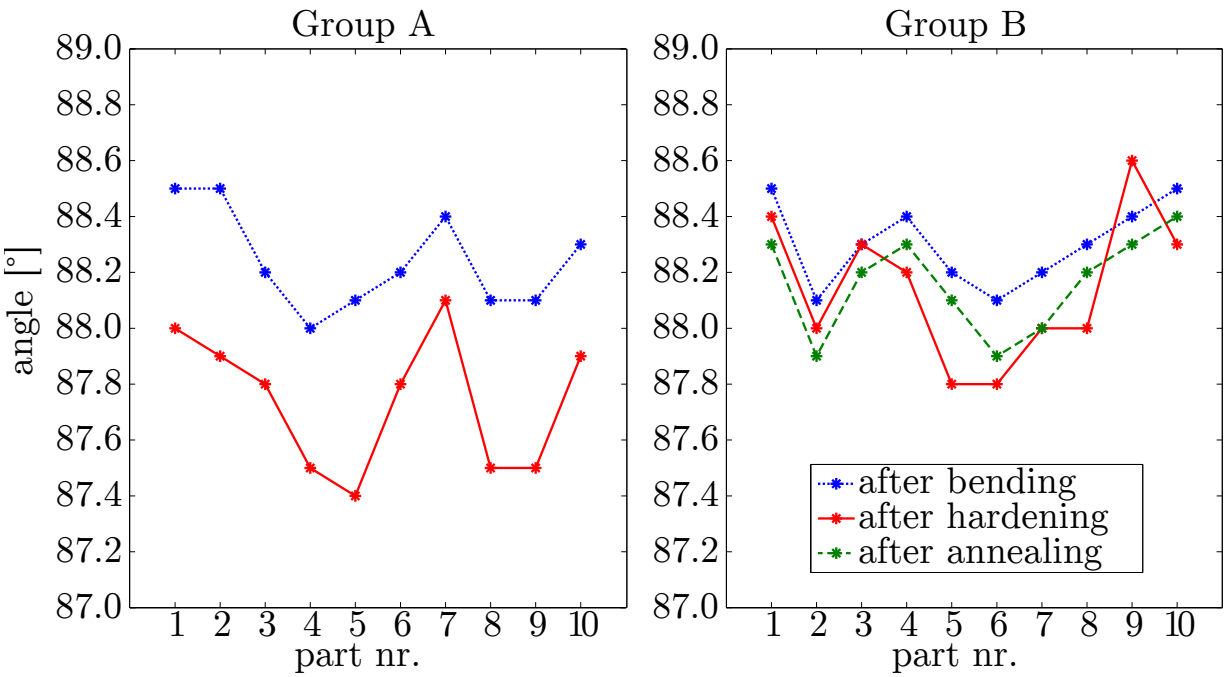

Figure 4.10: Angles before and after heat treatment

pared to group A.
Also, annealing slightly decreases the angle after the bending process, which can be explained by residual stresses that lead to plastic deformation in the bracket after the yield criterion was lowered by the increase in temperature. For better visualisation, mean value and standard deviation of $\Delta angle$ of group A and B are illustrated in 4.11.

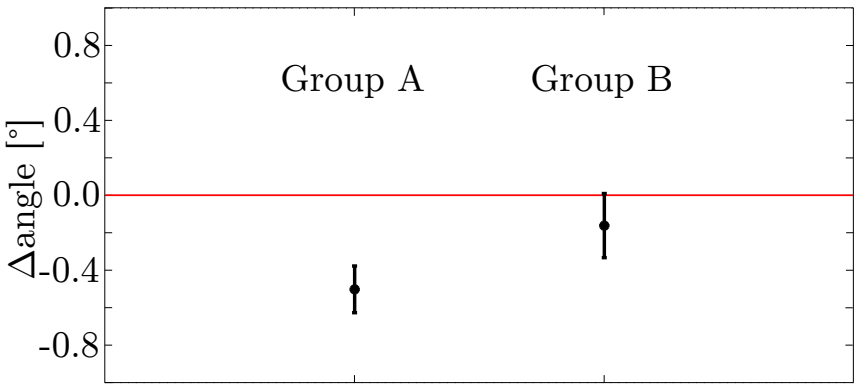

Figure 4.11: Angle changes after heat treatment

The arithmetic average is $\Delta\theta = 0.5°$ for group A without prior anneal-

ing and $\Delta\theta = 0.16°$ for group B. This reduction in angular change shows a significant influence of residual stresses on the distortion of the bracket and may not be excluded when simulating the process with the finite element method. It is conclusive that residual stresses from bending have an impact on the distortion of the bracket. However the influence is rather small compared to spring-back and the necessity of generally taking bending stresses into consideration has to be seen in further experiments. The average angular change from spring back ($\Delta\theta_{SB} = 1.7°$) can exceed the one from heat treatment by a factor of ten and may not be one of the main factors to consider for distortion prediction. Especially because the bracket experiment was designed to be vulnerable to angular changes and may be neglectable for other geometries.

4.3 Fineblanked Test Specimen

The fineblanked test specimen was originally designed to investigate the influence of varying die clearances and edge geometry for fine blanking. For this purpose a set of tools with exchangeable active elements were manufactured. The specimen geometry, as seen in figure 4.12, has an outer and inner toothing but no offset or other non-plane element. Its flatness allows different methods of manufacturing. One half of the specimens is made by fineblanking, the other half is water jet cut. Hence the influence of residual stresses, introduced by the blanking process, on thermal distortion can be investigated. Additionally, two different positions in the quenching basket are compared; upright and lying down. Again, the same C60E steel with a material thickness of 3 mm was used.

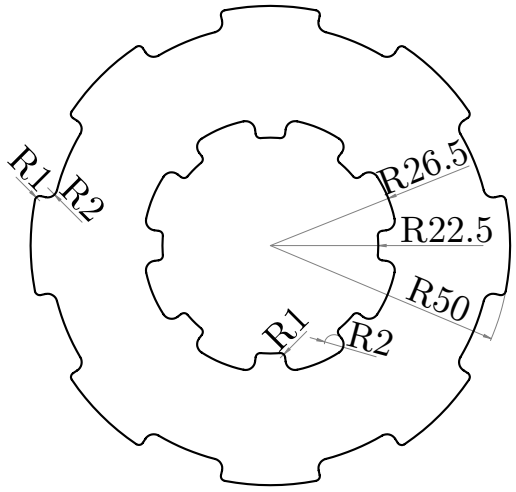

Figure 4.12: Fineblanked test specimen geometry

4.3.1 Manufacturing and Tools

As the die clearance and edge geometry are not in the focus of this work a constant clearance of 0.03 mm and edge geometry L1 with a chamfer of 0.35 mm height and 35° angle is chosen (see figure 4.13). The punch is produced with a sharp edge.
Constructive details of the tools and all possible pairings of active elements can be found in Manopulos dissertation [89]. All fine blanking parts are manufactured on the Feintool HLT 1250 press (see section 4.1.1 for further details).

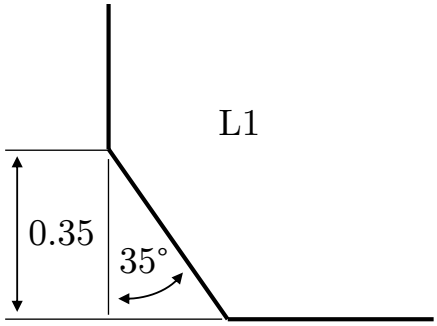

Figure 4.13: Chamfer geometry of the die

4.3.2 Experimental Design

The influence of fine blanking and positioning during quenching are investigated with the fineblanking test specimen experiment series. In order to separate the fine blanking effects on thermal distortion two variations are manufactured. 30 parts are made on the Feintool HLT 1250 with the tools presented in section 4.3.1, this group is labelled F. Another 30 parts are water jet cut and thus have no fineblanking history. They are further referred to as group W. Parts of group W are assumed to have no residual stresses in the cutting zone as well as no die roll or burr. The design of experiment is illustrated in figure 4.14.

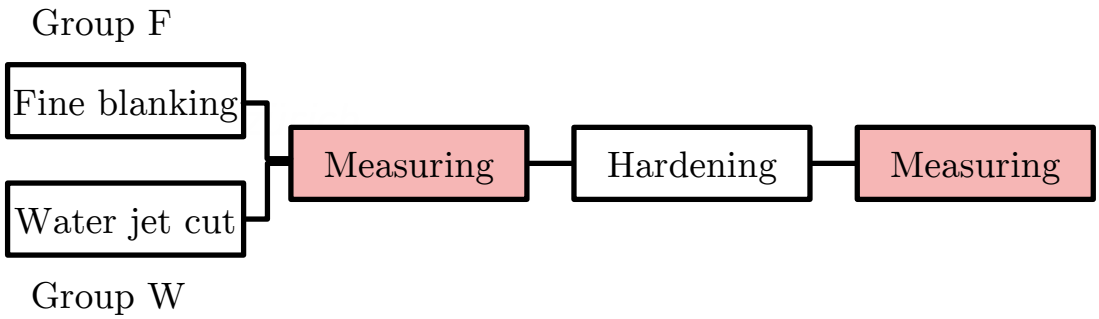

Figure 4.14: Design of experiment

Positioning During Quenching and Heat Treatment

All parts undergo the same heat treatment process as the previously investigated bracket parts: 30 minutes austenitisation at 860 °C with subsequent

quenching in an agitated oil bath at 55 °C. During this through hardening process, 20 out of 30 fineblanked and water jet cut parts are quenched in an upright and 10 in a lying position (as shown in section 4.1.2).

4.3.3 Measurement and Characterisation of Distortion

In order to cope with the amount of measurements, a half automated measurement and analysis technique is used. After scanning the parts from both sides with an automated measuring program, the data for the whole measurement series is analysed automatically according to a predefined protocol. By making a surface comparison from the generated mesh onto CAD-data deviations can be visualised. Figure 4.15 shows such a visualisation of a fine blanked part before heat treatment.

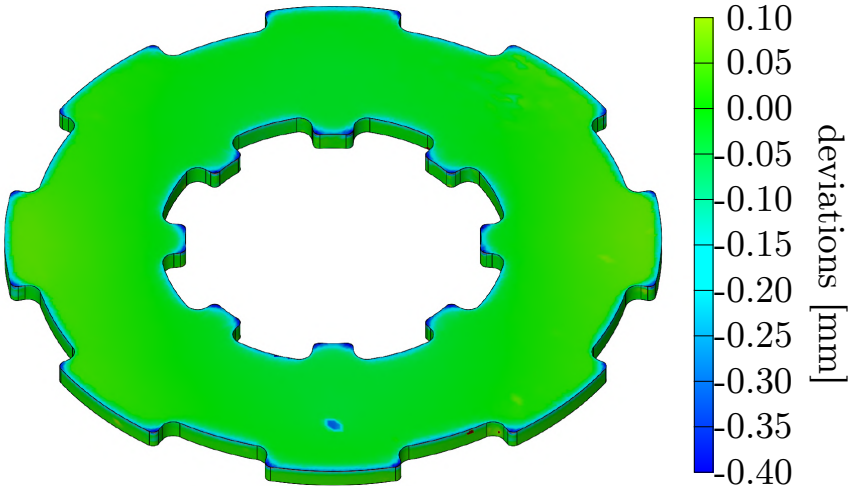

Figure 4.15: Surface comparison from CAD to measured mesh

The part is mostly green which indicates good agreement with the reference geometry. Deviations occur close to the edge due to die roll and near the marker point (small blue area in the lower part) which is not present in the CAD-data. The marker point ensures same orientation when comparing the meshes before and after hardening. Before specific points can be inspected on each part, their measured mesh has to be aligned with the CAD-data through a global best fit. The visualisations are helpful to understand distortion mechanisms but are not best suited for quantitative statements. Additional characteristics such as flatness can be evaluated and compared for the whole series, but they lack the information about deformation. This is why a simplified evaluation method is introduced, which

uses little data but still includes information about deformation patterns. Loosely based on measurements with a coordinate measurement machine, 16 points on a radius of $r = 43\,\text{mm}$ are chosen to describe planar deviations from a reference plane. The points are projected onto the mesh from a constructed circle that is lifted by 10 mm from the reference geometry. The distance between the respective point and its projection is then compared with the nominal value of 10 mm. The measurements are done from both sides to ensure no tilt falsifies the results. In figure 4.16 the top circle and the point-wise projections onto a measured part are illustrated. By plotting all deviations from the 16 measurement points (every 22.5°), planar deformation before and after heat treatment for several parts can be visualised simultaneously. For easier comparison deviations can also be condensed to an averaged, minimal and maximal value.

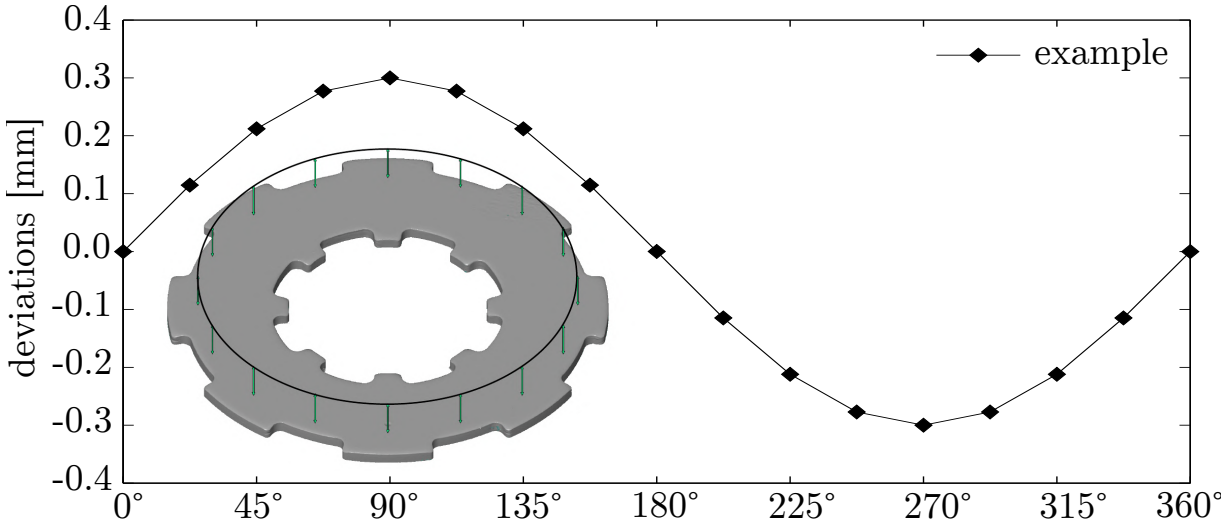

Figure 4.16: Measurement points on a circle with radius r=43 mm

4.3.4 Fine Blanked Test Specimen Results and Discussion

In the following section, deviations before and after the through hardening process are analysed. Firstly, the initial deviations from target geometry are measured. Thereafter the thermal distortions of fine blanked and water jet cut parts are compared. Furthermore, the influence of two different quenching orientations is evaluated and discussed.

Distortion before Heat Treatment

Geometrical deviations from target geometry prior to the heat treatment process are presented in the following. Figure 4.17 shows deviations of the first ten water jet cut and fineblanked parts before heat treatment. The median value, quantiles, minimum and maximum values of all points around the measurement circle are plotted. For better comparison with post-hardened parts the scale is kept constant.

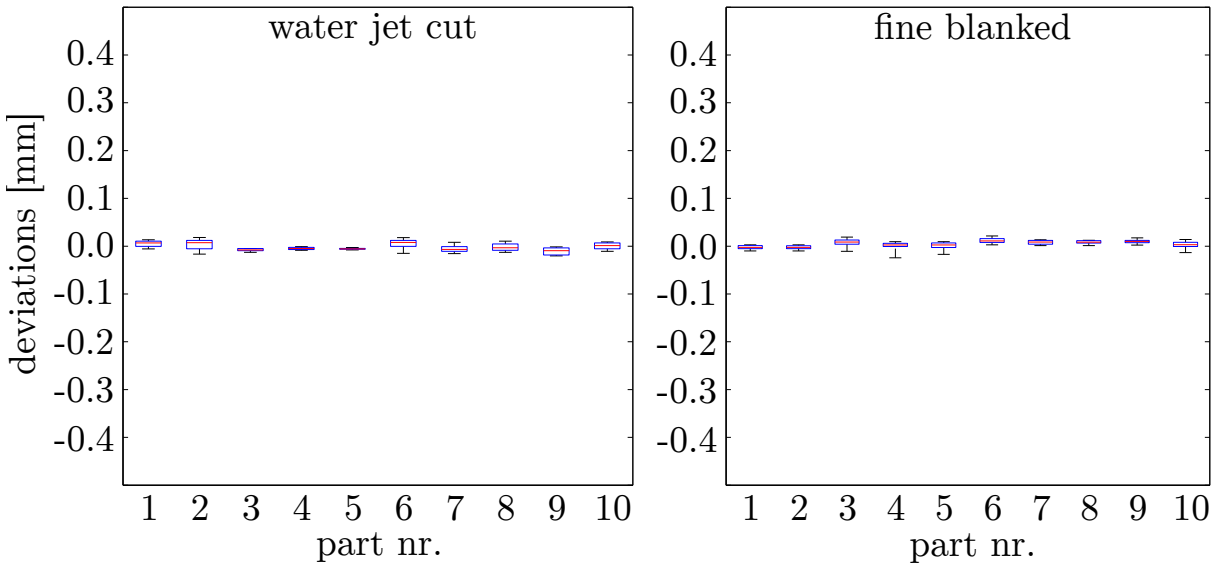

Figure 4.17: Water jet cut and fineblanked parts before heat treatment

The total maximal averaged deviations ($d = max - min$) for all water jet cut and fineblanked parts before heat treatment are $\overline{d}^{wj} = 0.020\,\text{mm}$ and $\overline{d}^{fb} = 0.023\,\text{mm}$. As expected, deviations before heat treatment are generally small compared to tolerances which are commonly specified for the flatness of fine blanked parts ($flatness = 0.05$). No major differences between the two manufacturing methods can be detected.

Distortion after Heat Treatment

Deviations after heat treatment are significantly larger than pre-treatment values and are also subject to higher variation between parts. Figure 4.18 shows exemplary two different specimens after the through hardening process.
Both are fineblanked parts after heat treatment but the part on the left shows substantial higher deviations from target geometry. Figure 4.19

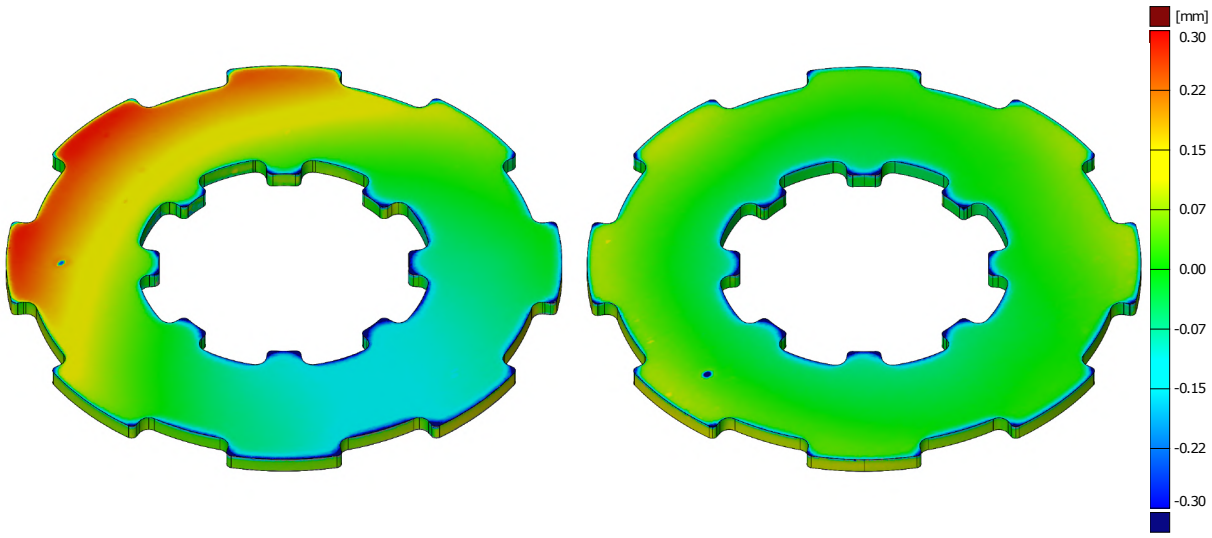

Figure 4.18: Deviations of two fine blanked parts after heat treatment

shows the distribution of maximum deviations of the parts. Whereas two-thirds of the parts have small deviations below 0.1 mm, one-third show significantly higher distortions with up to $D = 0.79\,\text{mm}$.

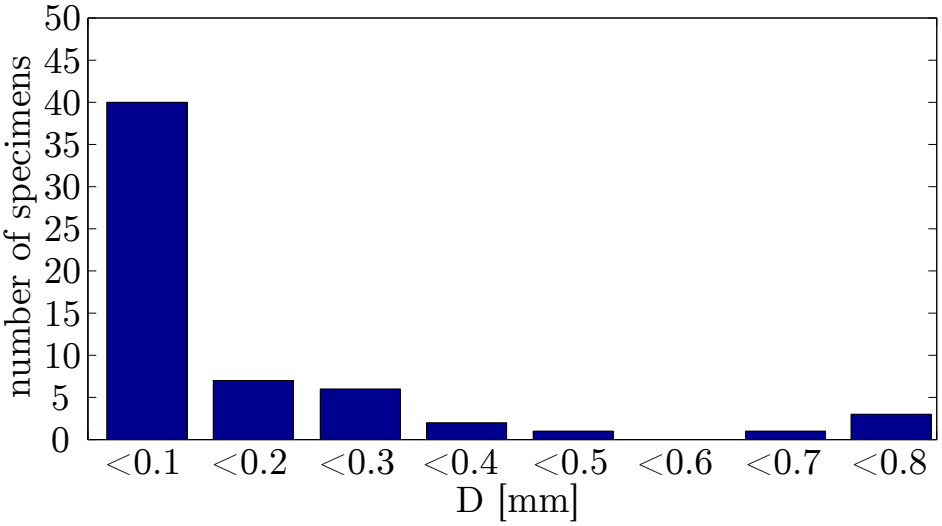

Figure 4.19: Distribution of deviations after quenching

Deviations for all water jet cut parts are show in figure 4.20 and fineblanked parts in figure 4.21.
Parts with number 1-5 and 26-30 are quenched laying down, all other parts were in an upright position (see figure 4.4). The average deviation for all water jet cut parts is $\overline{D}^{wj} = 0.171\,\text{mm}$, but it can be separated in lying

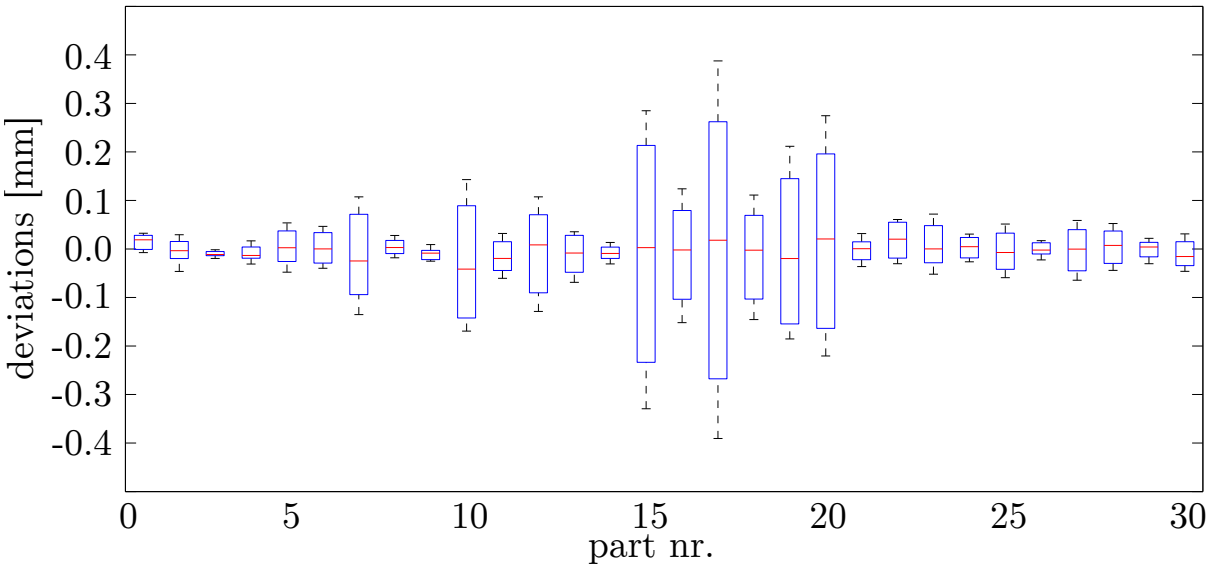

Figure 4.20: Water jet cut deviations after quenching

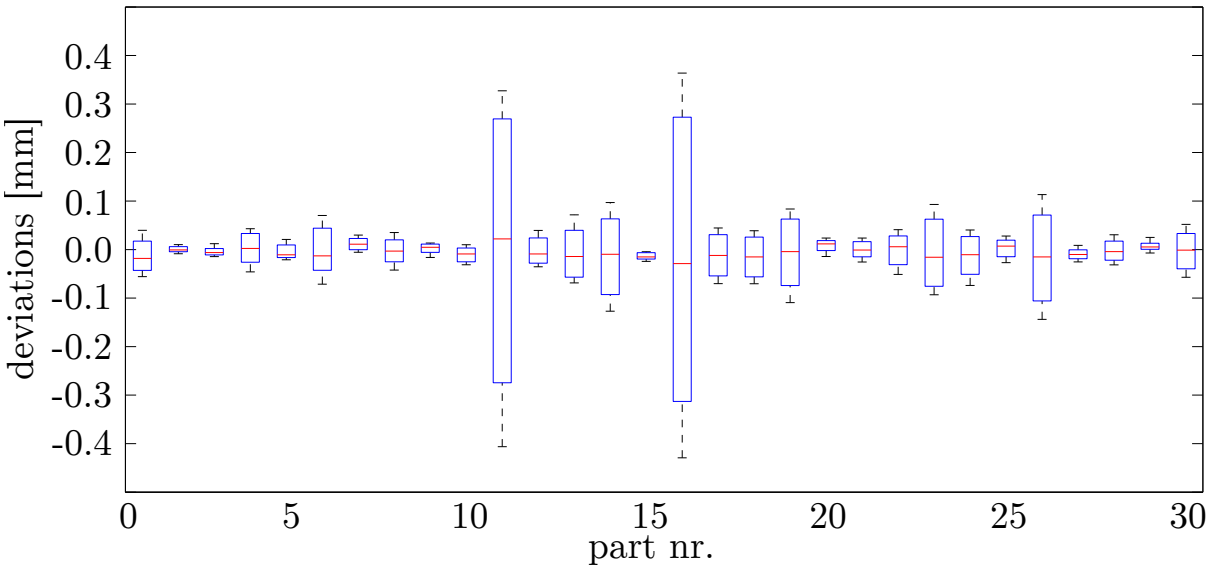

Figure 4.21: Fineblanking deviations after quenching

specimen with an average maximal deviation of $\overline{D}^{wj}_{lying} = 0.067\,\text{mm}$ and hanging with $\overline{D}^{wj}_{hanging} = 0.223\,\text{mm}$. Those results may indicate an orientation dependency although they are contradictory to the usually suggested quenching direction for flat parts. The recommendation for flat specimens is to submerged them with the slim side facing the oil in order to minimise thermal distortion [71].
Similar observations can be made when looking at the fineblanked parts.

The average deviation is slightly lower with $\overline{D}^{fb} = 0.134\,\text{mm}$. Again, part number 1-5 and 26-30 are quenched laying down, the others in an upright position. Parts that are lying during quenching have an average deviation of $\overline{D}^{fb}_{lying} = 0.076\,\text{mm}$ and hanging parts $\overline{D}^{fb}_{hanging} = 0.163\,\text{mm}$. Again, the previously determined orientation dependency is observable.
The average values and standard deviation for fineblanked and water jet cut parts before (initial) and after quenching are shown in Figure 4.22.

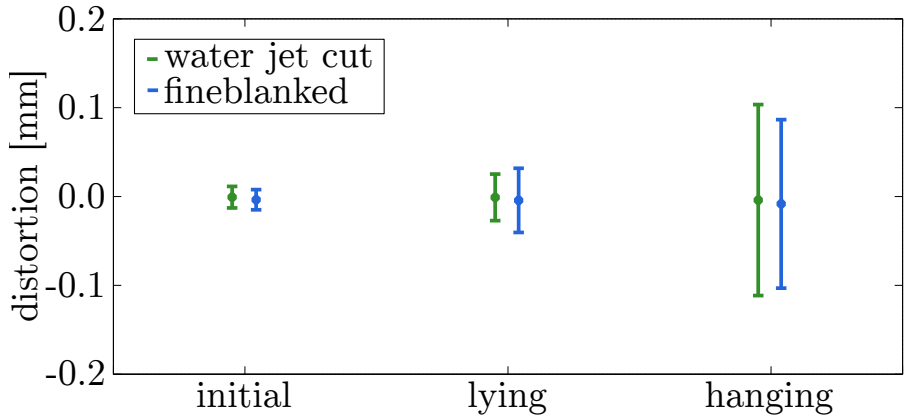

Figure 4.22: Distortion before and after heat treatment

The measurements are split into manufacturing method and orientation during the oil bath. In both cases the parts that were lying during quenching resulted in significant smaller average deformations than ones that were hanging. However, no clear difference between water jet cut and fineblanked parts can be determined. Fineblanking may not change the distortion after hardening because the shear zone is locally delimited and only little material close to the edge is affected by hardening effects and residual stresses. During regular blanking, where no counter punch is present, global residual stresses caused by deflection during the punching process, may be more relevant for distortion after quenching.
Conclusively no coherence between manufacturing method and thermal distortion could be shown. Therefore, no influence of possible residual stresses or material hardening effects, caused by the fineblanking process, were detected. Further investigations have to be performed to be conclusive if residual stresses from fineblanking have to be accounted for in finite element simulations. However, a clear relationship between the two quenching orientations is observable.

4.4 Chain Wheel - Industrial Part

The chain wheel part represents a geometry with industrial complexity, combining bending and multiple cutting processes. The geometry has an offset, a centre hole and 46 teeth. The following experimental investigations are focusing on orientation during quenching and the resulting thermal distortion. The chain wheel is additionally used to examine heat flow controlling during quenching and its effect on distortion. The front and side view of the part are illustrated in figure 4.23. As both other specimens it is manufactured from C60E sheet metal with a thickness of 3 mm.

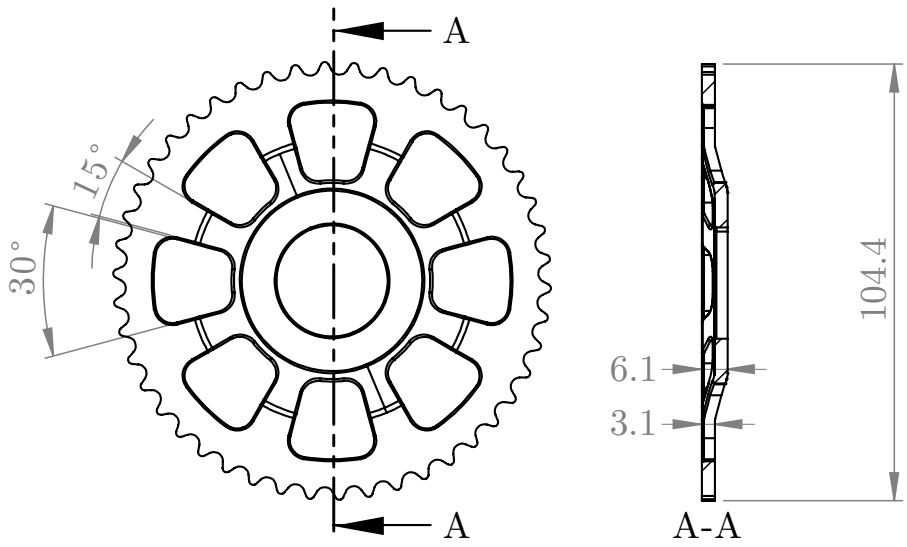

Figure 4.23: Technical drawing of the fine blanked chain wheel

For the sake of completeness all other important dimensions and tolerances of the chain wheel are listed in table 4.3. The part was originally designed with a different material and hardening method in mind, so the tolerances especially for flatness are tough to achieve with through hardening.

4.4.1 Manufacturing and Tools

Due to the complexity of the part it is manufactured in a multi step process that can not be performed on the press introduced in 4.1.1. For that reason the manufacturing of the parts was carried out by Feintool Technologie AG. The process can best be visualised by having a look at the steel strip showing all stages in figure 4.24.

Table 4.3: Dimensions of the chain wheel [mm]

characteristic	value	tolerance
pitch diameter	102.5	-
root diameter	98.5	+/- 0.025
number of teeth	46	-
tooth pitch	7	-
single pitch error	-	0.02
joint flash	-	0.03
flatness	-	0.05
inner diameter	26.5	+/-0.04
total thickness	6.1	+/-0.1
die roll of gearing	-	0.3-0.7

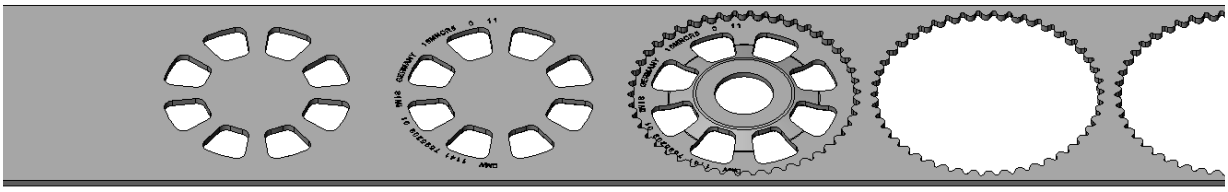

Figure 4.24: Different manufacturing steps illustrated on the steel strip

During the first manufacturing step the steel strip gets punched to create eight circular arranged holes. After each step the strip gets pushed to the next operation. In the second step the edges of the newly generated holes and the inscription on the part gets embossed. At the same time, a v-ring is pushed into the material along the contour line of the inner hole (not visible as it is on the other side). The third step is divided in forming the offset by clamping the strip and moving the tools vertically and a subsequent fineblanking of the gearing and the inner hole. Hereafter the part gets separated from the strip. The cross section of the closed tool with the steel strip inside is illustrated in figure 4.25.

The part is processed from left to right, alike the previous illustration. The circular arranged punches (1) can be partly seen in orange above the die (2). The yellow stamp (3) is used for embossing the inscription in the second

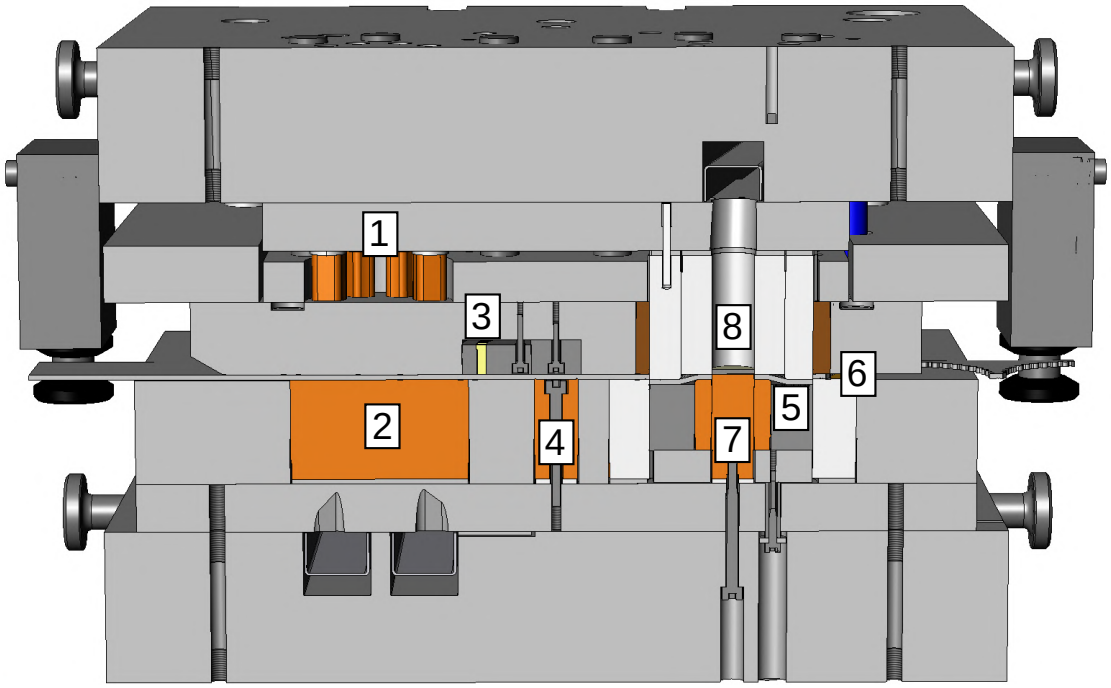

Figure 4.25: Cross section of the closed tool

step. The orange part is the v-ring (4) that was not seen in the illustration before. Prior to the final fineblanking process, the part gets clammed (5) and the offset is generated. Subsequently, the outer gearing is blanked with a punch (6) and counter punch. Simultaneously the inner hole is pierced with a central punch (7) and counter punch (8).

4.4.2 Experimental Design

The following experiment series is a hardening process with varying quenching orientation as seen in figure 4.26. The fineblanked parts are digitalised with the GOM system before quenching. They are either positioned to be laying down (8 parts) or hanging (22 parts) before being through hardened. Thereafter all parts are measured a second time. Because of the complexity of the geometry it was not possible to manufacture water jet cut parts as a reference.
The placement in the quenching cage is shown in figure 4.4. The inscription of the part made it possible to position all hanging parts equally in the same direction to eliminate any effects that may be caused by the minor anisotropy of the material. To prevent the gears from moving during

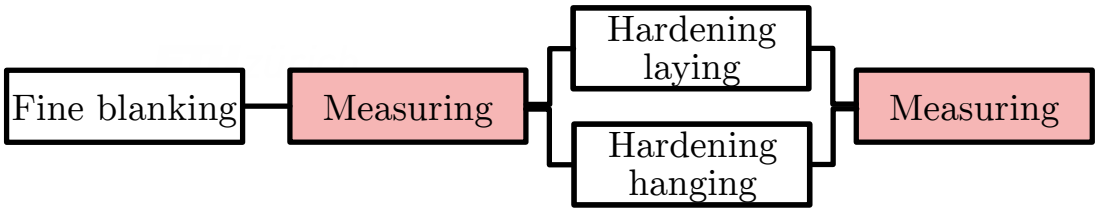

Figure 4.26: Design of experiment for the chain wheel

quenching, wires are used to hold them in place.

4.4.3 Chain Wheel Results and Discussion

Distortion of the chain wheel can best be captured when comparing the measured parts with the target geometry. For better quantification and comparability between parts, a deviation circle similar to the one introduced in section 4.3.3 is used in the following. Other possible methods of distortion descriptions like roundness or flatness were less conclusive and therefore neglected in the scope of this work.
The general procedure to evaluate the experiments was conducted analogically to the fineblanked test specimen series. Firstly, deviations from target geometry before through-hardening are determined. Subsequently, deformations in relation to their quenching position are analysed and recurring distortion modi are identified. Additionally, an experiment where ten specimens are quenched together in block formation in order to control heat transfer is discussed.

Distortion before Heat Treatment

When looking at the parts after fineblanking and before quenching we can notice some typical deviations from target CAD geometry (see figure 4.27). The highest differences can be seen at the gearing where die roll occurs and at the beginning of the bridges which are formed freely without direct contact with the tools. Those regions are deviating up to 0.3 mm to the target geometry. The inner and outer ring however, which are clamped during the forming process, are very close to the CAD data. Furthermore, there is some excess material in the outer pockets.
The GOM system can be very helpful to illustrate or measure deviations from target CAD geometry but an initial alignment of the measured mesh

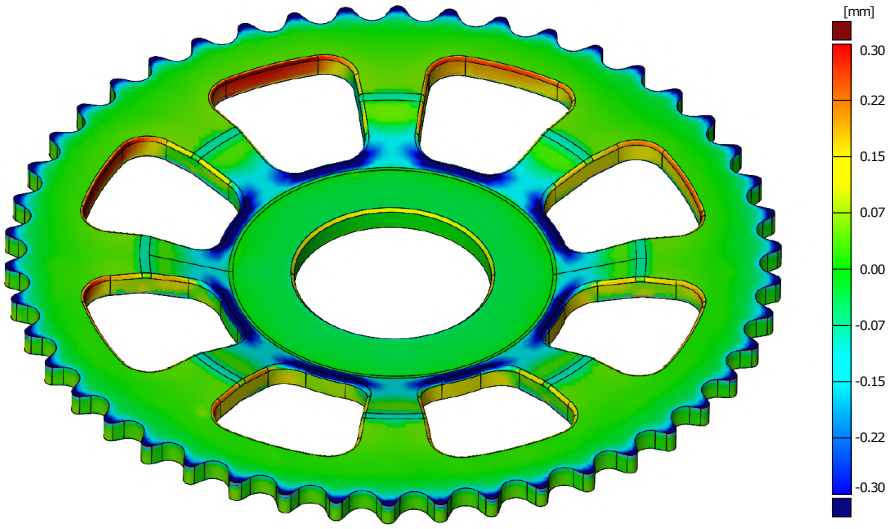

Figure 4.27: 3D blanking part before quenching

is required beforehand. When using a flat part it makes sense to aligned it globally using all available measurement points. For more complex three dimensional geometries a virtual fixation in space can be introduced. When using other measurement methods such as a coordinate measurement system a base is defined from which all further measurement points are related to. The same approach was used to align the optical measurements of the chain wheel by taking the inner ring as a base. The inner ring was chosen as it is the most stable part of the geometry. Also, it is where the part was supported during measurements.
The following graph (figure 4.28) shows deviations from target geometry on a virtual touching ring with radius $r = 46\,\text{mm}$. For all 30 parts the median value, quantiles, minimum and maximum values are plotted. The y-axis was chosen from $-0.1\,\text{mm}$ to $0.3\,\text{mm}$ for better comparison with parts after their heat treatment. Deviations before heat treatment are rather small with an average deviation of $\overline{d}^{CW} = 0.014\,\text{mm}$.

Distortion after Heat Treatment

On first sight, the results of the measurements after heat treatment show high variance and seem random. All parts show strong deviations from the target geometry. The deviations of all 30 parts are shown in figure 4.29.
The average deviation for all parts is with $\overline{D}^{CW} = 0.141\,\text{mm}$ ten times higher than prior to heat treatment $\overline{d}^{CW} = 0.014\,\text{mm}$. The expected ori-

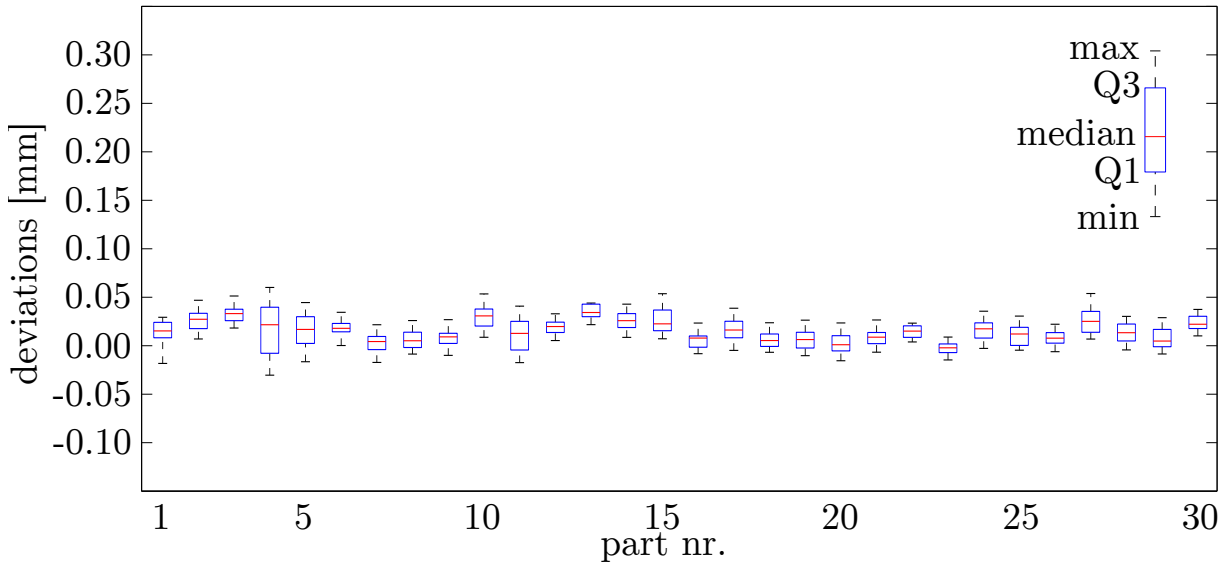

Figure 4.28: Chain wheel deviations before quenching

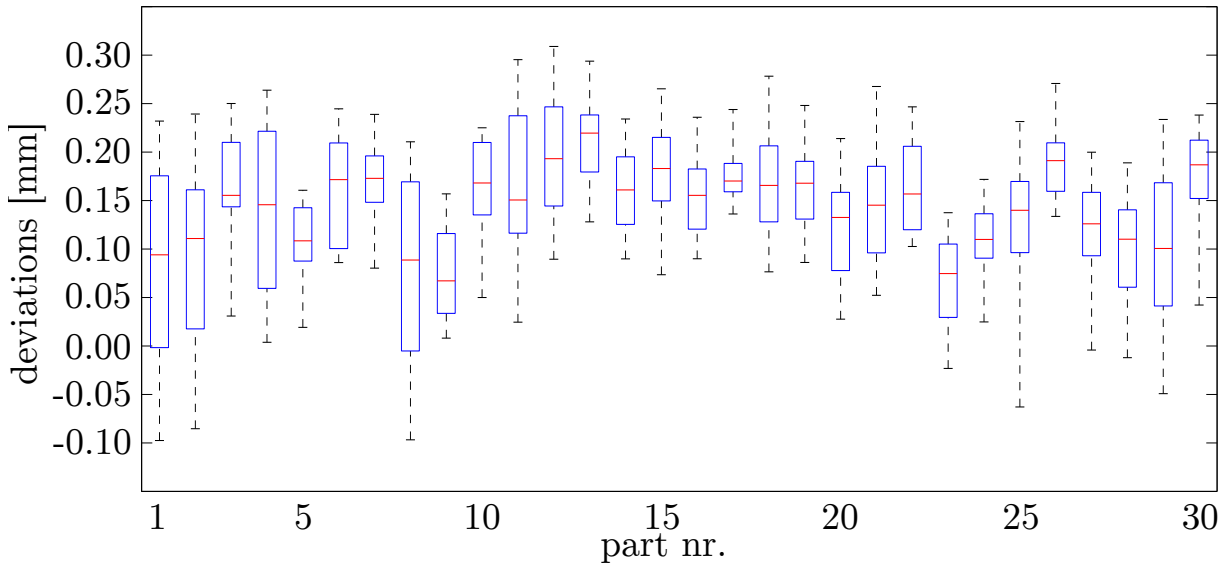

Figure 4.29: Chain wheel deviations after quenching

entation dependency for lying and hanging specimens is not clearly visible. Parts 1-4 and 26-30 are lying during quenching, the others are hanging. The deviations of hanging parts $\overline{D}^{CW}_{hanging} = 0.148\,\text{mm}$ are not distinctly different from lying ones with $\overline{D}^{CW}_{lying} = 0.121\,\text{mm}$.
Two parts are shown exemplary in figure 4.30. Both deviate up to 0.3 mm from CAD data. The blue areas are remainders from the forming stage as previously explained but the red areas are a direct result from hardening.

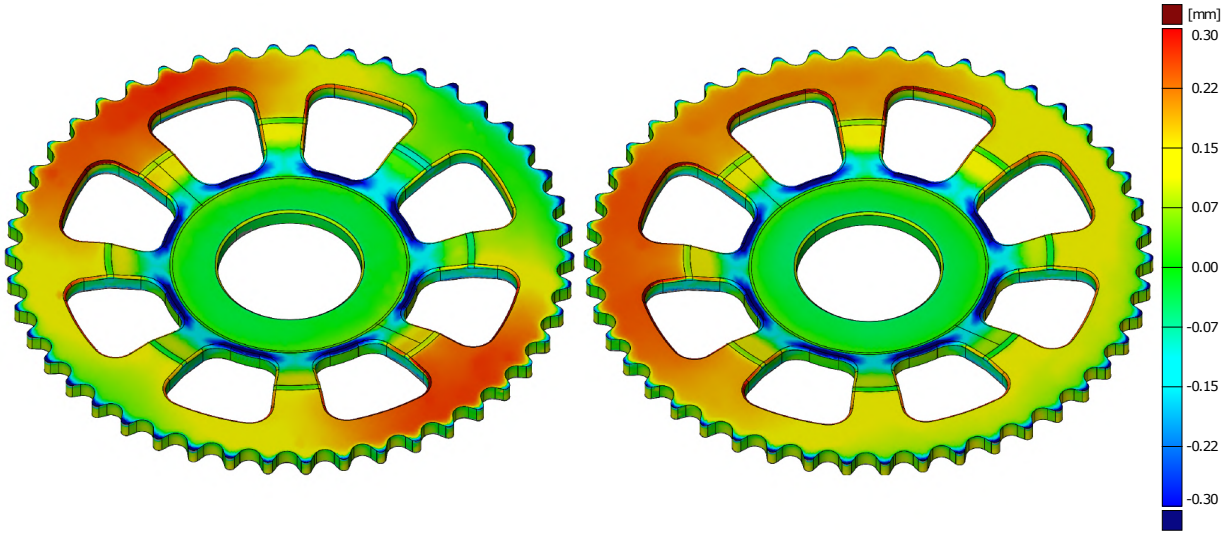

Figure 4.30: Two distinct distortion modi of the chain wheel after heat treatment

The two wheels distinguish themselves significantly from each other, although both show small deviations at the inner ring. As the inner ring stays relatively stable despite high thermal distortion of the part, the choice of the inner ring as the base during measurement evaluations is justified.

When looking clockwise on the outer ring, the one on the left changes from red to green back to red and finally green again. Plotting the measurement points of the wheel on the left along a circle with radius 46 mm results in a double wave as illustrated exemplary by three parts in figure 4.31 (top graph). Whereas the chain wheel on the right in figure 4.30 goes from a red area to green and then back to red again. The part therefore resembles a single wave (bottom graph in figure 4.31). Most of the measured parts fall into one of the two cases but with varying amplitude.

The waviness may be explained by the volume expansion due to martensitic phase transformation in the outer ring. The material expands but is held back by the bridges connecting it to the inner ring and the outer ring starts to buckle. This observation leads to the assumption that the two distortion modi represent a buckling problem and may be detected by buckling analysis. This will be further investigated in chapter 6.

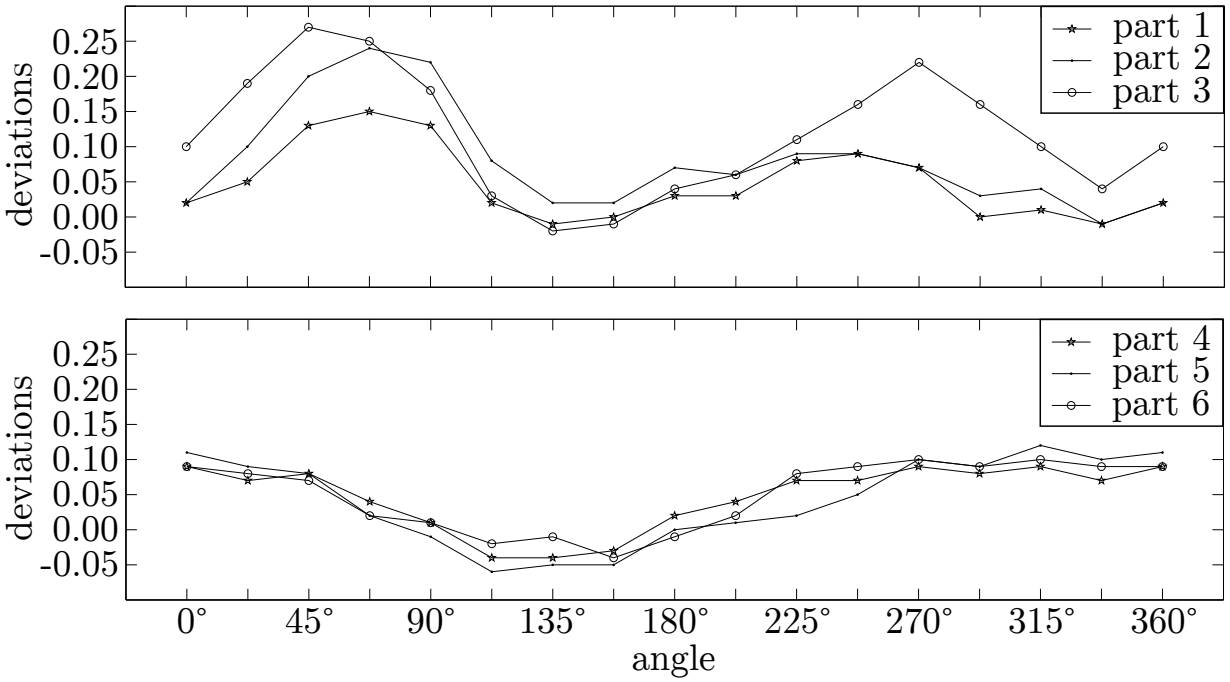

Figure 4.31: Deviations from target geometry along a circle with r=46 mm

Limiting Geometrical Changes During Hardening

It is well known that distortion caused by quenching can be minimised if parts are pressed to stay in a certain geometry. This can be achieved by building tools that constrain the movement and distortion of the part. The so called press quenching is mainly used for geometrical complex components [113, 24]. Additional costs for tools limit the application range and it is only applied as a last resort. Following the same thought of restricting movements, many hardening shops quench their critical parts pressed together.
The subsequently presented experiment is loosely based on this method. Ten gears are quenched together as a 'block' fixed in place with wires. Figure 4.32 show a picture of the parts in block formation after quenching. The movement of each part is limited by the parts bellow and on top of them. This setting also steers the oil flow through the inner and outer holes as well as along the gearing. Therefore the heat flow is also changed compared to single quenching. Only the gearing and the insides of the holes have direct contact with oil, other areas cool down slower than before which may result in different hardening behaviour.
For the evaluation the first two parts on both ends are neglected as they

Figure 4.32: Chain wheels quenched in block formation

are subject to different quenching conditions. The average deviation for the parts in block formation is $\overline{D}^{CW}_{Block} = -0.112\,\text{mm}$ and therefore smaller compared to single quenched parts. The results for different quenching conditions are summarised in figure 4.33. Again, the average values and the standard deviations are plotted.

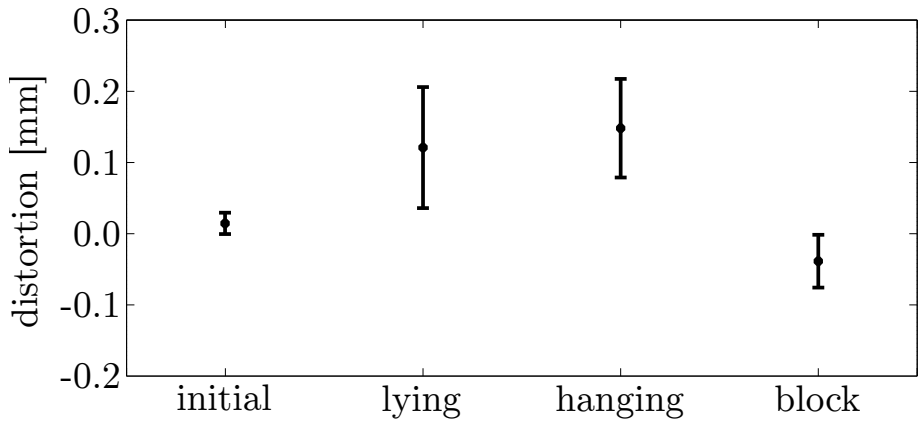

Figure 4.33: Chain wheel influencing factors on thermal distortion

The initial parts only deviate slightly from target geometry. Furthermore, the orientation dependency as seen with the fineblanking test specimen is not clearly identifiable in the case of the chain wheel. Neither lying nor hanging during quenching indicated an improvement of distortion. Both show rather high deviations that can be divided in two major patterns (one or two waves). The quenching in block formation results in smaller

deviations and with an inverted sign.

4.5 Summary of Quenching Experiments

All three parts; bracket, fineblanking test specimen and the chain wheel contributed to the comprehension on how distortion emergences during quenching. In the following the main results are and their consequences for numerical simulations are summarised.

4.5.1 Bracket Bending Experiment

The bracket experiment indicates that residual stress from forming processes influence distortion behaviour during oil quenching. The angular changes caused by spring-back are significantly higher than the ones from quenching. Although annealing the specimens and therefore reducing the residual stresses in the material prior to further heat treatment reduced the angular changes, they are small and may be neglected in numerical models. This will be further investigated in chapter 6. Berens [15] also showed for case hardening that pre-annealing can reduce the spread of changes in geometry and size for rings made of 100Cr6.

4.5.2 Fineblanking Test Specimen

To show the influence of sheet thickness on distortion, the fineblanking test specimen was used in a preliminary work [93]. Generally, it could be shown that the thicker the material, the smaller deviations from target geometry after quenching. This phenomenon can mainly be explained by higher structural stability with increasing thickness. By comparing fine blanked and water jet cut parts, the influence of the cutting process was investigated. The latter specimens can be assumed to be free of residual stresses and have no die roll. Surprisingly no clear difference in terms of distortion after quenching between the two were observed. However, a clear quenching orientation dependency was determined for both fine blanked and water jet cut parts. Specimen that were quenched in an upright, hanging position showed significantly higher distortion than parts that were laying face down.

4.5.3 Chain Wheel

The orientation dependency of the fineblanking test specimen was not reproducible with the chain wheel. No significant difference between parts that were quenched laying face down compared to hanging ones were noticeable. By analysing distortion after quenching two recurring deformation modi (one or two waves) were detected. The modi seem to originate by buckling of the outer ring. This is probably caused by either martensitic volume expansion, non-uniform temperature distribution during quenching or a combination of the two. The cause analysis will be done with the support of FE-simulations in chapter 6. An additional experiment where ten chain wheels were quenched in block formation revealed that this sort of charging can lower distortion after heat treatment by restricting the specimens movement and or controlling the oil flow.
Some effects need a deeper understanding of the complex interactions between phase transformations, temperature and stress evolution. Numerical simulations can be of assistance to trace temperature and stress evolution and their effect on geometrical changes of specimens. After gathering and optimising all necessary material data (chapter 5) FE-simulations are carried out (chapter 6) and compared to the experimental data obtained in this chapter.

5 Material Data for FE-Simulation

Heat treatment simulations must account for the complex interactions between geometry, temperature profile, transformation kinetics, stresses, strains and material. Furthermore, the simulation quality strongly depends on the input data consisting of the material characterisation and boundary conditions. All important material data and their modelling for this thesis are elucidated in this chapter. Many authors demonstrated that close to reality transformation kinetics are key to successfully predicting distortion, residual stresses and hardness after heat treatment processes. After listing all relevant characteristics for numerical simulations, the problems emerging from widely used estimation procedures based on the chemical composition of the used material are pointed out. Further, a newly developed optimisation procedure for the accurate modelling of phase transformation curves based on controlled quenching experiments is introduced. Finally, all relevant material data and models used for numerical simulations in chapter 6 are presented.

5.1 Simulation Relevant Characteristics

A study on changes in size and geometry as a consequence of heat treatment of steel was conducted by Heess et al. [52]. In addition to underlying mode of actions and physical principles, he presents a full list of characteristic parameters relevant for through hardening simulations (see table 5.1). His results are in line with another study conducted specifically on Computer Aided Simulation of Heat treatment (C.A.S.H.) [45]. The material input data can be split in two main fields; firstly the thermal and mechanical characteristics and secondly transformation kinetics that describe phase change. In order to account for transformation induced changes in characteristics during simulations, a multi-phase material model is used. Heat treatment simulations, involving for example carburisation, need additional parameters such as a diffusion coefficient D. The main focus of this thesis lies on through hardening processes, thus the latter are not further discussed.

Table 5.1: Material input data for FE-simulations according to Heess [52]

Thermal and mechanical characteristics		
thermal conductivity	λ	$[\frac{W}{mK}]$
density	ρ	$[\frac{Kg}{m^3}]$
heat capacity	c_p	$[\frac{J}{m^3K}]$
thermal expansion coefficient	α	$[\frac{1}{K}]$
Young's modulus	E	$[\frac{N}{m^2}]$
Poisson's ratio	ν	[-]
yield curve	$\sigma(\varepsilon)$	$[\frac{N}{m^2}]$
Transformation characteristics		
TTT diagram	-	
transformation enthalpy	ΔH	
trans. induced volume change	$\Delta V_{a \rightarrow y_i}$	
trans. plasticity constant	K	

The C.A.S.H study investigates the quality of characteristic values provided by literature, their applicability in the simulation process and the resulting accuracy. The most influencing parameters are listed in table 5.2. Similar results were found in a sensitivity study on critical influencing factors and the quality of thermal distortion prediction after heat treatment [116]. The modelling and implementation of those characteristics is discussed in the subsequent sections.

Table 5.2: Characteristic values strongly influencing simulation results [45]

Characteristic	**Quality of literature**
Transformation plasticity constant	well applicable
Heat transfer coefficient	acceptable
Hardening behaviour $k_f(\varepsilon)$	acceptable
Transformation kinetics/strains	generally not usable

5.2 Transformation Modelling During Heat Treatment

In the following sections models used to describe transformation kinetics as well as their implementation into the finite element simulation are presented. During heating steel above austenitisation temperature, the initial phase composition changes from ferrite/perlite to austenite. In the subsequent quenching, the homogeneous austenite structure transforms, mainly dependent on the cooling rate, into martensite, bainite, ferrite or perlite. The modelling of both heating and quenching behaviour is hereafter discussed.

5.2.1 Austenitisation Modelling

As mentioned in chapter 2.2.2 austenitisation starts when passing A_{C1}-temperature and is completed after reaching A_{C3}-temperature during slow heating. This is true for small heating rates that typically occur in furnace heating. For the assumption of slow heating, a simple thermodynamic equilibrium model can be used to model austenitisation [114]:

$$y_a = \frac{T - A_{C1}}{A_{C3} - A_{C1}} \quad for\ T > A_{C1} \tag{5.1}$$

Where y_a is the austenite volume fraction, A_{C1} and A_{C3} for austenite start and end temperature. Transformation begins when A_{C1} is reached. As soon as the temperature reaches A_{C3} the austenite phase fraction y_a equals 1 hence the material is fully austenitised. Faster heating rates are present in the cases of laser heating or welding and require models that take dynamic effects into account. These are not further discussed at this point.

The grain size of austenite is assumed to stay constant during the relatively short holding time before quenching. A study investigated the influence of alloying elements, holding time and austenitisation temperature on grain growth [77]. Temperatures highly above A_{C3} and long holding times are necessary to significantly change the grain size. The assumption of constant grain size therefore is reasonable for through hardening processes.

5.2.2 Phase Transformation Modelling During Quenching

During quenching of austenitised steels new phases are formed through diffusion controlled or diffusionless transformation. The modelling and implementation of the two transformation types are presented in the following.

Diffusion Controlled Transformation

Two of the most important methods describing diffusion controlled phase transformations during quenching are subsequently presented. Both are based on the generalised Kolmogorov-Johnson-Mehl-Avrami (JMAK) equation [6, 7, 8, 62, 69], where the volume fraction y_i for a certain phase is expressed as:

$$y_i = y_i^{eq}(1 - \exp[-b_i t^{n_i}]) \tag{5.2}$$

t represents time, b and n are temperature dependent material parameter and y_i^{eq} is the momentary thermo-dynamical equilibrium fraction that can be determined with the equilibrium phase diagram [76].
The first type of models are based on isothermal transformation diagrams, which are used to calculate the b and n parameters for each time step:

$$\begin{aligned} n_i(T) &= \frac{\ln[\ln(1-0.1/y_i^{eq})/\ln(1-0.9/y_i^{eq}]}{\ln\left[(t_i^{10\%}-t_i^{start})/(t_i^{90\%}-t_i^{start})\right]} \\ b_i(T) &= \frac{-\ln(1-0.9/y_i^{eq})}{(t_i^{90\%}-t_i^{start})^n} \end{aligned} \tag{5.3}$$

$t_i^{90\%}$ and $t_i^{10\%}$ are taken directly from the corresponding time temperature transformation (TTT) diagram. TTT diagrams contain isothermal transformation data and are presented in section 5.2.2. Note that all parameters in the equation are themselves dependent on the current temperature. The advantage of this type of models is their applicability for arbitrary temperature paths and their generally good transformation prediction capabilities [9]. The second kind of approach is based on the works of Leblond and Devaux [74] and represent a simplified version of equation 5.2, the so called Leblond-equation:

$$\dot{y}_i = \frac{{y_i}^{eq} - y_i}{\tau} \tag{5.4}$$

Nucleation and growth of new phases are combined within a single formula and the temperature-dependent parameter τ is of phenomenological nature and has to be adapted to fit experimental data. Although there exist many extensions to equation 5.4 that account for additional phenomena, such as quenching rate, only cooling paths that are close to the experimental data, that was used for fitting, may be predicted in a satisfying matter [67, 81, 2, 83]. In most cases however, TTT based models are superior in predicting correct transformation behaviour [9]. This is why a TTT-based approach was chosen in the scope of this work.

Diffusionless Martensite Transformation

The diffusionless martensitic transformation is not directly time dependent. The phase growth relies mainly on temperature (which is time dependent) and was established by Koistinen and Marburger [68]:

$$y_m = y_a[1 - exp(-c_m(M_s - T))] \tag{5.5}$$

with $c_m = 1.1 * 10^{-2}$, y_m as the martensite and y_a as the remaining austenite volume fraction. M_s represents the martensite start temperature and is material dependent. This means that austenite, which is not transformed to ferrite, perlite or bainite before reaching M_s begins to turn directly into martensite.

TTT Diagrams and the Additivity Principle

The basis for phase transformation kinetics in this work is isothermal material data represented by TTT diagrams. They can be either measured or estimated and contain time-temperature curves that feature start, intermediate and end points of isothermal transformations. Typically, intermediate data points indicate how much time has to pass in order to have 10% respectively 90% of the transformation completed for a given temperature. A schematic visualisation of such a diagram can be seen in figure 5.1.
This specific TTT diagram shows only start and end points and can be split in characteristic regions [114]:

- $A_3 - A_1$: ferrite proeutectoid
- $A_1 - TH$: ferrite and perlite

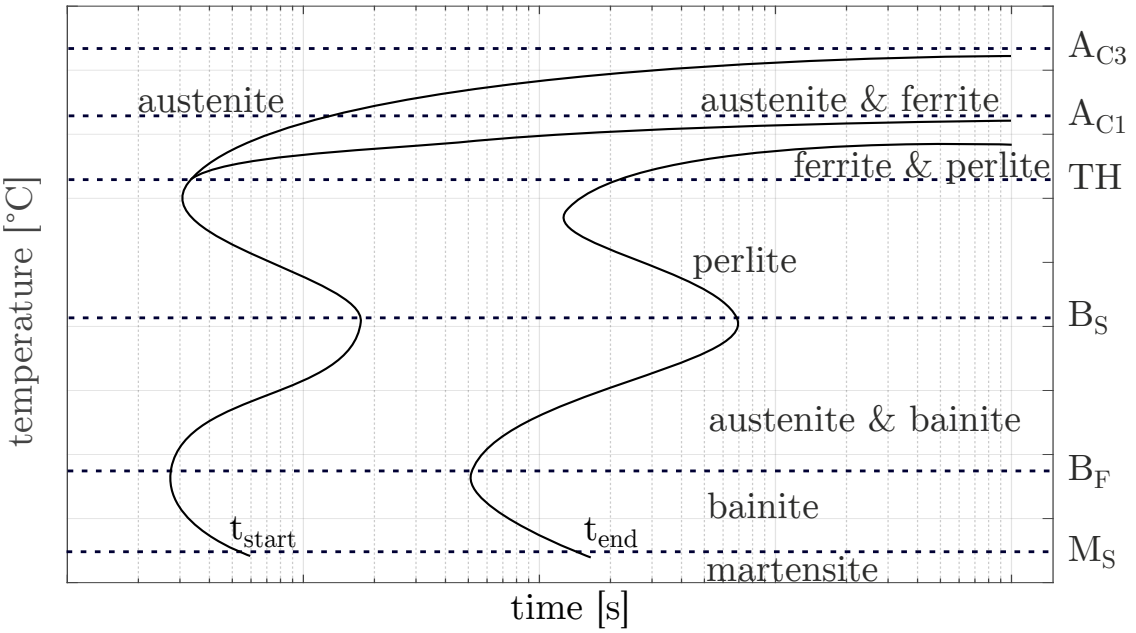

Figure 5.1: Schematic TTT diagram with transformation-start and -end curves [114]

- $TH - Bs$: only perlite
- $Bs - Bf$: incomplete bainite
- $Bf - Ms$: bainite
- $Ms-$: martensite

The regions show into which phases austenite is transformed when staying on a constant temperature. In order to represent non-isothermal quenching paths with isothermal data, the so-called additivity principle is used, which was introduced by Pumphrey and Jones [100]. The continuous time-dependent temperature function is divided in n isothermal steps.

In figure 5.2 the additivity principle is visualised by a step function representing a series of isothermal stages.

Before austenite is transformed into other phases, a certain amount of time passes which is called nucleation or incubation time. In order to account for this behaviour the approach distinguishes nucleation and growth. This delay is implemented with the Sheil method where the incubation time t_{inc}

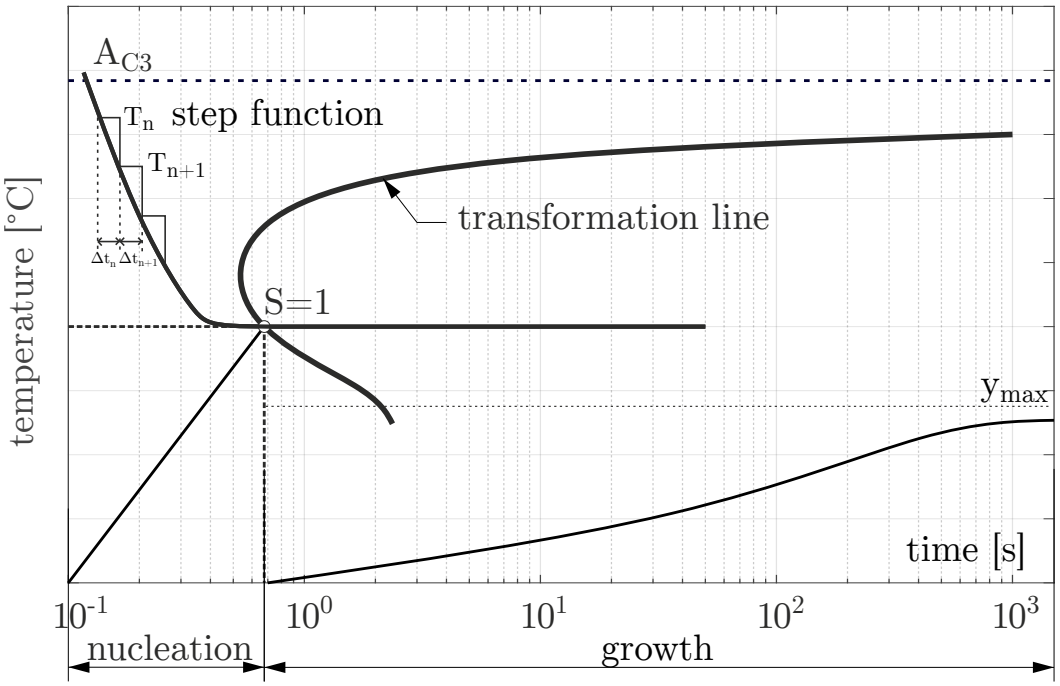

Figure 5.2: Visualisation of nucleation and phase growth

is determined by computing the Sheil parameter S [104]:

$$S = \int_0^{t_{inc}} \frac{dt}{t_{start}(T)} \tag{5.6}$$

t_{inc} corresponds to the transformation start time t_{start} at a certain temperature T. By applying the additivity principle we can write the Sheil's summation at the end of the increment n as following [114, 104]:

$$S_n = \sum_{i=1}^{n} \frac{\Delta t_i}{t_{start}(T_i)} \tag{5.7}$$

As soon as the Sheil condition is reached ($S_n \geq 1$), the incubation time is complete and a new phase initiates to grow. This subsequent growth stage can either be a diffusion controlled or diffusionless transformation (see chapter 2.2.2). Dependent on the their type a suitable approach is used as explained in the section 5.2.2.

5.2.3 Estimation of a TTT Diagram Based on Chemical Composition

For calculating diffusion controlled phase transformations with the presented method, a TTT diagram is required. It can be rather difficult to measure those isothermal transformation diagrams due to the small incubation time for most steels. In order to measure isothermal transformation, the descent-time to reach the desired temperature has to be negligible compared to the incubation time for that temperature [114]. The general measurement procedure is more deeply described in the standard [117, 118]. Alternatively, an estimated TTT diagram can be used. In this section a TTT diagram is approximated with the chemical composition and grain size of C60E steel with the help of a tool provided by the FE-software FORGE. The estimation method is widely used when measured isothermal data are not available. The obtained transformation curves are then used in a finite element simulation to predict final hardness and phase structure of elements with arbitrary quenching paths.
Unfortunately, as later shown, this approach predicts the measured results of continuous cooling experiments insufficiently as they show significant deviations from the measured CCT data (see section 5.2.4). This is why a two step optimisation method was developed in order to enhance accuracy of final phase content and hardness prediction after quenching simulations (see section 5.3).

Estimation of Characteristic Temperatures

The grain size of 7.5 µm was determined with polished micrographs of the untreated material. Together with the chemical composition (see table 3.1) a TTT diagram is calculated in the following by using the FORGE TTT-Generator. Firstly, A_{C1} and A_{C3} temperatures are estimated using empirical formulas by Andrews [5] and Kasatkin [64]. All chemical elements are in mass-%:

$$A_{C1} = 723 - 10.7Mn - 16.9Ni + 29.1Si + 16.9Cr + 6.38W + 290As \quad (5.8)$$

And for A_{C3} the mean value of the Andrews and Kasatkin estimation was

used. With A^A_{C3}:

$$A^A_{C3} = 910 - 203\sqrt{C} - 15.2Ni + 44.7Si + 104V + 31.5Mo + 13.1W \\ - 30Mn - 11Cr - 20Cu + 700P + 400Al + 120As + 400Ti \tag{5.9}$$

and A^K_{C3}:

$$A^K_{C3} = 912 - 370C - 27.4Mn + 27.3Si - 6.35Cr - 37.2Ni + 95.1V \\ + 190Ti + 72Al + 64.5Nb + 5.57W + 332S + 276P + 485N \\ - 900B + 16.2CMn + 32.3C \cdot Si + 15.4C \cdot Cr + 48C \cdot Ni \\ + 4.32Si \cdot Cr - 17.3Si \cdot Mo - 18.6Si \cdot Ni + 4.8Mn \cdot Ni \\ + 40.5Mo \cdot V + 174C^2 + 2.46Mn^2 - 6.86Si^2 + 0.322Cr^2 \\ + 9.9Mo^2 + 1.24Ni^2 - 60.2V^2 \tag{5.10}$$

averaged to $\bar{A}_{C3}$:

$$\bar{A}_{C3} = 0.5(A^A_{C3} + A^K_{C3}) \tag{5.11}$$

The bainite-start temperature B_S is calculated using the Kirkaldy-model [67]:

$$B_S = 656 - 57.7C - 35Mn - 75Si - 15.3Ni - 34Cr - 41.2Mo \tag{5.12}$$

The martensite start temperature M_S can be approximated with several approaches [61, 124, 21, 120, 5], one, also based on the chemical composition, was formulated by Haynes [111]:

$$M^H_S = 656 - 57.7C - 35Mn - 75Si - 15.3Ni - 34Cr - 41.2Mo \tag{5.13}$$

Another one by Andrews [5]:

$$- M^A_S = 512 - 452.8C - 16.92Ni + 14.97Cr - 9.5Mo - 71.44Mn \cdot C \\ - 6.62Cr \cdot C + 216.9C^2 \tag{5.14}$$

Again, an average of the two is taken:

$$\bar{M_S} = 0.5(M_S^H + M_S^A) \tag{5.15}$$

All characteristic temperatures are now estimated.

Estimation of Transformation Kinetics

In the next step transformation curves are calculated with the Kirkaldy-method, which is briefly explained in the following [67]. The method is based on the assumption that diffusive transformation kinetics can be approximated with a total function F consisting of sub-functions f_i. Every sub-function depends on one of four main parameters: grain size G (ASTM value), chemical composition, current temperature T, and phase fraction y_i. The transformation kinetics can therefore be written as:

$$\frac{dy_i}{dt} = F(f_1, f_2, f_3, f_4) \tag{5.16}$$

with

$$\begin{aligned} f_1(G) &= 2^{(G-1)/2} \\ f_2(C, Mn, Ni, Cr, Mo) & \\ f_3(T) &= \Delta T^n D \\ f_4(y_i) &= \frac{y_i^{\frac{2(1-y_i)}{3}}(1-y_i)^{\frac{2y_i}{3}}}{X} \end{aligned} \tag{5.17}$$

ΔT is the temperature difference to the corresponding transformation start temperature in equilibrium. n and D are dependent on the diffusion mechanism type, X is a delayed reaction factor that takes stabilisation effects during austenite to bainite transformation into account. All three parameters n, D, X and f_2 have to be identified empirically or can be estimated. In order to obtain the necessary time τ_i that a certain phase fraction y_i needs to transform from austenite, equation 5.16 together with 5.17 has to be inverted:

$$\tau_i(y_i, T) = \int_0^{y_i} \frac{dx}{F} \tag{5.18}$$

The empirical formulations for each phase can be found in [114]. The method described finally leads to the calculated time temperature transformation curves illustrated in figure 5.3.

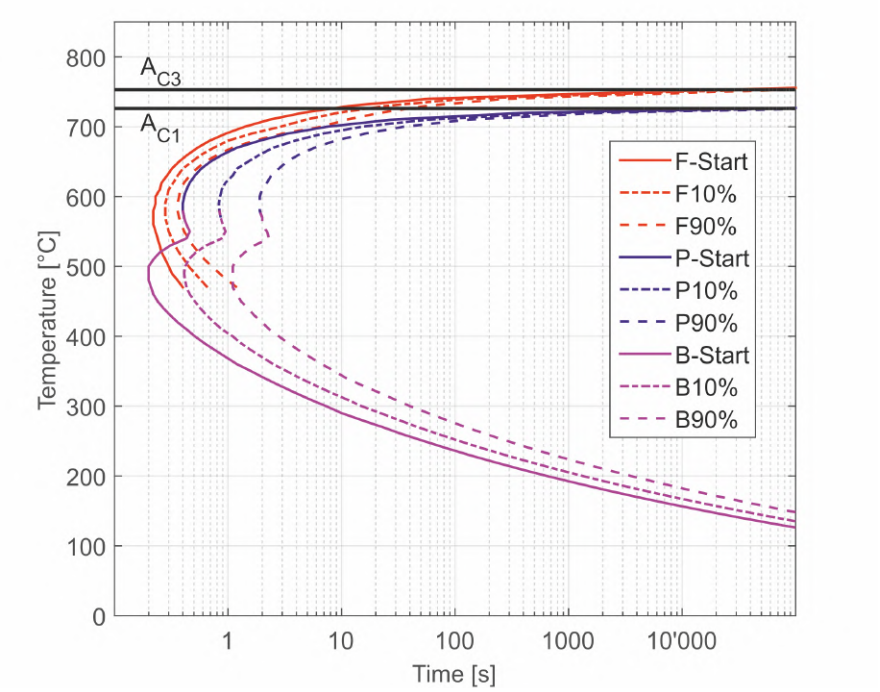

Figure 5.3: TTT diagram estimation with the chemical composition

The full line represents the isothermal transformation starting line, the first dotted from left indicates 10% transformation of the maximal $y_{i,max}$ that is possible at that temperature. The second dotted line shows where 90% of phase transformation is completed. The diagram thus gives us the information of how much of a phase is transformed isothermally after a certain amount of time. For instance, after 15 s 10% bainite (of the maximum possible amount of bainite $y_{B,max}$) would have transformed from austenite at a constant temperature of 300 °C.

Hardness Prediction

The hardness is either directly linked to the current or final phase composition of the material through a simple mixing rule or incrementally where H also accounts for the momentary transformation temperature. The more

simple mixing rule can be expressed as follows:

$$H = \sum_i y_i H_i(T) \tag{5.19}$$

H is the hardness for each finite element and depends on all occurring phases according to their fraction y_i multiplied with the corresponding phase hardness H_i.
Alternatively one can account for the effect, that hardness of certain phases are dependent on the transformation temperature. For example bainite that transforms from austenite at lower temperature has a greater hardness than one that evolved at higher temperatures [98]. Figure 5.4 shows the incremental hardness dependent on transformation temperature that is used in FORGE by default.

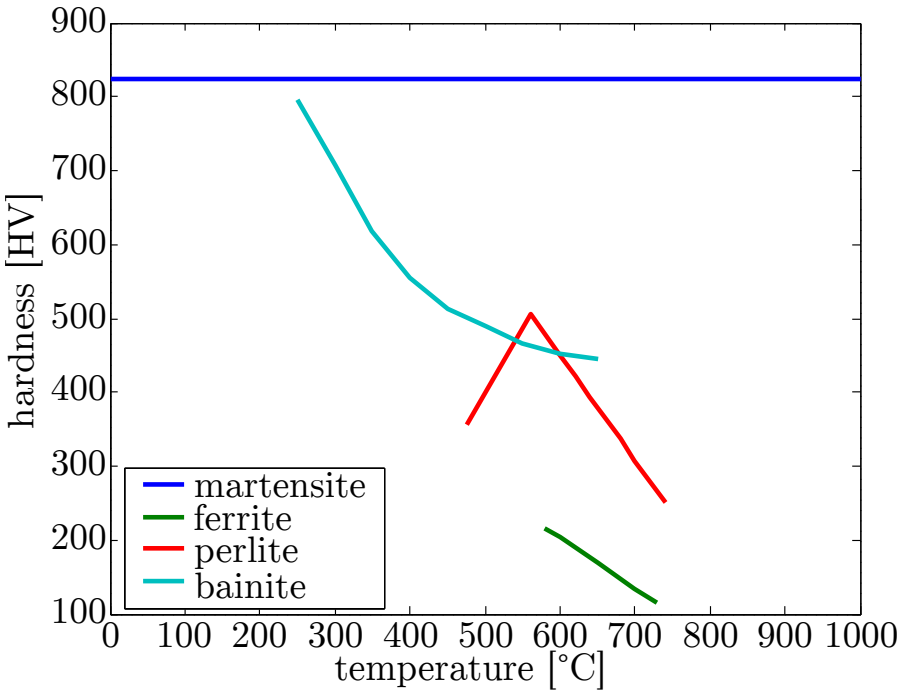

Figure 5.4: Incremental hardness for different transformation temperatures in FORGE

As previously mentioned, bainite depends on its transformation temperature due to the mostly blocked diffusion of iron atoms at lower temperatures and the inhibited diffusion of the much smaller carbon atoms. This leads to two different transformation mechanisms for bainite; upper bainite that is similar to perlite transformation with inhibited carbon diffusion and lower

bainite by diffusionless transformation similar to martensite transformation [71], [98]. The martensite hardness can reach from 200 HV to 1100 HV but is presumed to be independent of its transformation temperature and solely dependent on carbon content [101]. The total hardness is summed over all calculation steps k combined with a mixing rule for all present phases i:

$$H = \sum_{k} \left(\sum_{i} y_i H_i(T) \right) \tag{5.20}$$

5.2.4 Inaccuracies with the Estimated TTT Diagram

In order to check the plausibility of the TTT diagram that was estimated with the Kirkaldy method a validation attempt is conducted. The controlled quenching experiments of section 3.2.1 are used to validate the quality of the estimation. Nine different quenching times are analysed; 10 to 1000 seconds from A_{C3} to 200 °C as seen in figure 3.4. Analogously to the experiments on the dilatometer, cylindrical specimens are simulatively heated to 850 °C in order do get 100% austenite (on the basis of equation 5.1). A directly followed quenching simulation is conducted. The temperature paths, respectively the cooling rates are identical to the ones in the experiments. After all simulations are completed, phase structure and hardness is compared. The hardness values of the simulation and the experiment are shown in figure 5.5.
Every point in time on the x-axis represents a single quenching experiment. The differences between measurements and simulation are substantial: hardness is underestimated for fast quenching times of 10 to 20 seconds and overestimated for slower cooling rates from 40 to 1000 seconds. The 10 second quenching experiment can be used to demonstrates the need for optimised transformation curves. The hardness should not only be more than 200 HV higher, the simulation is not capable of predicting correct martensitic phase transformation with the underlying estimated transformation curves. The micrograph in figure 3.5 shows 95-100% martensite after quenching whereas the simulation estimates 0%. But even if the phase transformation prediction would be successful, hardness of martensite is overestimated in FORGE (see figure 5.5) with 800 HV. In the next section a newly developed optimisation algorithm, based on controlled quenching experiments, aims to optimise the prediction accuracy.

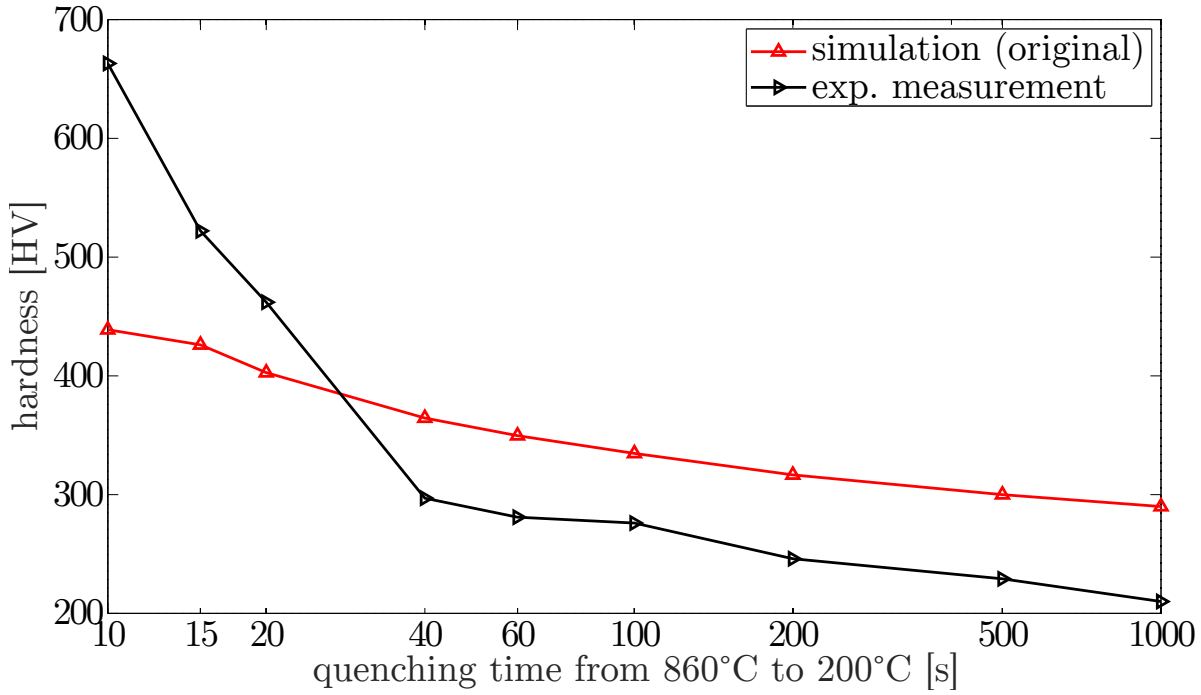

Figure 5.5: Measured versus simulated hardness values

5.3 Optimisation of Material Data

In the following, the thermal material data conceived in the previous section is optimised in two steps in order to have more accurate phase transformation and hardness prediction in quenching simulations. By using the controlled quenching experiments measured in section 3.2.1, transformation curves are adapted fit the hardness and phase structure measurements. The presented method was developed by the author and was published in 2016 [95]. The general two step optimisation procedure is schematically illustrated in figure 5.6.

After obtaining constant hardness values h_{opt} for each individual phase based on the measured CCT diagram in step 1, all quenching experiments from 10-1000 seconds quenching time ($T_{10}-T_{1000}$) are simulated as described in section 5.2.4. The resulting final hardness and phase fractions of each simulation are evaluated with measured data. If no convergence is reached with the initial simulation, transformation curves are adjusted according to certain rules that are further explained in section 5.3.2. Simulations of all quenching times $T_{10} - T_{1000}$ are repeated with the updated transformation behaviour and compared with measured data. If the hardness and phase

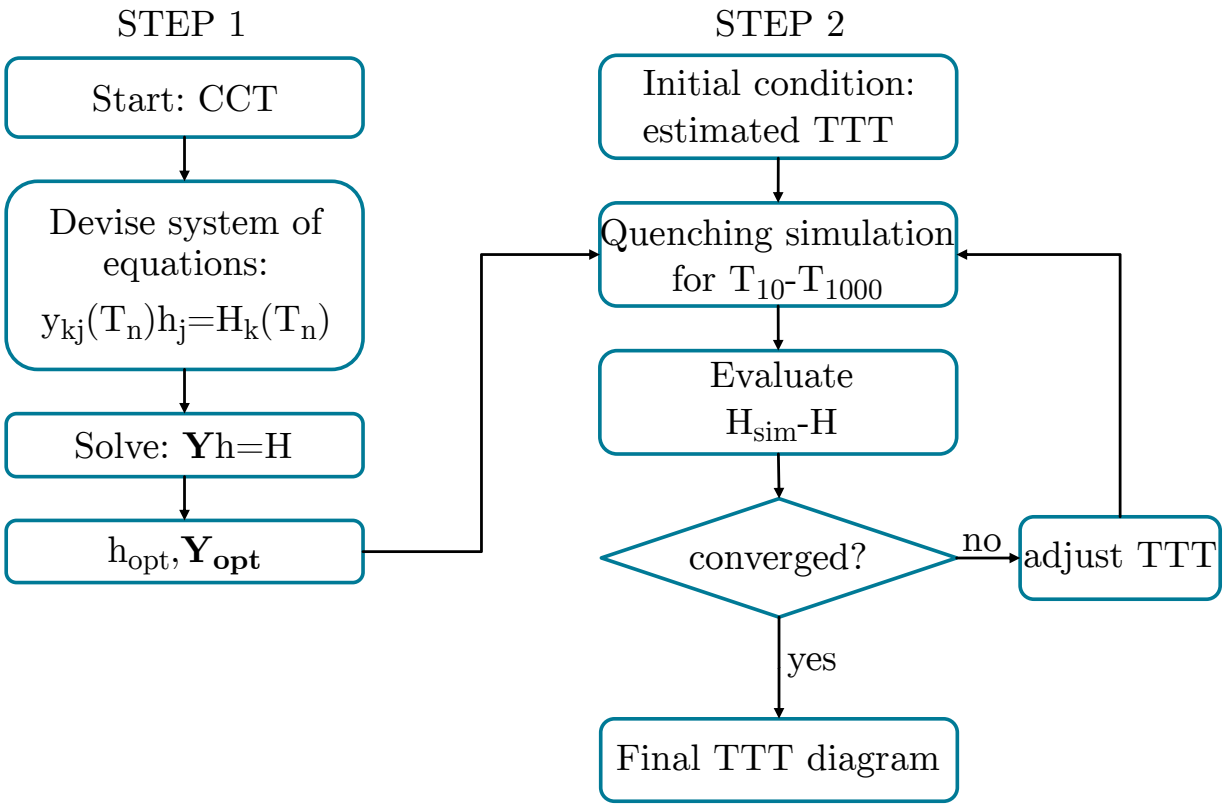

Figure 5.6: Optimisation process of hardness values (step 1) and transformation curves (step 2)

composition is predicted in a satisfying manner, the TTT diagram can be used for general quenching simulations. Otherwise transformation curves are further modified until a convergence is reached.

5.3.1 Optimisation Step 1 - Hardness Values

The first step aims to optimise the individual hardness values of each phase. This method neglects transformation-temperature dependent effects and only accounts for the current phase composition in the material to predict its hardness H as presented in 5.2.3. The mixing rule multiplies the phase fractions y_k with the hardness values y_j of each phase (perlite, ferrite, bainite and martensite):

$$y_F h_F + y_P h_P + y_B h_B + y_M h_M = H_i \tag{5.21}$$

It is assumed, that all phase fractions for a given material equal to 1. This

means that austenite is completely transformed to one of the four previously mentioned phases:

$$y_F + y_P + y_B + y_M = 1 \tag{5.22}$$

The measured CCT diagram of section 3.2.1 contains final hardness values for each quenching experiment. The corresponding phase fractions are determined with polished micrographs and listed in table 5.3. The determination of the exact phase structure is challenging. When using the etching method, light-dark contrast makes not only phase components visible, but also additional metallic properties, such as grain boundaries and non-metallic inclusions. As the fraction measurements are afflicted with uncertainties, a range of possible phase percentages is given.

Table 5.3: Measured phase fractions and hardness values

quenching time	ferrite	perlite	bainite	martensite	hardness
10 seconds	0%	0%	5-15%	85-95%	663 HV
15 seconds	0-5%	0%	60-90%	10-40%	522 HV
20 seconds	0-15%	0-20%	60-80%	0-10%	462 HV
40 seconds	20-40%	60-80%	0%	0%	297 HV
60 seconds	20-40%	60-80%	0%	0%	281 HV
100 seconds	20-40%	60-80%	0%	0%	276 HV
200 seconds	30-50%	50-70%	0%	0%	246 HV
500 seconds	40-60%	40-60%	0%	0%	229 HV
1000 seconds	40-60%	40-60%	0%	0%	210 HV

The hardness and phase fraction information is used to build a linear equation system, where $\mathbf{Y}$ is a matrix containing phase fractions y_n, h the phase related hardness and H the total hardness.

$$\mathbf{Y}h = H \tag{5.23}$$

$\mathbf{Y}$ and H are known from the measurements and h is unknown. To show how to set up the equations, the first experiment with a quenching time of ten seconds is taken as an example. It is known, that only bainite and

martensite are present and the final hardness is 663 HV. According to equation 5.21, it can be expressed with:

$$0h_F + 0h_P + y_B h_B + y_M h_M = 663 \tag{5.24}$$

The data of all nine experiments can therefore be written as:

$$\begin{bmatrix} 0 & 0 & y_{1,3} & y_{1,4} \\ y_{2,1} & 0 & y_{2,3} & y_{2,4} \\ y_{3,1} & y_{3,2} & y_{3,4} & y_{3,4} \\ y_{4,1} & y_{4,2} & 0 & 0 \\ y_{5,1} & y_{5,2} & 0 & 0 \\ y_{6,1} & y_{6,2} & 0 & 0 \\ y_{7,1} & y_{7,2} & 0 & 0 \\ y_{8,1} & y_{8,2} & 0 & 0 \\ y_{9,1} & y_{9,2} & 0 & 0 \end{bmatrix} * \begin{bmatrix} h_F \\ h_P \\ h_B \\ h_M \end{bmatrix} = \begin{bmatrix} 663 \\ 522 \\ 462 \\ 297 \\ 281 \\ 276 \\ 246 \\ 229 \\ 210 \end{bmatrix} \tag{5.25}$$

A zero is set wherever the occurring of a certain phase can be ruled out. The assumption of equation 5.22, which states that the sum of all fractions equals to one, is taken into account. The number of phase fractions can therefore be reduced from 21 to twelve. With nine equations, twelve unknown phase fractions and four hardness values (totally sixteen unknowns), the equation system is undetermined. Therefore the problem is further restricted by the upper and lower bound for phase fractions presented in table 5.3. By solving the system in Matlab with the constrained optimisation functionality fmincon, the individual hardness values h (table 5.4) and corresponding phase fractions $\mathbf{Y}$ (table 5.5) are obtained. As expected, only four hardness values and three of the phase fractions have been actively optimised leading to a fully determined system. All other unknowns have simply been set to their boundary values. The first step is therewith completed.

Table 5.4: Optimised hardness values

phase	hardness [HV]
ferrite	137
perlite	322
bainite	517
martensite	654

Table 5.5: Optimised phase fractions

quenching time	ferrite	perlite	bainite	martensite
10 seconds	0%	0%	5%	95%
15 seconds	5%	0%	50%	45%
20 seconds	15%	19%	60%	6 %
40 seconds	20%	80%	0%	0%
60 seconds	20%	80%	0%	0%
100 seconds	20%	80%	0%	0%
200 seconds	37%	63%	0%	0%
500 seconds	52%	48%	0%	0%
1000 seconds	60%	40%	0%	0%

5.3.2 Optimisation Step 2 - Transformation Curves

The second step optimises transformation curves in order to predict the final phase composition accurately. The TTT diagram estimated with the chemical composition and grain size of the material (see section 5.2.3) is used as the initial starting point for the optimisation procedure. A local modification strategy is applied, where transformation curves are translated and stretched. Some general relationships can be observed (see figure 5.7): By increasing the grain size, transformation curves are shifted to the right on the time axis. This leads to an increase in hardness for faster quenching rates by delaying the diffusion controlled transformations, thus increasing martensite development. Conversely, hardness decreases when transformation curves are shifted to the left. Lifting the ferrite or perlite curves locally results in decreased hardness values in the quenching simulations. Whereas

modifications of ferrite lines affect faster quenching (15 s - 20 s) and perlite lines influence moderate quenching times (40 s - 100 s). Elevating bainite transformation lines leads to an increase in hardness for simulations with 10 s - 60 s quenching time and vice versa.

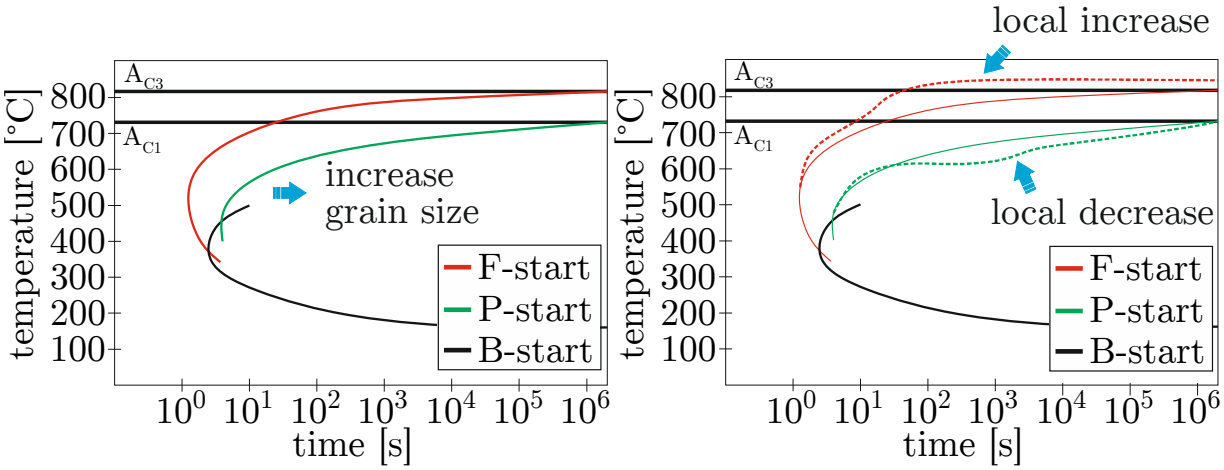

Figure 5.7: Visual representation of the modification strategy

By following these rules and including the measured A_{C1} and A_{C3} temperatures, the initial transformation curves can be optimised (see figure 5.8). All transformation curves are shifted to the right in order to capture the almost full martensite transformation for fast quenching (10 s). The bainite and ferrite curves are locally lifted to account for lower hardness at moderate and higher hardness for faster quenching rates. The perlite curves are not changed.

In combination with the hardness optimisation of step 1 not only phase structure but also hardness prediction is improved. Figure 5.9 shows the experimental data, the original and optimised hardness values for all nine quenching experiments. The simulation is now able to accurately predict martensite transformation for fast quenching, which is most important for more complex quenching simulations. The optimised transformation curves enable the prediction of perlite/ferrite transformations for slow cooling rates as well. Whereas moderate quenching rates do not show significant improvement. The optimised material data used for all further quenching simulations are listed in the appendix 8.2.

In order to validate the optimised transformation behaviour, the modified Jominy experiment of section 3.3 is revisited in the following.

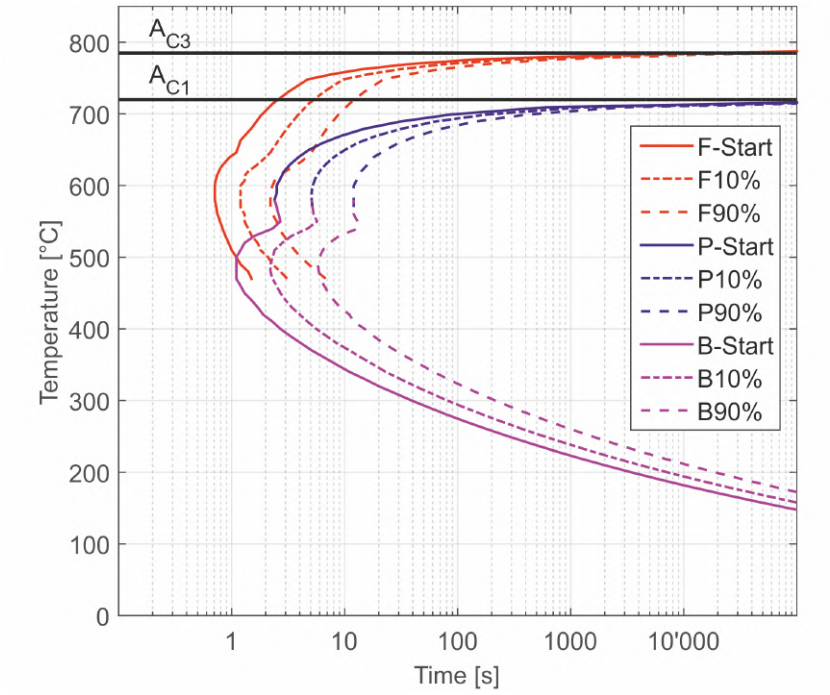

Figure 5.8: Optimised TTT diagram

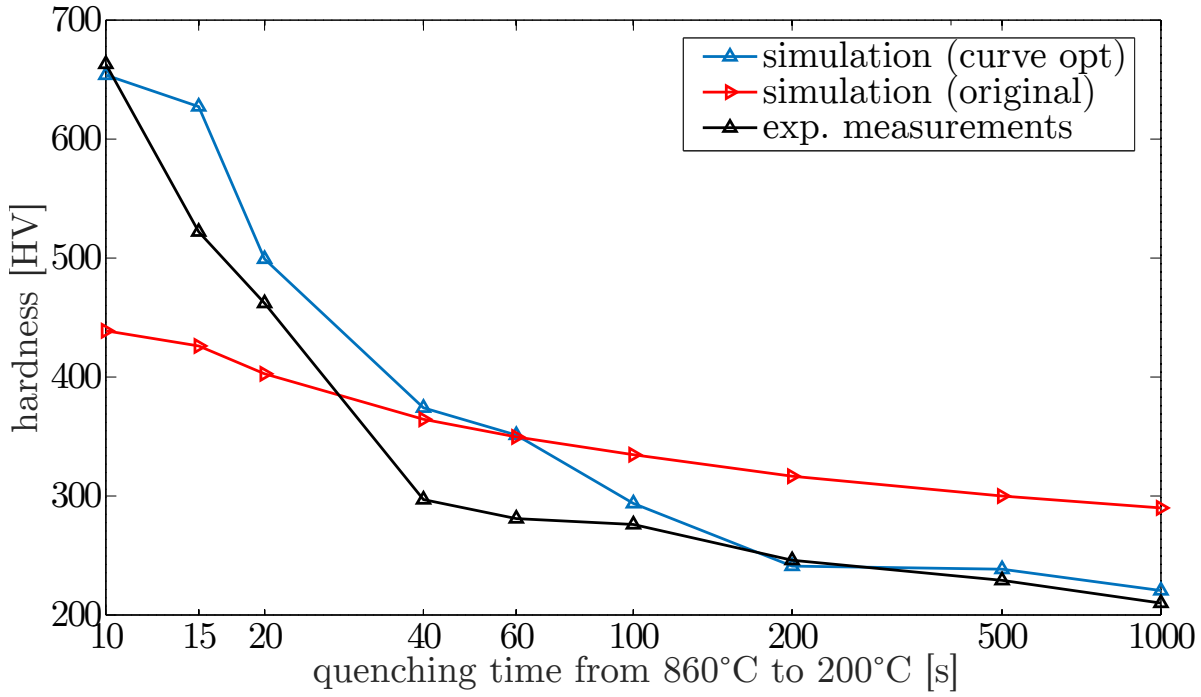

Figure 5.9: Measured versus simulated hardness values after optimisation

5.3.3 Validation with the Modified Jominy Experiment

Comparing resulting hardness distribution and phase structure from the finite element simulation of the Jominy experiment with the measured values (see section 3.3) is useful to validate the material model [81, 72, 92]. Correct boundary conditions are key in order to get comparable temperature evolution for the whole Jominy specimen. The used heat transfer coefficient, taken from the Forge database, is applied only for the first three millimetres of the specimen. The surface-temperature dependent transfer coefficient is illustrated in figure 5.10.

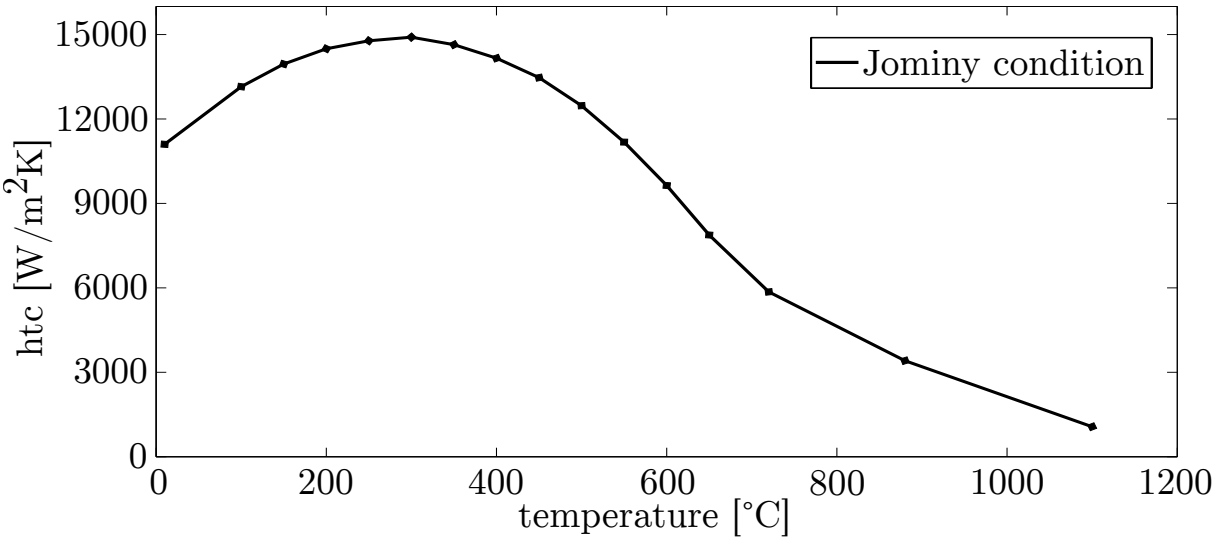

Figure 5.10: Heat transfer coefficient for the first 3 mm

The remaining surfaces are assumed to have a constant heat transfer with air, which is set to 20 W/m^2K. The ambient temperature is at constant 20 °C and emissivity was previously measured and kept at 0.76. The resulting hardness distribution from the quenching face in comparison to the measured values are shown in figure 5.11.
Fast quenching and therewith resulting hardness is close to experimental data. For through hardening processes this is the most important region. The simulation predicts a drop of hardness after seven millimetres, which is too early. Deviations may be caused by an insufficient description of bainite and ferrite evolution in this region. After circa 13 mm, when mainly ferrite/perlite is present, there is a good agreement with measurements.

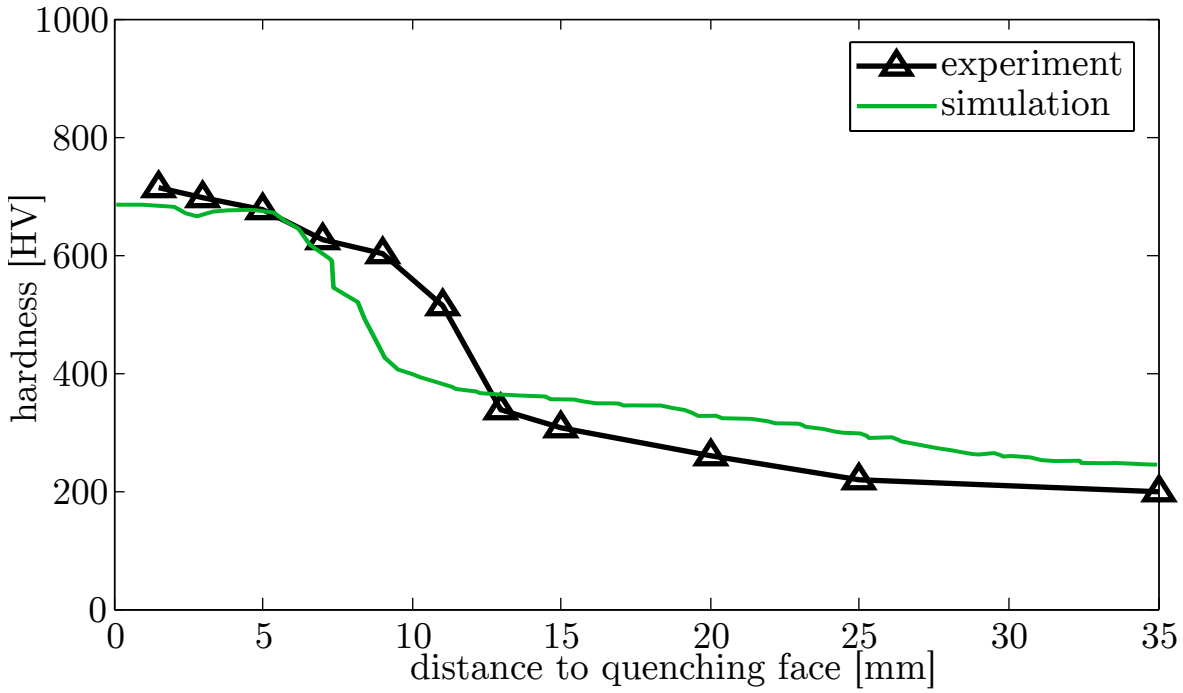

Figure 5.11: Jominy hardness validation

5.4 Discussion

By conducting the presented two step optimisation procedure hardness and phase content prediction was improved significantly. The results are especially accurate for fast quenching rates, which is most important for through hardening applications. Intermediate quenching rates that encounter bainite and ferrite transformations are improved moderately. The method is especially interesting to industry applications because it can be used with little experimental effort.
Some authors raise the question if it is reasonable to assume that the transformation rate solely depends on temperature and volume fraction [84]. Newer developments show promising results, which may lead to even better prediction of final phase composition and hardness with more advanced and highly complex transformation kinetics including variable transformation start and finish temperatures as well as quenching rate dependency [22]. The disadvantage of those models is the increased modelling effort involved and the acquiring of all relevant parameters. Also, the applicability to arbitrary cooling paths has jet to be shown.

6 Fineblanking and Heat Treatment Simulation

Being able to predict distortion due to heat treatment has great potential in saving manufacturers time and effort during the construction phase of their tools. The aim is to reproduce distortion effects virtually with the finite element method by taking the influencing factors identified in chapter 4 into account. In order to investigate the influence of residual stresses and other important parameters on distortion during heat treatment, finite element simulations can be of great help. Stress evolution, transformation behaviour or position dependent temperature paths can be retraced. This is is key to understand the complex interaction that take place during quenching. Furthermore, the coupling of mechanical forming with subsequent heat treatment simulations is discussed in detail in the coming sections. The FE-software used for the following numerical simulations is FORGE 2011 and its successor FORGE NxT by Transvalor solutions. It was chosen as it allows to perform the mechanical as well as metallurgical heat treatment simulations and the coupling in-between. Material models are not encrypted and can be altered to the needs of the user (as shown in chapter 5). There exist several other suitable commercial software packages that are able to perform heat treatment simulation, for example Dante, Simufact or LS-Dyna.

6.1 Bracket Simulation

The geometry of the billet and the tools used for the forming simulation are identical with the experimental setup. The simulation is performed in three steps; bending, austenitisation and quenching. After bending, residual stresses are either transferred to the austenitisation and quenching simulation (refereed to as group A) or deleted in order to simulate an annealing process (group B). The angles are identified in same manner as for the experimental brackets with the GOM software (see section 4.2.3).

6.1.1 Bending Simulation and Spring-Back

During the cold forming process of bending, the yield curve found in section 3.1.1 was used to predict stresses. The setup before and after closing is illustrated in figure 6.1, where blue is the punch and yellow the die. The rectangular billet in red was approximated by tetrahedron elements. Standard tetrahedron elements are generally not ideal for bending approximations as they tend to overestimate stiffness which is why a mixed formulation that separates displacements and hydrostatic pressure was used [56]. A mesh sensitivity analysis revealed that a minimum of five elements across the thickness of the part are necessary in order to get reliable simulation results [94]. When using five ore more element layers, stresses and angle changes in heat treatment simulations stay approximately the same. For the following evaluations a simulation with seven elements across thickness was used.

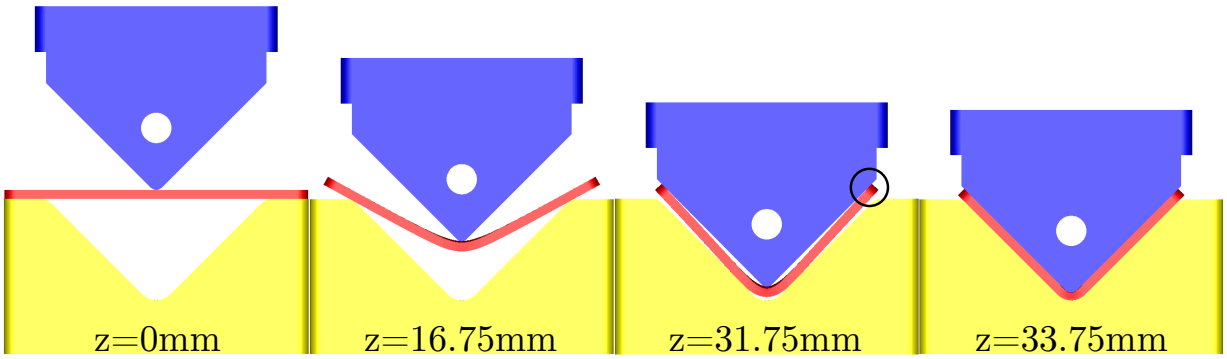

Figure 6.1: Bending process simulation

The beginning of the bracket forming resembles a three point bending test until the sides touch the punch (z=31.75 mm). The bracket is then pushed in the die until reaching its final position (z=33.75 mm). The bending towards the end therefore leads to a negative change in angle after unloading. Before spring-back, the angle between the two sides is given by the active elements and amounts to exactly $\theta_0 = 90°$. The angular change after elastic unloading is predicted with $\Delta\theta_{sb} = -0.46°$ and is simulated by virtually removing the tools. The remaining residual stresses are transferred to the subsequent quenching simulation.

Stress State Before and After Spring-Back

The highest stresses before spring-back are predicted in thickness and width direction in the bending radius. The punch compresses the material leading to a flow perpendicular to the sheet surface resulting in a reduced local thickness and enlarged width. Stresses in x-direction (see figure 6.2) inside the bending radius are most interesting regarding angular change. The stress free neutral line is shifted from the middle of the specimen due to compression induced by the punch.

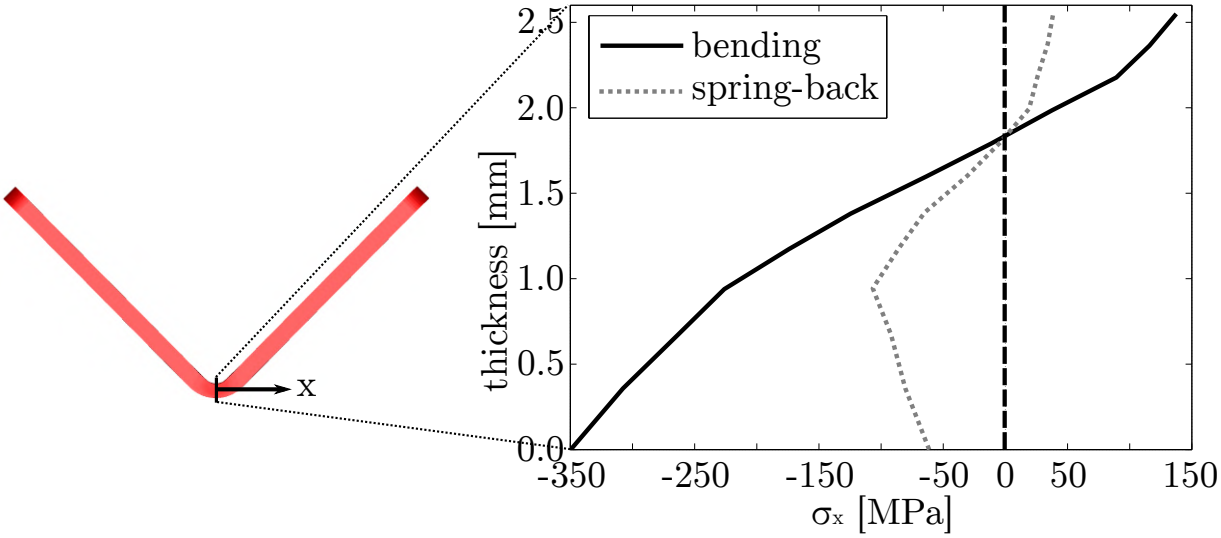

Figure 6.2: Simulated stresses in x-direction in the middle of the specimen before and after spring-back

The stress state before spring back is as expected (solid line); on top of the bending radius tension and bellow compression stresses are induced by the forced opening after the sides touch the punch. Although σ_x is bellow yield strength, the equivalent von Mises stress exceeds elastic limits locally which leads to the final residual stress distribution after spring back (dotted line). Because of the non-uniform stress distribution across the entire section, stresses in figure 6.2 do not cancel each other completely.

6.1.2 Heat Treatment Simulation

All heat treatment simulations use the optimised phase fraction dependent material model of section 5.3. The first simulation (representing group A) transfers the geometry and stresses from the bending simulation to the

austenitising step. This austenitisation is implemented, according to the real process, by heating the bracket at an ambient temperature of 860 °C and a heat transfer coefficient of 10 W/(m^{2}K) modelling stationary air.
A second simulation, representing group B, is performed where all stresses and strains are deleted and only the resulting geometry of the bending simulation is transferred. All other process- and material parameters are unchanged from the previous simulation.
Most residual stresses of the bending simulation (group A) are decomposed during heating due to the very low austenite yield strength of circa 100 MPa at high temperatures. After reaching the maximum temperature, no change of angle is detectable. With increasing temperature and decreasing yield strength, plastic flow takes place in thickness and width direction, where the highest strains are present. Due to slow heating, the temperature of the entire specimen increases equally, thus no significant thermal stresses arise. After complete austenitisation at 860 °C (100% austenite), residual equivalent stresses are smaller than ±50 MPa for group A and ±6 MPa for group B.

Thermal Boundary Conditions

The quenching simulation was modelled with a slightly modified heat transfer coefficient that was provided by Durixol as seen in figure 6.3.

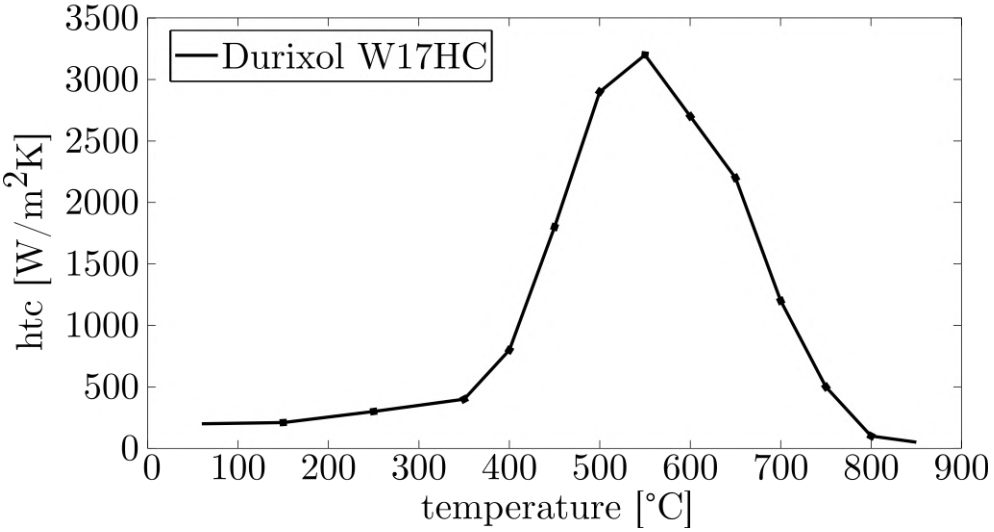

Figure 6.3: Slightly modified heat transfer coefficient (htc) of Durixol W71HC

The temperature of the quenching agent was assumed to stay constantly on 55 °C. The slight increase of the oil bath temperature up to 5 °C during the experiments was neglected. The initial bracket temperature of 860 °C is transferred from the austenitising simulation and so is the phase structure (100% austenite) and stress state.

Temperature and Stress Evolution during Quenching

During the quenching simulation, the nonuniform surface to volume fraction leads to inhomogeneous temperature distribution within the bracket resulting in the emergence of thermal stresses. Figure 6.4 shows temperature over quenching time for an element on the surface (top radius) and an element in the middle of one side.

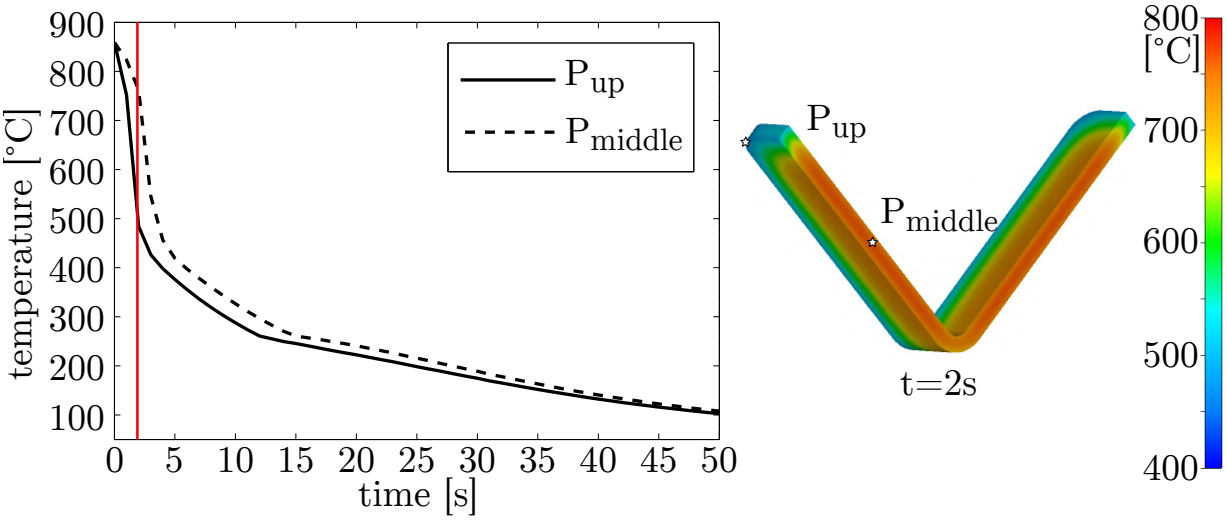

Figure 6.4: Temperature paths of two points during quenching (l) and temperature distribution at t=2 s (r)

Although the two temperature paths are close together, steep cooling at high temperatures leads to a temperature distribution with a gradient of maximum 277 °C between core and surface after two seconds, which is illustrated with a half bracket on the right of figure 6.4. As expected, the core (represented by P_{middle}) keeps temperature longer than the surface. P_{up} has the highest surface to volume ratio and therefore cools down the fastest. The unevenly distributed temperature leads to an increase in thermal stresses. Figure 6.5 shows the resulting stress distribution over time

in the bending radius for brackets of group A (with residual stresses from bending).

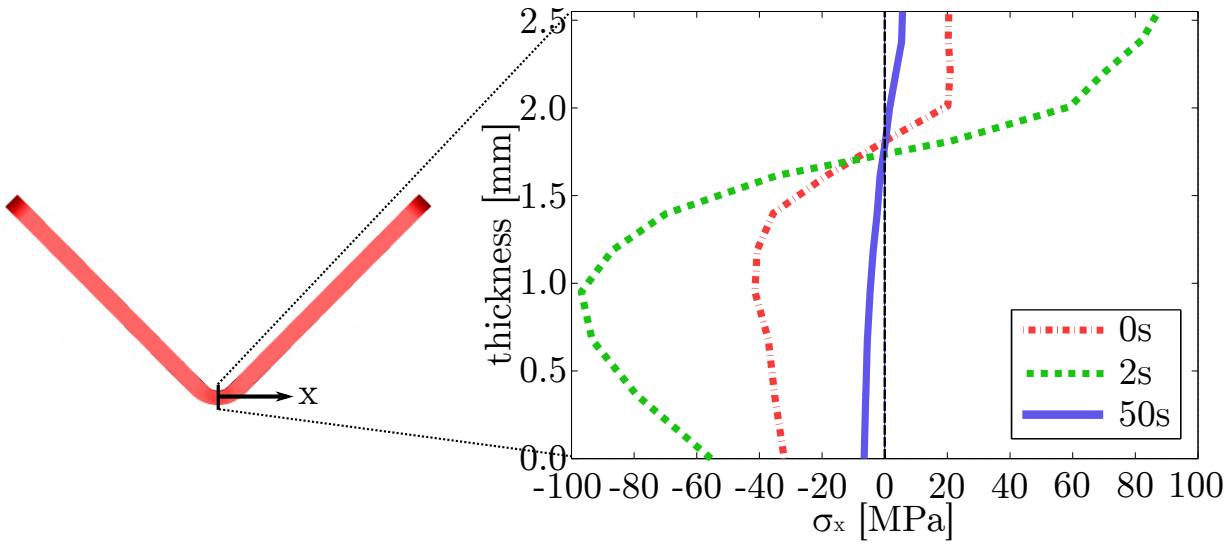

Figure 6.5: Stresses in x-direction during quenching simulation

In the beginning we have a similar stress distribution as for after springback (see figure 6.2), but reduced by the relaxation during austenitisation. After two seconds, when the temperature gradient peaks, stresses increase in tension and compression region. A positive angular change is observable contemporaneously. With progressing cooling and martensite transformation (beginning after 13 seconds) the stresses are reduced until reaching its minimum at the end of the quenching process, when no more phase transformations take place and the temperature is uniformly distributed (50 seconds). The remaining stresses are smaller than $\pm 10\,\mathrm{MPa}$.
Group B (without residual stresses from bending) shows similar behaviour but with fewer stresses at t=0 s and smaller peaks at 2 s of 45 MPa (compared to 100 MPa for group A), leading to a smaller change in angle.

6.1.3 Results and Distortion Prediction

Contradictory to the experiments, the simulation predicts a slight increase in angle between the brackets of $\Delta\theta_A = 0.1°$ after quenching, which can be retraced by looking at the stress evolution during cooling. When deleting all former bending stresses before simulating austenitising and quenching, a very small change of $\Delta\theta_B = -0.03°$ can be observed, which is in line with experimental results.

The bracket simulation shows only small angular deviations between parts that have their stress state transferred from the bending operation compared to initially stress-free heat treatment simulations. This can mainly explained by the decomposition of stresses during austenitising.

6.2 Fineblanking Test Specimen Simulation

The fineblanking test specimen simulation is divided into blanking and heat treatment. Although no clear difference of thermal distortion between fineblanked and water jet cut parts was observed in the experiment series, a significant disparity was seen by altering the quenching direction. The simulation may helps to understand the distortion mechanisms during quenching and possible influences of the blanking process.

6.2.1 Blanking Simulation

In order get optimal results when simulating blanking, a fine mesh in the cutting region is essential. To keep the amount of elements at an acceptable level, mesh boxes along the cutting line with a fine resolution of 0.1 mm are used. Whereas the rest of the mesh is set to 0.8 mm. By taking advantage of the symmetry only 1/8th of the part has to be simulated. The total number of elements is thereby reduced to a tolerable amount in terms of computational time. A remeshing algorithm was used to cope with heavily deformed elements or regions with an excessive stress gradient due to the cutting process.

Damage Criterion

Material failure is a challenging topic and a generally applicable model for all types of processes has jet to be developed. There exist several approaches, one recent work by Wesner addresses failure modelling in fineblanking [121]. Some of the investigated models need extensive material testing and take hydrostatic stress and triaxiality into account. Others assume that material fails after reaching a certain stress or strain limit. As this is a research area for itself and to keep the testing effort small, the widely used failure criteria proposed by Cockroft and Latham is chosen [30]. For

the following simulations the normalised version was used, which can be expressed as

$$C_{CL} = \int_0^{\bar{\varepsilon}} \left(\frac{\sigma_{\max}}{\bar{\sigma}(\bar{\varepsilon})} \right) d\bar{\varepsilon} \tag{6.1}$$

with $\sigma_{\max}$ as the maximum principle stress, $\bar{\sigma}$ is the equivalent stress and $\bar{\varepsilon}$ the effective strain. The critical value of C_{LC} is usually determined with a standard tensile test [50]:

$$C^*_{CL} = \int_0^{\varepsilon_f} \left(\frac{\sigma_f}{\sigma(\varepsilon)} \right) d\varepsilon \tag{6.2}$$

with

$$\varepsilon_f = \ln \left(\frac{A_0}{A_f} \right) \tag{6.3}$$

where A_0 and A_f are the initial and final cross area, thus ε_f is the fracture strain. When $C_{CL} \geq C^*_{CL}$ in an element it is deleted. Hydrostatic and compressive stresses are not taken into account, although they are assumed to be necessary to predict crack initialisation correctly [49]. In this case, the damage criterion is mainly used to separate the steel strip and part for which purpose it is usable. C^*_{CL} is set to 4.5 as this value proved to suit the process of fineblanking best but was not determined with a tensile test. From a physical point of view C^*_{CL} has therefore no meaning but using smaller values lead to rough surfaces on the blanked edge.

Stress Evolution During Blanking

Figure 6.6 shows the Von Mises stress distribution in the shearing zone for different stages during fineblanking.
The future part is held in place by the guide plate and die while the strip is pushed downwards by the punch. The die roll is formed in the beginning of the blanking process. The highest stresses are subsequently concentrating in the shear zone leading to deletion of elements until the part is fully separated from the strip. Some residual stresses are remaining in the part but only very locally. Hence, material that is 2.5 mm or more from the cutting edge is completely stress free. These results support the assumption

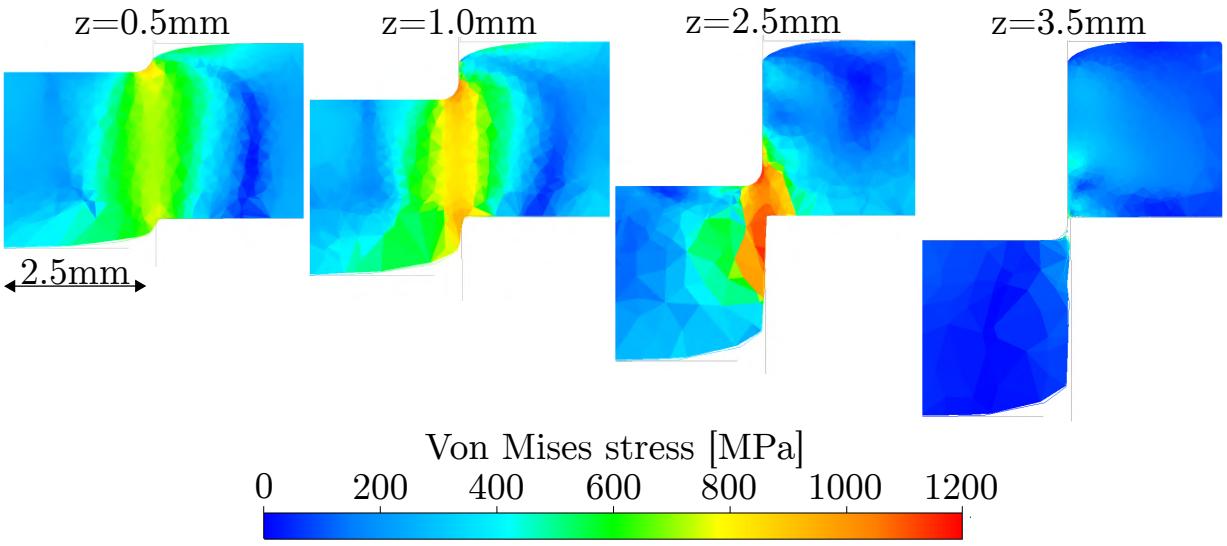

Figure 6.6: Von Mises stress evolution during fine blanking

that residual stresses induced by fineblanking are only present close to the cutting edge.

6.2.2 Heat Treatment Simulation

In the following, heat treatment simulations are separated in an austenitisation and quenching process. The fineblanked parts include stresses and strains transferred from the forming process, whereas the water jet cut parts are simulated with a stress free geometry. Again, the material optimised in section 5.3 was implemented. The same austenitisation set up as presented for the bracket in section 6.2.2 was used.

In order to take the orientation dependency during quenching into account, the heat transfer coefficient has to be temperature- and location dependent. The requirements of thermal boundary conditions and the distortion modi observed in chapter 4 demand to simulate the full geometry. If the same mesh of the bending process was kept and the full geometry would be derived by mirroring, the amount of elements would increase computational time massively. A possibility to deal with that problem is to coarsen the mesh after the blanking simulation in order to reduce the number of elements. It is also an option to neglect fine blanking history altogether as it was shown that only the edge regions of the part are affected (shown in figure 6.6). The two possibilities are further discussed in section 6.2.3.

Thermal Boundary Conditions

Figure 6.7 shows the temperature dependent heat transfer coefficient. By defining three different regions on the part with a slightly altered coefficient, a location dependency is introduced. The heat transfer is changed from the original htc-curve (section 3) by +5% for the middle (section 2) and +10% upper section (section 1). The regions are equally divided along the length of the part. This approach may not reproduce the physical processes explained in section 2.2.1, but can be understood as an artificial imperfection similar to an eccentricity used when simulating buckling problems.

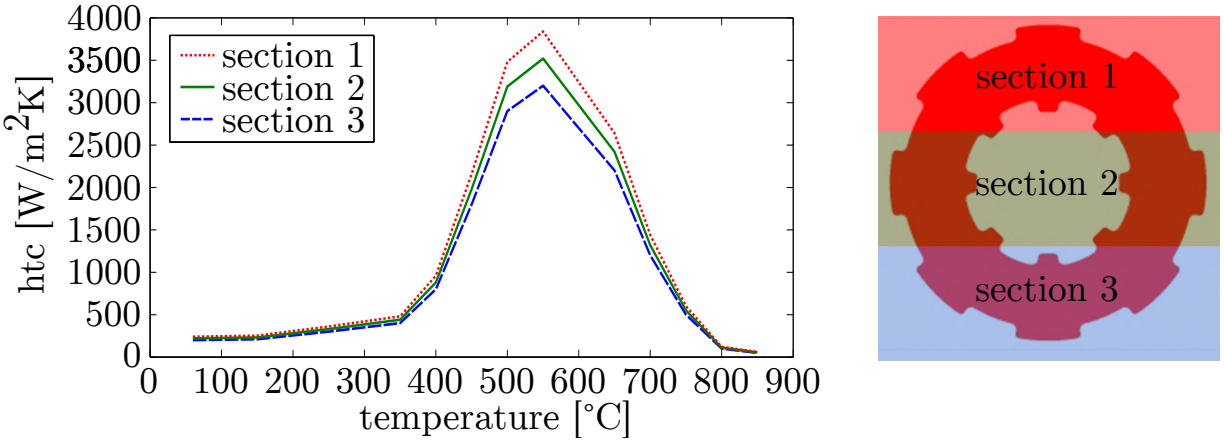

Figure 6.7: Section-wise altered heat transfer coefficient

This setup aims to reproduce the slightly earlier wetting with the quenching oil from one side but completely neglects fluid-dynamic and boiling phenomenon that may occur during quenching. Fluid circulation and boundary layers may be approximated by CFD simulations (a broad overview of the current state of the art on this topic is given by Canale and Totten [28]), but they are hardly reproducible and strongly influenced by neighbouring parts in the quenching basket. Because of the complex nature of this problem, the instability approach seems reasonable as it is reproducible, stable and still allows to have an uneven temperature distribution of the part.

Temperature and Stress Evolution during Quenching

In the first couple of seconds during quenching, the highest temperature gradients and thermal stresses are present. Figure 6.8 shows the simulated temperature distribution after 2, 4, 6 and 8 seconds when quenching

the previously austenitised blanking test specimen with the heat transfer coefficient of figure 6.7.

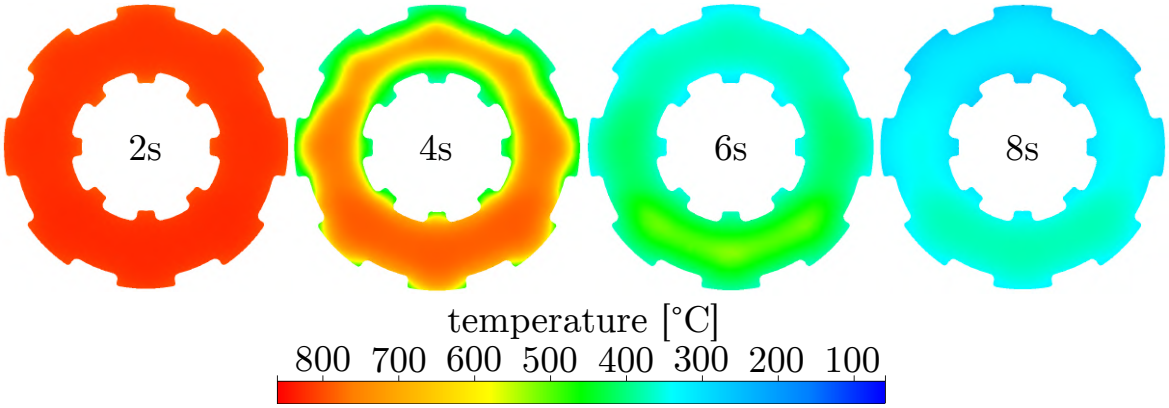

Figure 6.8: Simulated temperature distribution after 2, 4, 6 and 8 seconds

As the heat transfer is small for high temperatures, the location-dependent differences of the three sections are barely visible in the fist stage. After 4 seconds the top part is clearly cooling faster than the middle or bottom region. This is also the moment where highest temperature gradients are present. Figure 6.9 illustrates the temperature evolution for four characteristic points on the part. The measurement points are chosen to visualise the maximum and minimum values for section 1 (red) and 3 (blue). The points in the middle of the part have the smallest surface-to-volume ratio. Hence, they lose temperature more slowly compared to points that lie on the surface of a tooth.
All four points start at the austenitising temperature of 860 °C. After passing 800 °C the heat transfer increases drastically thus the temperature drops to 400 °C in circa 1-2 seconds. The points in sector 2 (blue) have a smaller heat transfer leading to a delayed fast cooling phase. During that period highest temperature differences (up to 350 °C) are observed resulting in equivalent thermal stresses of up to 250 MPa. Locally in the tooth radii, small plastic deformations of circa 1% take place as the yield strength of hot austenite is lower by the high temperatures but no significant impact on global distortion is detected. After the fast quenching phase, cooling decelerates and temperatures move closer together. When austenite starts to transform to martensite after 10 s - 15 s, temperature gradients are much smaller than previously observed. Thermal stresses have already disintegrated to a large extent prior to phase transformations. Hence, the behaviour can be classified as tendency II.

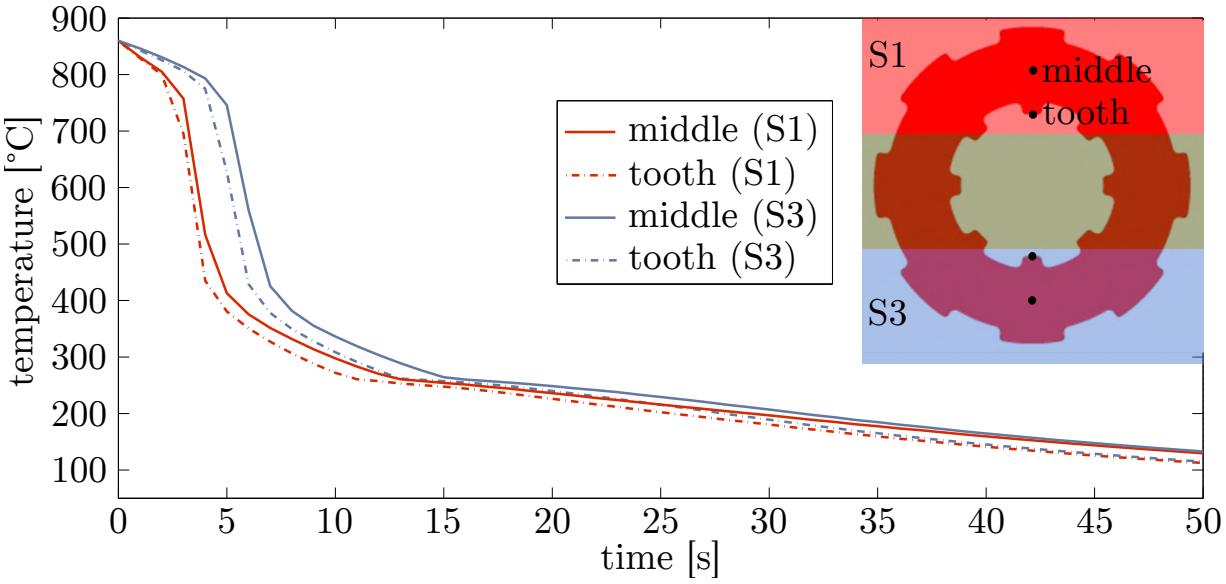

Figure 6.9: Temperature paths of four points during quenching

6.2.3 Results and Distortion Prediction

The predicted final distortion after simulating heat treatment is surprisingly small. Deviations from target geometry can mainly be retraced to martensite volume expansion, but is well bellow 1%. The location and temperature dependent heat transfer was not able to provoke the strong distortion patterns that emerged in the experiment series. Even by changing the heat transfer up to 50% for different sections did not result in significant larger deviations from the CAD geometry. Further, hardly any difference between parts that are simulated stress free prior to heat treatment and parts that account for fineblanking residual stresses was observed. A slightly higher distortion results when changing heat transfer across thickness instead of over the height of the part. Figure 6.10 illustrates geometry change after the quenching simulation 50 times exaggerated for two different heat transfer variations.

The simulated hardness of 680 HV - 687 HV corresponds well with measured values of experimentally hardened parts that averaged 678 HV. Also, micrographs of the specimens indicate full martensite transformation, which is in line with simulation results. When comparing simulated distortion with the experimental data, average deviations after quenching $\overline{D}_{tot} = 0.134\,\text{mm}$ are much higher than what is predicted with the simulation $D_{sim} = 0.003\,\text{mm}$. Nevertheless, the accuracy is difficult to evaluate as some parts in the ex-

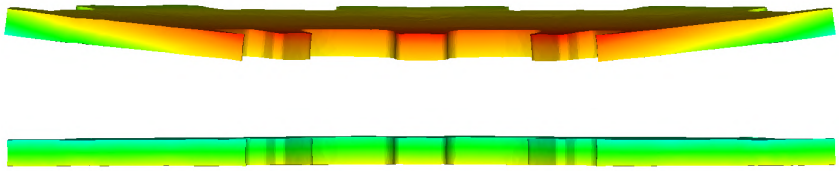

Figure 6.10: Distortion after quenching with htc variation across thickness (top) and across height (bottom) 50x exaggerated

periment series had comparable small changes after heat treatment.
As no significant deviations between simulation with stresses from the blanking process and stress-free parts could be shown. Thus it may be assumed that is not necessary to take stresses caused by pure blanking into account when simulating heat treatment of fineblanked geometries.

6.3 Chain Wheel Simulation

The chain wheel geometry with its complex shape consisting of an offset, gearing and several holes, is used to test the applicability of the previously presented material model and simulation procedure. The experimental results revealed that multiple different distortion modi are present after quenching. The finite element analysis helps understanding the origin of changes in size and shape observed in the quenching experiments.

6.3.1 Forming Simulation

The forming simulation is separated in three steps; blanking of holes to create the fillets, generating the offset and finally blanking of the gearing and inner hole. The embossing stage of the real process was neglected as it is assumed to have little to no influence on the stress state of the part. Furthermore it would require a very fine mesh that increases computational time significantly. The result after each step is illustrated for an eighth of the chain wheel in figure 6.11.
The final simulation, where the gearing is blanked (step 3), was performed with half of the wheel as this is the smallest possible symmetry plane. The

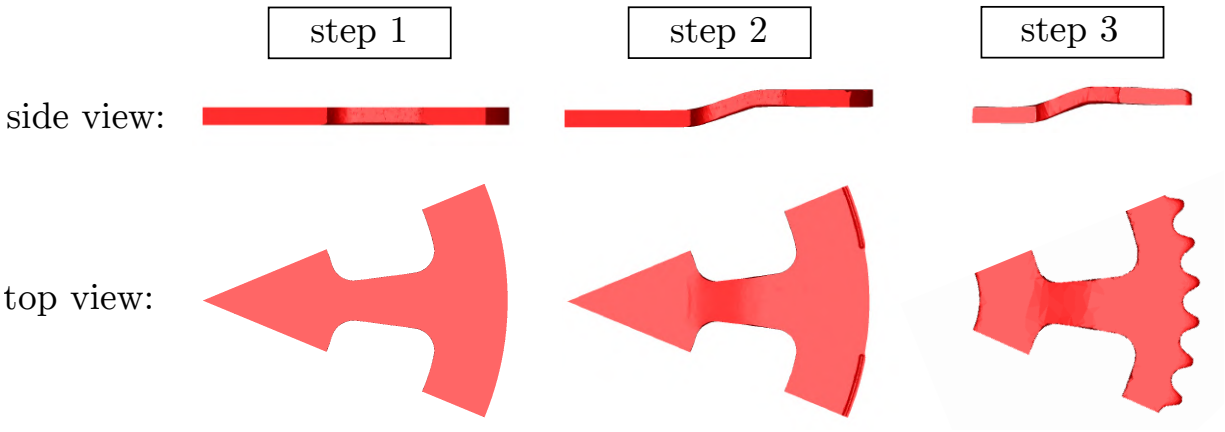

Figure 6.11: Three forming steps of the chain wheel

first step consists of pure fineblanking. The stress is concentrated locally in the shear zone similar to the fineblanked test specimen. During the second step, where the offset is formed, bending stresses are brought into the material that stay partially as residual stresses. Additionally, a v-ring is pushed in the area close to the gearing in order to positively influence the blanking during the third step. Alike the previous fineblanking simulations, a damage value of $C^*_{CL} = 4.5$ was used.

6.3.2 Heat Treatment Simulation

The set-up for the heat treatment simulation was done analogical to the fineblanked test specimen geometry; austenitisation is followed by a quenching simulation. In addition to comparing simulations that account for residual stresses from the blanking and forming process with ones without material history, different heat transfer conditions and their influence on distortion are investigated. Forming steps are simulated with a partial geometry using the symmetry of the part, whereas the quenching simulation is conducted with the full geometry in order to allow distortion patterns observed in the experiments (see chapter 4.4).

Temperature Evolution and Distortion

As expected from previous simulations, high temperature gradients are present during quenching. Because of the high surface-to-volume ratio of the gearing, it cools down faster than the rest of the chain wheel. Figure

6.12 shows the temperature distribution during the first eight seconds with a variable heat transfer coefficient across the length of the part.

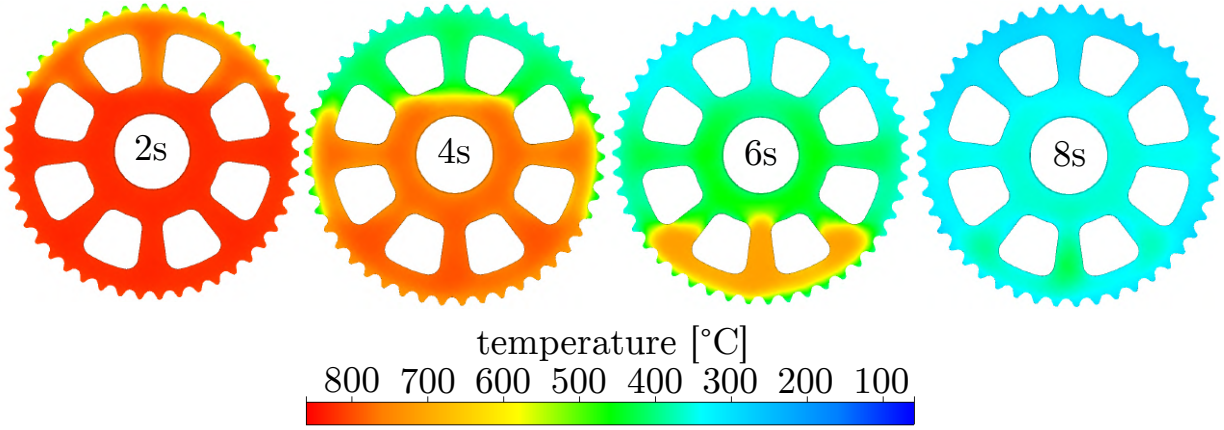

Figure 6.12: Temperature evolution during quenching simulation with a variable heat transfer coefficient across the lenght of the part

The results are comparable to the ones from the fineblanking test specimen but the temperature gradients are even greater. Hence, high thermal stresses and phase transformations overlap in this case which can be classified as distortion tendency III. Therefore the change in size and shape is distinctively more pronounced than seen in previous simulations. The final geometrical changes are visualised in figure 6.13 for two quenching simulations. The one on the right results when a variable heat transfer coefficient across the length of the part, $htc(T, y)$, is applied. The one on the left varies its heat transfer across the thickness, $htc(T, z)$. In both cases the part was divided in three sectors with a +5% and +10% higher heat transfer for the middle and top sector (see figure 6.7).

During quenching with a varying heat transfer across thickness, the cooling of the gearing is accelerated. The outer ring decreases in size and lifts upwards, where it stays until reaching room temperature. When the heat transfer is varied along the length, distortion arises similarly but with an additional asymmetric thermal contraction and followed martensite transformation caused expansion. A more complex, non-symmetric distortion mode is resulting as seen in the right picture of figure 6.13.

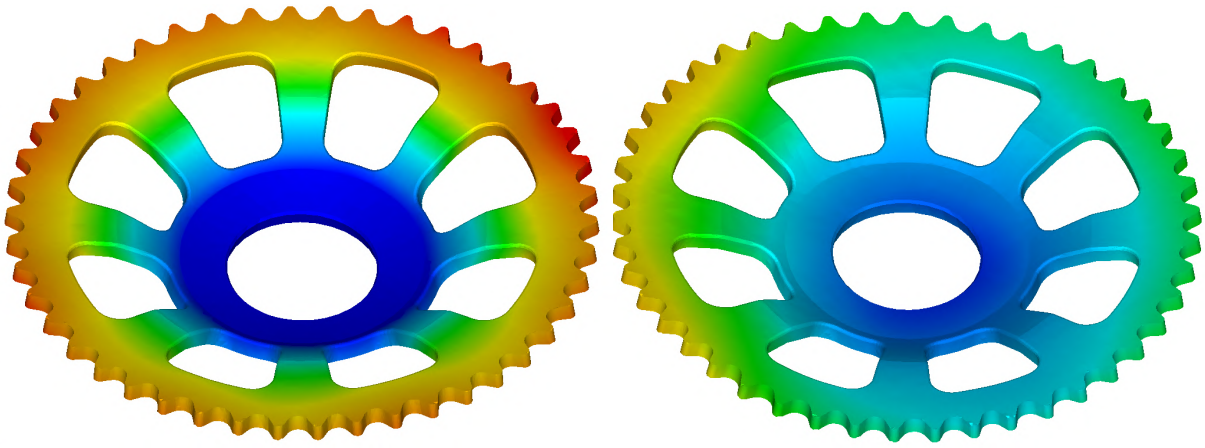

Figure 6.13: Chain wheel quenched with a variable heat transfer across thickness (left) and length (right) 20 times exaggerated

6.3.3 Results and Distortion Prediction

To begin with, heat treatment simulations without considering the forming history are analysed. Each simulation presented in the following was conducted with a different temperature- and location dependent heat transfer coefficient. The final deviations of the simulated meshes from target geometry are determined in the same way as presented for the experimental series with a measurement circle with $r = 46\,\text{mm}$ (see section 4.3.3). Figure 6.14 illustrates final deviations for three quenching simulations.
When not location but pure temperature dependent heat transfer is used ($htc(T)$), a distortion mode results as shown in figure 6.13 on the left. The gearing flips up due to faster cooling of the outer ring. This effect can be amplified when increasing the quenching rate in the gearing region by applying a variable heat transfer across thickness. An increase in deviations from $\overline{D}^{s}_{htc(T)} = 0.116\,\text{mm}$ to $\overline{D}^{s}_{htc(T,z)} = 0.303\,\text{mm}$ is observable. By applying a variable heat transfer along the length of the chain wheel, a more complex distortion mode is resulting with an average of $\overline{D}^{s}_{htc(T,y)} = 0.203\,\text{mm}$. In the experiment series two wave formations, single and double, were the most commonly observed distortion modi. Of the two, only the double wave mode is predicted by one of the presented simulations. However, the mode where the outer ring is solely flipped up was never observed in the experiments. Simulations that account for the forming history show similar behaviour with a slightly increased average distortion of $\overline{D}^{s*}_{htc(T,y)} = 0.210\,\text{mm}$. The small difference may be explained by the die roll originating

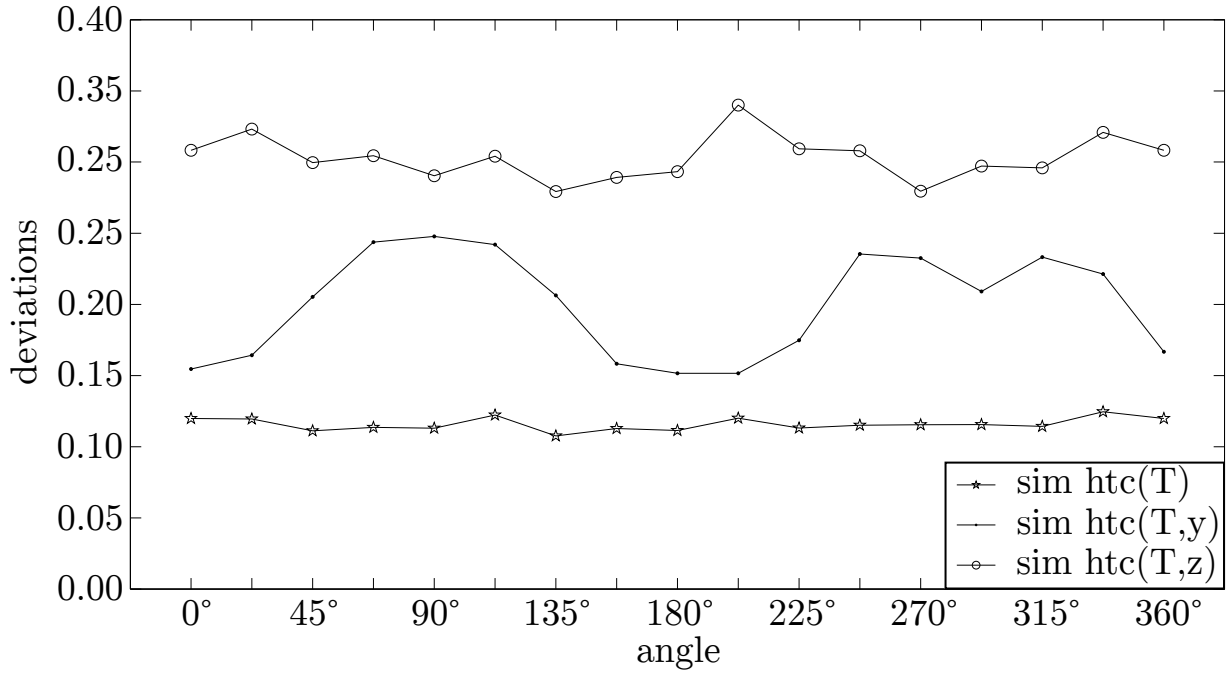

Figure 6.14: Deviations after quenching simulation for three different heat transfer conditions

from the fineblanking simulation or the additional residual stresses from the forming operation.
Depending on the heat transfer modelling, the average distortion is over or underestimated by the simulation. However the predictions can be accurate for some specific parts that were measured experimentally in section 4.4.

6.3.4 Buckling Analysis

As previously mentioned, the deformation patterns observed in the experimental section 4.4 resemble a buckling problem where the post-quenching geometry results in two different modi. A buckling analysis was conducted in order to investigate the shapes of the first two, and therefore most likely to be present, buckling modi. The necessary constraints for the analysis are applied in a way that the chain wheel is fixed at the base (inner ring), where it is most stable. Additionally, a small stress load of 1 MPa per tooth was applied around the gearing representing thermal compression stresses during quenching. The first two buckling or shape modi are shown in figure 6.15.

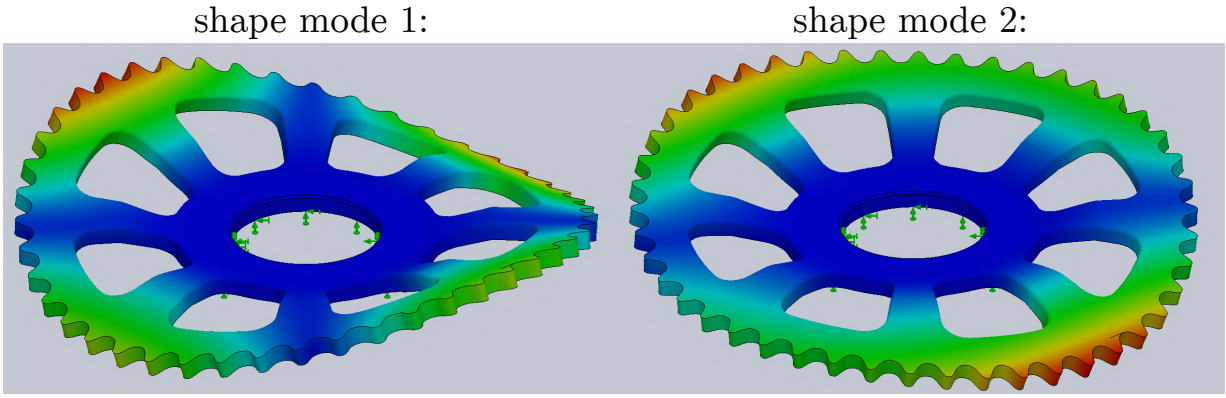

Figure 6.15: First two shape modi of the chain wheel buckling analysis

Interestingly, the two modi align with the experimental observations (see figure 4.30). The two distortion modi, single wave and double wave, were the most commonly measured outcome during the experiment series. Both occur roughly equally often in the experiment series which may be explained by the buckling loads that are close to one another ($\lambda_1 = 4.9 \cdot 10^8$,$\lambda_2 = 5.5 \cdot 10^8$). The buckling analysis fails to predict the general raise of the outer ring which may be due to the simplified load conditions. The incremental simulation with a variable heat treatment coefficient along the length of the chain wheel also resulted in distortion mode 1 but additionally predicted the raise of the outer ring. Based on the good agreement of the predicted and measured distortion modi, the buckling analysis may be used to forecast the most likely distortion patterns. Although the deformation modi seem to fit the observations, the buckling analysis is unable to predict the extent of deviations from target geometry but only its general direction. Therefore other predictive methods are indispensable for accurate forecast of thermal distortion.

6.4 Summary of Heat Treatment Simulations

Generally hardness was well estimated and is in line with the Jominy validation that showed good agreement between simulations and experiments. However, this is favoured by the near 100% martensite phase composition for all parts. Although the simulations results fit the experimental data partially, not all distortion modi can be predicted. In the following, the main findings and results of each geometry are recapitulated.

6.4.1 Bracket

The majority of residual stresses after the bracket bending process disappear during the austenitising simulation. Furthermore, highest temperature gradients are present in the beginning of the quenching process where no phase transformations take place. The resulting change in shape and size can therefore be classified as tendency II (as defined in section 2.2.3). Thus, the angular change that emerges after quenching is only small. By deleting the residual stresses prior to the quenching simulation, and thereby modelling an annealing process, $\Delta\theta_B$ is further reduced, which corresponds well with experimental data.

6.4.2 Fineblanking Test Specimen

In the case of the fineblanked test specimen hardly any difference was observed between quenching simulations that account for residual stresses from the blanking process and stress free simulations. This observation is line with experiments where no significant disparity between fineblanked and water jet cut parts could be shown. Therefore, it can be assumed that the blanking process can mostly be neglected during heat treatment simulations. This is a major advantage as computation time and stability of simulations are improved by a large extent.
The simulation was not able to predict all distortion modi of the experimental series, which may be due to the high variance of the results. Some parts show only small deviations from target geometry and are in good agreement with the simulation, others are heavily distorted. The quenching behaviour of the fineblanked test specimen can also be classified as tendency II as phase transformations occur when core and surface temperature differences are already very small. Consequentially, deviations can be expected to be minor as well. No deterministic relationship between heat treatment boundary conditions and extent of distortion was neither found experimentally or numerically.

6.4.3 Chain Wheel

Because of distinctively different surface-to-volume ratios and the resulting high temperature gradients during quenching, the chain wheel geometry can be classified as tendency III. Martensite transformation and high thermal

stresses occur at the same time resulting in greater simulated change in size and shape than for the other two parts. The influence of residual stresses from the forming simulation was detectable but has only minor influence on the final result. Hence, similar geometries with comparable forming operations may be simulated without considering the forming step.
Although the simulation manages to predict correct phase transformations and hardness with the optimised transformation kinetics, a single simulation can only produce one possible distortion mode. As observed in the experimental chapter, scattering of the result are quite high. Efforts to provoke other modi by creating asymmetrical heat transfer conditions during quenching was partially successful. Buckling analysis may be consulted in order to investigate other distortion modi that are otherwise not predicted. The occurrence of different shape modi after quenching shows the difficulty of possible tool compensation in the forming step.

7 Summary and Outlook

The motivation of this thesis was to bring the predictive capabilities of heat treatment simulations to a level where manufacturing tools can be, at least partially, compensated for thermal distortion. A substantial amount of costs and time are expected to be saved if reworks on tools can be minimised successfully.

First of all, C60E steel was characterised by measuring thermo-mechanical material properties including yield curve, anisotropy and CCT diagram. A modified end-quench experiment was developed in order to measure the hardenability of sheet metal. This test was designed to additionally serve as a validation experiment for the phase transformation behaviour in FE-simulations.

A series of experiments was conducted to identify key influencing factors on thermal distortion in fineblanking processes. The impact of residual stresses, quenching direction, batching and fineblanking on geometrical changes were determined with three different specimens. Distortion was measured with digital image correlation technique before and after treatment steps in order to track geometrical changes of specimens. Even though residual stresses from bending influenced thermal distortion, pure fineblanking did not significantly alter the extent of geometrical changes due to quenching. Thus, the blanking step may be neglected for thermal distortion prediction. Shorter computational time and more stable calculations are resulting as complicated remeshing algorithms and element deletion can be omitted. If the blanking process can be neglected for parts where the zone of influence is more dominant has to be further investigated.

To ensure close to reality FE-simulations, all process and material relevant parameters were identified and modelled according to state of the art procedures. Transformation kinetics proved to be a key factor for the simulation quality. As a widely used method to calculate transformations

kinetics from the material's chemical composition failed to describe experimentally measured phase structure and hardness of quenched specimens, a two step optimisation method was developed and conducted. In the fist step, hardness values of individual phases were optimised. Subsequently, the transformation behaviour was adjusted based on measurements of controlled quenching experiments. The thereby derived transformation kinetics successfully improved simulation results. An additional validation experiment involving the modified end-quench test for sheet metal confirmed the improved prediction capabilities of this approach.

The virtual reproduction of the experiment series in chapter 6 proved to be helpful in understanding and tracing the development of residual stresses and changes in shape and size in specimens. The FE-simulations were able to predict hardness and phase structure as well as distortion after heat treatment in a satisfying manner, provided that material behaviour is previously optimised. The thereby obtained information can already be used to adapt the design of parts or tools before they are manufactured. Furthermore, they can be consulted for choosing a suitable treatment process in order to achieve desired tolerance requirements. Although results aligned well with measured data, the existence of multiple distortion modi and scattering in the experiments impeded direct compensation of manufacturing tools. However, by conducting a buckling analysis all present distortion modi of a chain wheel specimen were detected.

Although the developed optimisation process of transformation kinetics improved simulation results significantly, the behaviour for medium cooling rates was not captured optimally. Some authors suggest that the transformation kinetics must be modelled with respect to varying cooling rates for best results [63, 22]. Moreover, transformation start and finish temperatures should not be kept constant but modelled as variables depending on the current cooling rate [97, 22]. Another approach would be to use closer-to-reality quenching experiments when optimising transformation kinetics. The temperature paths of the controlled quenching experiments, on which the presented two step optimisation is based, differentiate strongly from ones occurring in reality. This potentially leads to inaccuracies when trying to simulate with deviating quenching rates. Realistic temperature paths could be estimated with quenching simulations and further used for the design of experiments used in the optimisation process.

The presented approaches and methods are designed to work with through-hardening processes but may be expanded to additional treatment methods, e.g case hardening. Parts that are subject to case hardening are usually made of low carbon steels (C<0.25%). They enable good formability, machinability and weldability but lack the ability to form hard phases during quenching [71]. A thermochemical treatment, where the surface is enriched with carbon in the austenitisation stage, enables phase transformations to martensite and bainite in the subsequent quenching step. Thus, case hardening results in a hardened, wear-resistant surface while maintaining a relatively ductile core.
When simulating case hardening, the diffusion of carbon and its effect on material behaviour has to be taken into account [108]. The change in carbon content itself can be modelled with Fick's diffusion equation [47, 114]. Furthermore, phase transformation models have to consider carbon content which is not implemented in the presented model. A recently published work by Kim et al., also based on a JMAK[1] approach, incorporates carbon concentration in transformation kinetics [66]. Although final phase structure was well predicted with their model, the adaptability for distortion prediction has jet to be investigated.

[1] see section 5.2.2

8 Appendix

8.1 Modified Jominy Test - Technical Drawings

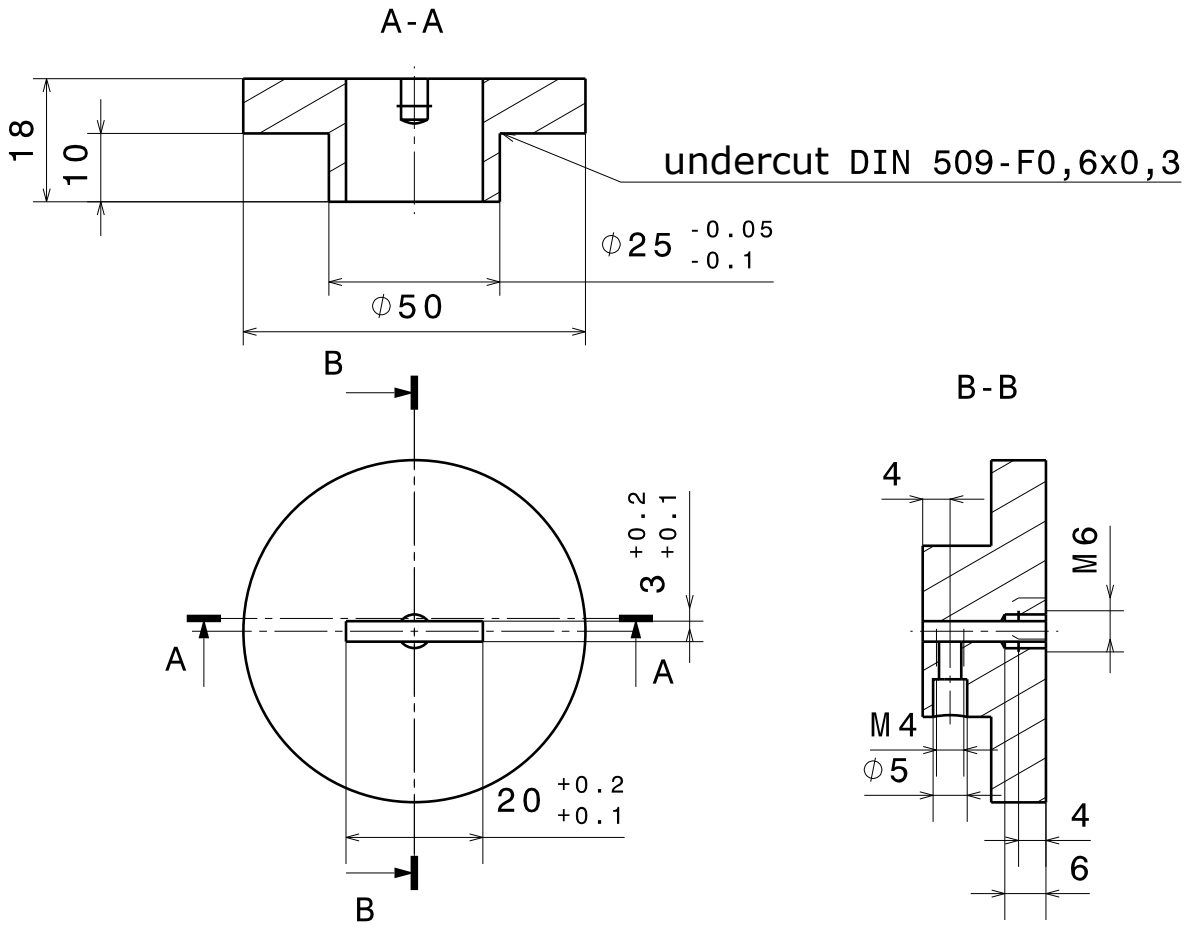

Figure 8.1: Jominy technical drawings - mount

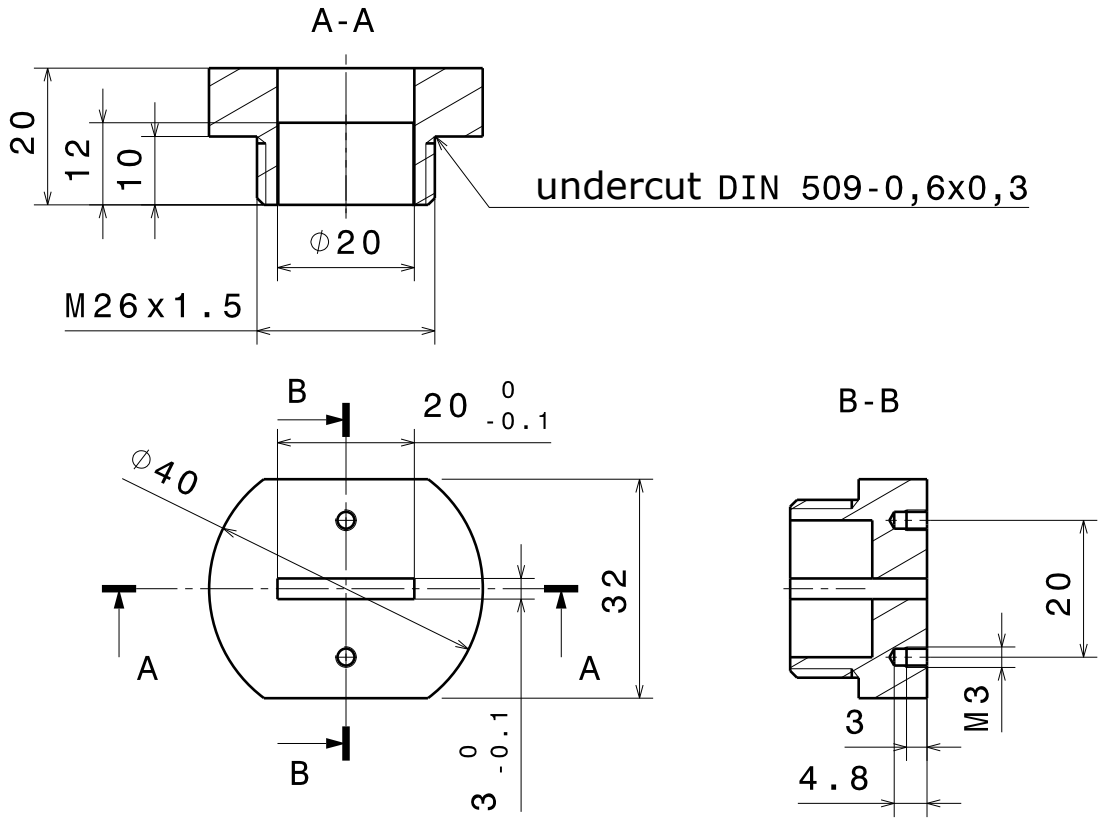

Figure 8.2: Jominy technical drawings - water outlet

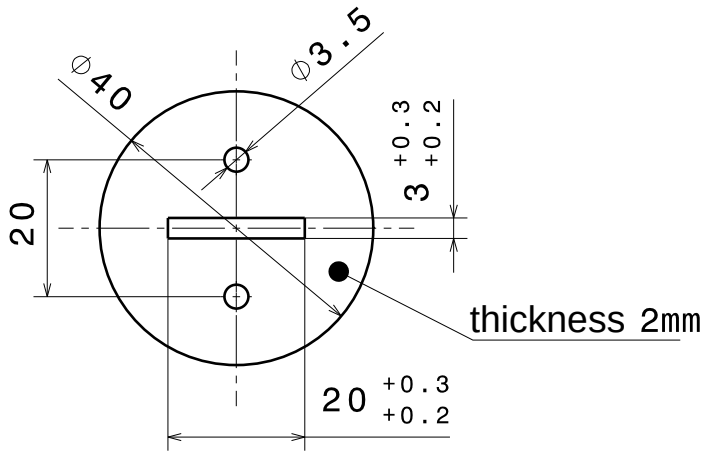

Figure 8.3: Jominy technical drawings - plate with slit

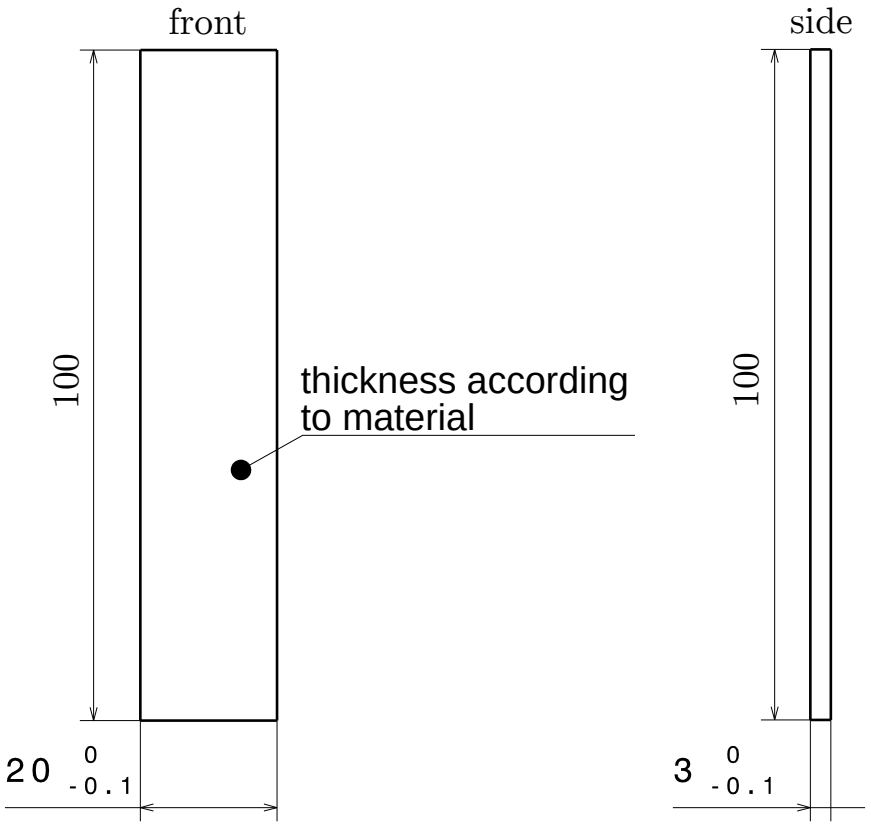

Figure 8.4: Jominy technical drawings - specimen

8.2 Multiphase Material Model During Quenching

8.2.1 Isothermal Transformation

Table 8.1: Optimised Ferrite Isothermal Transformation I

T $[°C]$	t_{start}	$t_{10\%}$	$t_{90\%}$	y_{max}
470.0	2.1	4.3	9.4	0.40
480.0	1.9	3.7	7.9	0.40
490.0	1.7	3.2	6.7	0.40
500.0	1.5	2.8	5.7	0.40
510.0	1.4	2.6	5.0	0.40
520.0	1.3	2.3	4.4	0.40
530.0	1.2	2.1	4.0	0.40
540.0	1.1	2.0	3.7	0.40
550.0	1.1	1.9	3.4	0.40
560.0	1.0	1.8	3.2	0.40
570.0	1.0	1.7	3.1	0.40
580.0	0.99	1.7	3.0	0.40
590.0	0.98	1.7	3.1	0.40
600.0	0.98	1.7	3.2	0.40

Table 8.2: Optimised Ferrite Isothermal Transformation II

T $[°C]$	t_{start}	$t_{10\%}$	$t_{90\%}$	y_{max}
610.0	0.99	1.7	3.3	0.40
620.0	1.0	1.8	3.6	0.40
630.0	1.1	2.0	4.1	0.40
640.0	1.1	2.2	4.8	0.40
650.0	1.2	2.5	5.7	0.40
660.0	1.3	2.8	6.3	0.40
670.0	1.5	3.1	7.1	0.40
680.0	1.7	3.6	8.1	0.40
690.0	2.0	4.2	9.7	0.40
700.0	2.5	5.2	12.	0.40
710.0	3.2	6.7	15.	0.50
720.0	4.4	9.1	21.	0.6
730.0	6.4	13.	31.	0.6
740.0	10.	22.	50.	7,12E+01
750.0	20.	41.	94.	2,53E+01
760.0	49.	1.01E+02	2.31E+02	1,00E-13
770.0	2.02E+02	4.19E+02	9.58E+02	1,00E-13
780.0	4.91E+03	1.02E+04	2.32E+04	1,00E-13
790.0	1.00E+06	2.00E+06	3.00E+06	1,00E-13

Table 8.3: Optimised Perlite Isothermal Transformation

T $[°C]$	t_{start}	$t_{10\%}$	$t_{90\%}$	y_{max}
570.0	3.4	7.1	16.	0.8
582.7	3.4	7.0	16.	0.8
595.3	3.4	7.0	16.	0.8
608.0	3.5	7.2	17.	0.8
620.7	3.7	7.7	18.	0.8
633.3	4.0	8.3	19.	0.8
646.0	4.6	9.4	22.	0.8
658.7	5.4	11.	25.	0.8
671.3	6.7	14.	31.	0.8
684.0	8.8	18.	42.	0.8
696.7	13.	26.	61.	0.8
701.4	21.	44.	9.96E+01	0.6
706.0	42.	87.	2.00E+02	0.52
710.7	1.21E+02	2.50E+02	5.72E+02	0.4
715.3	8.25E+02	1.71E+03	3.90E+03	0.4
720.0	1.00E+06	2.00E+06	3.00E+06	1.000E-16

Table 8.4: Optimised Bainite Isothermal Transformation I

T $[°C]$	t_{start}	$t_{10\%}$	$t_{90\%}$	y_{max}
10.0	1.00E+06	2.00E+06	3.00E+06	0.6
21.0	1.00E+06	2.00E+06	3.00E+06	0.6
31.9	1.00E+06	2.00E+06	3.00E+06	0.6
42.9	1.00E+06	2.00E+06	3.00E+06	0.6
53.8	1.00E+06	2.00E+06	3.00E+06	0.6
64.8	1.00E+06	2.00E+06	3.00E+06	0.6
75.7	1.00E+06	2.00E+06	3.00E+06	0.6
86.7	1.00E+06	2.00E+06	3.00E+06	0.6
97.6	1.00E+06	2.00E+06	3.00E+06	0.6
108.6	1.00E+06	2.00E+06	3.00E+06	0.6
119.5	1.00E+06	2.00E+06	3.00E+06	0.6
130.5	1.00E+06	2.00E+06	3.00E+06	0.6
141.4	5.37E+05	1.11E+06	2.95E+06	0.6
152.4	2.45E+05	5.08E+05	1.34E+06	0.6
163.3	1.16E+05	2.41E+05	6.39E+05	0.6
174.3	5.74E+04	1.19E+05	3.15E+05	0.6
185.2	2.94E+04	6.08E+04	1.61E+05	0.6
196.2	1.55E+04	3.21E+04	8.51E+04	0.6
207.2	8.45E+03	1.75E+04	4.64E+04	0.6
218.1	4.74E+03	9.82E+03	2.60E+04	0.6
229.1	2.73E+03	5.67E+03	1.50E+04	0.6
240.0	1.62E+03	3.35E+03	8.89E+03	0.6
251.0	9.82E+02	2.04E+03	5.39E+03	0.6
261.9	6.10E+02	1.26E+03	3.35E+03	0.6
272.9	3.88E+02	8.03E+02	2.13E+03	0.6
283.8	2.51E+02	5.21E+02	1.38E+03	0.6
294.8	1.66E+02	3.45E+02	9.14E+02	0.6

Table 8.5: Optimised Bainite Isothermal Transformation II

T $[°C]$	t_{start}	$t_{10\%}$	$t_{90\%}$	y_{max}
305.7	1.12E+02	2.33E+02	6.17E+02	0.6
316.7	77.	1.60E+02	4.25E+02	0.6
327.6	54.	1.12E+02	2.97E+02	0.6
338.6	39.	80.	2.12E+02	0.6
349.5	28.	58.	1.54E+02	0.6
360.5	21.	43.	1.13E+02	0.6
377.1	15.	32.	85.	0.6
382.4	12.	24.	64.	0.6
387.8	9.1	19.	50.	0.6
393.2	7.1	15.	39.	0.6
398.5	5.7	12.	31.	0.6
403.9	4.6	9.5	25.	0.6
409.3	3.8	7.8	21.	0.6
410.0	3.1	6.5	17.	0.6
420.0	2.7	5.5	15.	0.6
430.0	2.3	4.8	13.	0.6
440.0	2.0	4.2	11.	0.6
450.0	1.8	3.7	9.9	0.6
460.0	1.7	3.4	9.1	0.6
470.0	1.5	3.2	8.5	0.6
480.0	1.5	3.1	8.1	0.6
490.0	1.5	3.0	8.1	0.6
500.0	1.5	3.1	8.3	0.6
510.0	1.6	3.4	8.9	0.6
520.0	1.8	3.8	10.	0.6
530.0	2.3	4.7	12.	0.6

Table 8.6: Optimised Bainite Isothermal Transformation III

T $[°C]$	t_{start}	$t_{10\%}$	$t_{90\%}$	y_{max}
540.0	3.2	6.6	17.	0.6
550.0	3.8	7.8	18.	0.6
560.0	3.6	7.4	17.	0.6
570.0	3.4	7.1	16.	0.6
580.0	3.4	7.0	16.	0.6

8.2.2 Elasticity Laws

Table 8.7: Austenite Elasticity Laws

T [$°C$]	Young's modulus [Pa]	Poisson's ratio
0	195000	0.30
100	190000	0.30
200	186000	0.30
300	180000	0.30
400	172000	0.30
500	162000	0.30
600	150000	0.30
700	135000	0.30
800	125000	0.30
900	120000	0.30
1200	120000	0.30

Table 8.8: Ferrite and Perlite Elasticity Laws

T [$^{\circ}C$]	Young's modulus [Pa]	Poisson's ratio
0	214000	0.30
100	210000	0.30
200	204000	0.30
300	196000	0.30
400	187000	0.30
500	175000	0.30
600	161000	0.30
700	146000	0.30
800	129000	0.30
1200	129000	0.30

Table 8.9: Bainite Elasticity Laws

T [$^{\circ}C$]	Young's modulus [Pa]	Poisson's ratio
0	214000	0.30
100	210000	0.30
200	204000	0.30
300	196000	0.30
400	187000	0.30
500	175000	0.30
1200	175000	0.30

Table 8.10: Martensite Elasticity Laws

T [$°C$]	Young's modulus [Pa]	Poisson's ratio
0	214000	0.30
100	210000	0.30
200	204000	0.30
300	196000	0.30
1200	196000	0.30

8.2.3 Rheological Laws

The following parameters are used in context of the plastic behaviour law presented in formula 2.75:

$$\sigma_{y(i)} = \sigma_{0(i)} + H_i {\varepsilon_v}^{n_i} + K_i \dot{\varepsilon}_v^{m_i} \tag{8.1}$$

Table 8.11: Austenite Rheological Law

T $[°C]$	σ_0	K	m	H	n_1
20	139	0	0.2	792	0.4
300	97.4	0	0.2	565	0.4
750	30.5	45	0.2	200	0.4
900	8.2	73	0.2	78.3	0.4
1200	8.2	73	0.2	78.3	0.4

Table 8.12: Ferrite Rheological Law

T $[°C]$	σ_0	K	m	H	n_1
20	209	0	0.2	354	0.4
300	107	0	0.2	188	0.4
750	14.4	21.2	0.2	29.5	0.4
900	2.1	18.9	0.2	6.8	0.4
1200	2.	18.9	0.2	6.8	0.4

Table 8.13: Perlite Rheological Law

T $[°C]$	σ_0	K	m	H	n_1
20	363	0	0.2	948	0.3
50	360	0	0.2	945	0.3
100	355	0	0.2	930	0.3
150	350	0	0.2	920	0.3
200	345	0	0.2	910	0.3
250	335	0	0.2	885	0.3
300	325	0	0.2	860	0.3
350	310	48	0.2	820	0.3
400	295	95	0.2	780	0.3
450	270	143	0.2	715	0.3
500	240	190	0.2	645	0.3
550	200	238	0.2	560	0.3
575	175	261	0.2	510	0.3
600	150	285	0.2	451	0.3
630	120	300	0.2	360	0.3
680	33	308	0.2	208	0.3
1200	33	308	0.2	208	0.3

Table 8.14: Bainite Rheological Law

T $[°C]$	σ_0	K	m	H	n_1
20	850	0	0.2	4300	0.4
100	820	0	0.2	4270	0.4
150	800	0	0.2	4245	0.4
250	730	0	0.2	4170	0.4
320	650	0	0.2	4110	0.4
450	500	0	0.2	4000	0.4
1200	500	0	0.2	4000	0.4

Table 8.15: Martensite Rheological Law

T $[°C]$	σ_0	K	m	H	n_1
20	900	0	0.2	7700	0.5
100	890	0	0.2	7700	0.5
200	860	0	0.2	7700	0.5
300	820	0	0.2	7700	0.5
1200	820	0	0.2	7700	0.5

8.2.4 Thermal Parameters

Table 8.16: Austenite Thermal Parameters

T [$^{\circ}C$]	ρ [Kg/m^3]	c_p [J/(Kg K)]	λ [W/(m K)]
0	8040	520	15.00
20	8032	520	15.00
100	8001	530	16.50
200	7959	540	18.00
300	7914	560	19.50
400	7868	580	20.80
500	7820	590	21.80
600	7772	610	22.80
700	7722	620	24.30
800	7671	630	25.50
900	7621	650	27.00
1000	7570	660	28.50
1200	7570	660	28.50

Table 8.17: Ferrite Thermal Parameters

T [$^{\circ}C$]	ρ [Kg/m^3]	c_p [J/(Kg K)]	λ [W/(m K)]
0	7889	460	76.00
20	7883	470	74.40
100	7859	495	68.30
200	7827	525	61.10
300	7794	570	54.50
400	7759	610	48.40
500	7723	690	43.00
600	7686	795	38.30
700	7648	900	34.20
800	7609	1000	30.80
900	7570	1100	29.80
1000	7531	1200	28.80
1200	7531	1200	28.80

Table 8.18: Perlite, Bainite & Martensite Thermal Parameters

T [$°C$]	ρ [Kg/m^3]	c_p [J/(Kg K)]	λ [W/(m K)]
0	7854	460	49.50
20	7848	470	49.50
100	7825	495	47.50
200	7793	525	45.50
300	7759	570	43.50
400	7724	610	40.80
500	7688	690	38.00
600	7651	795	35.00
700	7614	900	32.00
800	7575	1000	30.00
900	7537	1100	29.00
1000	7498	1200	28.00
1200	7498	1200	28.00

Table 8.19: Thermal Expansion Coefficients

T [$°C$]	α austenite	α ferrite	α perlite	α bainite	α martensite
0	1.55E-05	1.19E-05	1.19E-05	1.19E-05	1.19E-05
20	1.59E-05	1.22E-05	1.22E-05	1.22E-05	1.22E-05
100	1.71E-05	1.31E-05	1.31E-05	1.31E-05	1.31E-05
200	1.83E-05	1.40E-05	1.40E-05	1.40E-05	1.40E-05
300	1.92E-05	1.47E-05	1.47E-05	1.47E-05	1.47E-05
400	2.00E-05	1.53E-05	1.53E-05	1.53E-05	1.53E-05
500	2.06E-05	1.58E-05	1.58E-05	1.58E-05	1.58E-05
600	2.12E-05	1.63E-05	1.63E-05	1.63E-05	1.63E-05
700	2.17E-05	1.67E-05	1.67E-05	1.67E-05	1.67E-05
800	2.21E-05	1.70E-05	1.70E-05	1.70E-05	1.70E-05
900	2.23E-05	1.72E-05	1.72E-05	1.72E-05	1.72E-05
1000	2.24E-05	1.72E-05	1.72E-05	1.72E-05	1.72E-05
1200	2.24E-05	1.72E-05	1.72E-05	1.72E-05	1.72E-05

Bibliography

[1] Ahrens, U. ; Maier, H. J. ; Maksoud, A. EL. M.: Stress affected transformation in low alloy steels-factors limiting prediction of plastic strains. In: *Journal de Physique IV (Proceedings)* Bd. 120, EDP sciences, 2004, S. 615–623

[2] Åkerström, P. ; Oldenburg, M.: Austenite decomposition during press hardening of a boron steel-Computer simulation and test. In: *Journal of Materials Processing Technology* 174 (2006), Nr. 1-3, S. 399–406

[3] Akin, J.E.: *Buckling Analysis*. 2009. – 182–188 S. – ISBN 9813107928

[4] Altenbach, Holm: *Continuum Mechanics*. 2015. – 354 S. – ISBN 9788578110796

[5] Andrews, K. W.: Empirical formulae for the calculation of some transformation temperatures. In: *J. Iron Steel Inst* 203 (1965), Nr. 7, S. 721–727

[6] Avrami, M.: Kinetics of Phase Change. I General Theory. In: *The Journal of Chemical Physics* 7 (1939), S. 1103–1112. – ISSN 00219606

[7] Avrami, Melvin: Kinetics of Phase Change. II Transformation-Time Relations for Random Distribution of Nuclei. In: *The Journal of Chemical Physics* 8 (1940), Nr. 2, S. 212. – ISSN 00219606

[8] Avrami, Melvin: Granulation, Phase Change, and Microstructure Kinetics of Phase Change. III. In: *The Journal of Chemical Physics* 9 (1941), Nr. 2, S. 177. – ISSN 00219606

[9] Babu, K. ; Prasanna Kumar, T. S.: Comparison of austenite decomposition models during finite element simulation of water quenching and air cooling of AISI 4140 steel. In: *Metallurgical and Materials*

Transactions B: Process Metallurgy and Materials Processing Science 45 (2014), Nr. 4, S. 1530–1544. – ISBN 1166301400

[10] Bargel, H.J. ; Schulze, G.: *Werkstoffkunde*. 2008. – ISBN 978-3-8348-0295-8

[11] BARTEC Messtechnik und Sensorik: Emissionsfaktor-Tabelle. 2001 (09929). – Forschungsbericht. – 8 S

[12] Bathe, K.: *Finite element procedures*. Klaus-Jurgen Bathe, 2006. – ISBN 097900490X

[13] Belytschko, T. ; Liu, W. K. ; Moran, B. ; Elkhodary, K.: *Nonlinear finite elements for continua and structures*. John Wiley & Sons, 2013. – ISBN 1118700082

[14] Benninghoff, H.: *Wärmebehandlung der Bau- und Werkzeugstähle*. BAZ-Buchverlag, 1978 (Sigma : Fachbuchreihe zur Fertigungstechnik. Gruppe: Werkstoff-, Oberflächen- und Wärmebehandlungstechnik). – ISBN 9783858150400

[15] Berens, F. ; Göbel, M. ; Klingemann, R. ; LÜBBEN, T. ; Majorek, A. ; Neumeier, F. ; Schmitt, G. ; Wägner, M.: Untersuchung von Wärmebehandlungssystemen hinsichtlich ihrer Auswirkungen auf Mass- und Formänderungen mittels eines einfachen Prüfkörpers: Bericht aus dem AWT-Fachausschuss 15 Mass -und Formänderungen infolge Wärmebehandlung. In: *HTM. Härtereitechnische Mitteilungen* 56 (2001), Nr. 3, S. 206–214. – ISSN 0341-101X

[16] Bergen, R. T. von: Effects of quenchant media selection and control on the distortion of engineered steel parts. In: *Proceedings of the 2nd ASM Heat Treatment and Surface Engineering Conference. Part 1 (of 2)* 163-6 (1994), Nr. pt 1, S. 139–150

[17] Berisha, B.: *Computational Modeling of Combined Hardening Phenomena Based on Dislocation Density Theory*. – ISBN 9783909386451

[18] Berns, M.: Verzug von Stählen infolge Wärmebehandlung. In: *Materialwissenschaft und Werkstofftechnik* 8 (1977), may, Nr. 5, S. 149–157. – ISSN 1521-4052

[19] Besserdich, G. ; Müller, H. ; Macherauch, E.: Experimentelle Erfassung der Umwandlungsplastizität und ihre Auswirkung auf Eigenspannungen und Verzüge: simulation der Härtung von Stahlzylindern. In: *HTM. Härterei-technische Mitteilungen* 50 (1995), Nr. 6, S. 389–396. – ISSN 0341-101X

[20] Bhadeshia, H. K.: Martensite and Bainite in Steels : Transformation Mechanism & Mechanical Properties. In: *Le Journal de Physique IV* 07 (1997), Nr. C5, S. C5–367–C5–376. – ISBN 1155-4339

[21] Bohemen, S. M. C. van: Bainite and martensite start temperature calculated with exponential carbon dependence. In: *Materials Science and Technology* 28 (2012), Nr. 4, S. 487–495. – ISSN 0267-0836

[22] Bok, H. H. ; Kim, S. N. ; Suh, D. W. ; Barlat, F. ; Lee, M. G.: Non-isothermal kinetics model to predict accurate phase transformation and hardness of 22MnB5 boron steel. In: *Materials Science and Engineering A* 626 (2015), S. 67–73. – ISSN 09215093

[23] Boltzmann, L.: Ableitung des Stefan'schen Gesetzes, betreffend die Abhängigkeit der Wärmestrahlung von der Temperatur aus der electromagnetischen Lichttheorie. In: *Annalen der Physik* 258 (1884), Nr. 6, S. 291–294. – ISSN 1521-3889

[24] Bomas, H. ; Lübben, T. ; Zoch, H. W. ; Mayr, P.: Die Beeinflussung des Verzuges einsatzgehärteter Bauteile durch Abschreckvorrichtungen. In: *HTM Härterei-Techn. Mitt* 45 (1990), Nr. 3

[25] Bryson, William E.: *Heat treatment : Master Control Manual*. [2. Aufl.]. München : Hanser, 2015. – ISBN 978-1-56990-485-5

[26] Buchmayr, B. ; Kirkaldy, J. S.: Modeling of the Temperature Field, Transformation Behavior, Hardness and Mechanical Response of Low Alloy Steels during Cooling from the Austenite Region. In: *Journal of Heat Treating* 8 (1990), S. 127–136. – ISSN 01909177

[27] Burdorf GmbH: Data Sheet: Durixol W71HC. – Forschungsbericht

[28] Canale, L. C. F. ; Totten, G. E.: Quenching technology: a selected overview of the current state-of-the-art. In: *Materials Research* 8 (2005), Nr. 4, S. 461–467. – ISBN 0500040001

[29] Chatterjee, S. ; Wang, H.-S. ; Yang, J. R. ; Bhadeshia, H. K. D. H.: Mechanical stabilisation of austenite. In: *Materials Science and Technology* 22 (2006), Nr. 6, S. 641–644. – ISBN 0267-0836

[30] Cockcroft, M. G. ; Latham, D. J.: Ductility and the workability of metals. In: *J Inst Metals* 96 (1968), Nr. 1, S. 33–39

[31] Comini, G. ; Del Guidice, S. ; Lewis, R. W. ; Zienkiewicz, O. C.: Finite element solution of non-linear heat conduction problems with special reference to phase change. In: *Int. J. num. Meth. Engng.* 8 (1974), Nr. 3, S. 613–624. – ISBN 0029-5981

[32] Denis, S.: Considering stress-phase transformation interactions in the calculation of heat treatment residual stresses. In: *Mechanics of solids with phase changes*. Springer, 1997, S. 293–317

[33] Denis, S. ; Gautier, E. ; Simon, A. ; Beck, G.: *Stress-phase-transformation interactions - basic principles, modelling, and calculation of internal stresses*. 1985

[34] Denis, S. ; Gautier, E. ; Sjöström, S. ; Simon, A.: Influence of stresses on the kinetics of pearlitic transformation during continuous cooling. In: *Acta Metallurgica* 35 (1987), Nr. 7, S. 1621–1632. – ISSN 0001-6160

[35] Denis, S. ; Simon, A. ; Beck, G.: Estimation of the effect of stress/phase transformation interaction when calculating internal stress during martensitic quenching of steel. In: *Transactions of the Iron and Steel Institute of Japan* 22 (1982), Nr. 7, S. 504–513. – ISSN 0021-1583

[36] Denis, S. ; Sjostrom, S. ; Simon, A.: Coupled temperature, stress, phase transformation calculation model numerical illustration of the internal stresses evolution during cooling of an Eutectoid carbon steel cylinder. In: *Metallurgical Transaction* 18A (1987), Nr. July, S. 1203–1212. – ISSN 03602133

[37] Deutsche Industrienorm: *DIN EN 10052: Begriffe der Wärmebehandlung von Eisenwerkstoffen*. 1994

[38] Deutsche Industrienorm: *EN ISO 642: Steel - Hardenability test by end quenching (Jominy test).* 1999

[39] Deutsche Industrienorm: *EN 10204: Metallische Erzeugnisse - Arten von Prüfbescheinigungen.* 2004

[40] Deutsche Industrienorm: *DIN 8588: Fertigungsverfahren Zerteilen - Einordnung, Unterteilung, Begriffe.* 2013

[41] Deutsche Industrienorm: *DIN 50125: Prüfung metallischer Werkstoffe - Zugproben.* 2016

[42] Eckstein, H.: *Technologie der Wärmebehandlung von Stahl.* 2., stark. Leipzig : VEB Deutscher Verlag für Grundstoffindustrie, 1987. – 672 S. S. – ISBN 3-342-00220-4

[43] Edelstahl Witten-Krefeld GmbH: *Datasheet Thyrofort - heat-treatable steels.* 2016

[44] Ehlers, M.: *Numerische und experimentelle Untersuchung zur Eigenspannungs- und Vorzugsausbildung beim martensitischen Härten von Stufenzylindern und Quadern in verdampfenden Flüssigkeiten.* Band 6/200. Aachen : Shaker verlag, 2000. – ISBN 3-8265-8186-5

[45] Ehlers, M. ; Güttler, J. ; Schwarzer, J.: Computer Aided Simulation of Heat Treatment (CASH): Teil 1: Ein Überblick. In: *HTM Härtereitechnische Mitteilungen* 61 (2006), Nr. 1, S. 5–9. – ISSN 0341-101X

[46] Embury, J. D. ; Deschamps, A. ; Brechet, Y.: The interaction of plasticity and diffusion controlled precipitation reactions. In: *Scripta Materialia* 49 (2003), Nr. 10 SPEC., S. 927–932. – ISBN 3347682661

[47] Fick, Adolf: Ueber diffusion. In: *Annalen der Physik* 170 (1855), Nr. 1, S. 59–86. – ISSN 1521-3889

[48] Fischer, F. D. ; Reisner, G. ; Werner, E. ; Tanaka, K. ; Cailletaud, G. ; Antretter, T.: New view on transformation induced plasticity (TRIP). In: *International journal of plasticity* 16 (2000), Nr. 7, S. 723–748. – ISBN 0749-6419

[49] Gouveia, B.P.P.A. ; Rodrigues, J.M.C. ; Martins, P.A.F.: Ductile fracture in metalworking: experimental and theoretical research. In: *Journal of Materials Processing Technology* 101 (2000), Nr. 1-3, S. 52–63. – ISBN 0924-0136

[50] Gram, M. D. ; Wagoner, R. H.: Fineblanking of high strength steels: Control of material properties for tool life. In: *Journal of Materials Processing Technology* 211 (2011), Nr. 4, S. 717–728. – ISSN 09240136

[51] Greenwood, G. W. ; Johnson, R. H.: The Deformation of Metals Under Small Stresses During Phase Transformations. In: *Proceedings of the Royal Society of London A: Mathematical, Physical and Engineering Sciences* 283 (1965), jan, Nr. 1394, S. 403–422

[52] Heess, K.: *Edition expertsoft*. Bd. 76: *Mass- und Formänderungen infolge Wärmebehandlung von Stählen : Grundlagen - Ursachen - Praxisbeispiele*. 3., völlig. Renningen : expert-Verlag, 2007. – 84 S. S. – ISBN 978-3-8169-2678-8

[53] Hochholdinger, B.: Simulation des Presshärteprozesses und Vorhersage der mechanischen Bauteileigenschaften nach dem Härten. (2012), Nr. 20680, S. 235

[54] Hollox, G. E. ; VonBergen, R. T.: Distortion in the heat treatment of bearings. In: *Heat treatment of metals* 5 (1978), Nr. 2, S. 27–31. – ISSN 0305-4829

[55] Holzapfel, G.: Nonlinear solid mechanics: a continuum approach for engineering. In: *Vol. 24. Chichester. Wiley* (2000). ISBN 978-0471823193

[56] Hora, P.: Chapter 7. Simulation thermo- mechanisch gekoppelter Vorgänge. In: *Umforrmtechnik II Numerische Simulationsverfahren*. 2013

[57] Hougardy, H. P.: Umwandlung und Gefüge unlegierter Stähle. In: *Verlag Stahleisen, Dusseldorf* (1990)

[58] Hsu (Xu Zuyao), T. Y.: Additivity hypothesis and effects of stress on phase transformations in steel. In: *Current Opinion in Solid State and Materials Science* 9 (2005), Nr. 6, S. 256–268. – ISBN 1359-0286

[59] Inoue, T. ; Arimoto, K.: Development and implementation of cae system hearts for heat treatment simulation based on metallo-thermo-mechanics. In: *Journal of Materials Engineering and Performance* 6 (1997), Nr. 1, S. 51–60. – ISBN 1059-9495

[60] Inoue, T. ; Wang, Z.-G.: Coupling Phenomena between Stress, Temperature and Metallic Structures in the Process with Phase Transformation. In: *Linkoping University,* (1984), S. 298–310

[61] Ishida, K.: Calculation of the Effect of Alloying Elements on the Martensite-Start- Temperature in Steels. In: *Journal of Alloys and Compounds* 220 (1995), S. 126–131

[62] Johnson, William A. ; Mehl, Robert F.: Reaction Kinetics in processes of nucleation and growth. In: *Transactions of American Institute of Mining and Metallurgical Engineers* (1939), Nr. 135, S. 416–458

[63] Jung, M. ; Kang, M. ; Lee, Y.K.: Finite-element simulation of quenching incorporating improved transformation kinetics in a plain medium-carbon steel. In: *Acta Materialia* 60 (2012), Nr. 2, S. 525–536. – ISSN 13596454

[64] Kasatkin, O. G. ; Vinokur, B. B. ; Pilyushenko, V. L.: Calculation models for determining the critical points of steel. In: *Metal Science and Heat Treatment* 26 (1984), Nr. 1, S. 27–31. – ISSN 00260673

[65] Kenyeri, R. L. ; Foley, R. P.: Variations in hardness values and diameter change in 1018 and 4340 steel jominy bars. In: *20 th ASM Heat Treating Society Conference*, 2000, S. 470–478

[66] Kim, D. W. ; Cho, H. H. ; Lee, W. B. ; Cho, K. T. ; Cho, Y. G. ; Kim, S. J .. ; Han, H. N.: A finite element simulation for carburizing heat treatment of automotive gear ring incorporating transformation plasticity. In: *Materials and Design* 99 (2016), S. 243–253. – ISSN 18734197

[67] Kirkaldy, J S. ; Venugopalan, D: *Prediction of Microstructure and hardenability in Low Alloy Steels.* 1984

[68] Koistinen, D. P. ; Marburger, R. E.: A general equation prescribing the extent of the austenite-martensite transformation in pure iron-carbon alloys and plain carbon steels. In: *Acta Metallurgica* 7 (1959), Nr. 1, S. 59–60. – ISSN 0001-6160

[69] Kolmogorov, A.N.: On the Statistical Theory of the Crystallization of Metals. In: *Bulletin of the Academy of Sciences of the USSR* Vol. 1 (1937), Nr. Mathematics Series, S. 355–359

[70] Lankford, W.T. ; Snyder, S.C. ; Bauscher, J.A.: New Criteria for Predicting the Press Performance of Deep Drawing. In: *Trans. ASM* 42 (1950), S. 1197–1205

[71] Läpple, V.: *Wärmebehandlung des Stahls.* Verlag Europa-Lehrmittel, Nourney, Vollmer, 2010. – ISBN 9783808513101

[72] Le Masson, P. ; Loulou, T. ; Artioukhine, E. ; Rogeon, P. ; Carron, D. ; Quemener, J. J.: A numerical study for the estimation of a convection heat transfer coefficient during a metallurgical "Jominy end-quench" test. In: *International Journal of Thermal Sciences* 41 (2002), Nr. 6, S. 517–527. – ISSN 12900729

[73] Leblond, J. B. ; Devaux, J. ; Devaux, J. C.: Mathematical modelling of transformation plasticity in steels I: Case of ideal-plastic phases. In: *International Journal of Plasticity* 5 (1989), Nr. 6, S. 551–572. – ISBN 0749-6419

[74] Leblond, J.B. ; Devaux, J.: *A new kinetic model for anisothermal metallurgical transformations in steels including effect of austenite grain size.* 1984

[75] Lee, C. H. ; Bhadeshia, H. K. D. H. ; Lee, H. C.: Effect of plastic deformation on the formation of acicular ferrite. In: *Materials Science and Engineering A* 360 (2003), Nr. 1-2, S. 249–257. – ISBN 0921-5093

[76] Lee, M. ; Kim, S. ; Han, H. N. ; Jeong, W. C.: Implicit finite element formulations for multi-phase transformation in high carbon

steel. In: *International Journal of Plasticity* 25 (2009), sep, Nr. 9, S. 1726–1758. – ISSN 07496419

[77] Lee, S. J. ; Lee, Y. K.: Prediction of austenite grain growth during austenitization of low alloy steels. In: *Materials and Design* 29 (2008), Nr. 9, S. 1840–1844. – ISBN 0261-3069

[78] Leidenfrost, J. G.: On the fixation of water in diverse fire. In: *International Journal of Heat and Mass Transfer* 9 (1966), Nr. 11, S. 1153–1166. – ISBN 00179310 (ISSN)

[79] Lement, B. S.: *Distortion in tool steels.* American Society for Metals, 1959

[80] Li, B.: 6 Residual Stresses After Quenching. (1992)

[81] Li, M. V. ; Niebuhr, D.V. ; Meekisho, L. L. ; Atteridge, D. G.: A computational model for the prediction of steel hardenability. In: *Metallurgical and Materials Transactions B* 29 (1998), Nr. 3, S. 661–672. – ISSN 1073-5615

[82] List, Jocelyne: *Optische und virtuelle Kontrolle von Rückfederungseinflüssen.* 2012

[83] Liu, F. ; Sommer, F. ; Mittemeijer, E. J.: Determination of nucleation and growth mechanisms of the crystallization of amorphous alloys; application to calorimetric data. In: *Acta Materialia* 52 (2004), Nr. 11, S. 3207–3216. – ISBN 1359-6454

[84] Lusk, M. ; Jou, H.: On the rule of additivity in phase transformation kinetics. In: *Metallurgical and Materials Transactions A* 28 (1997), Nr. February, S. 287–291. – ISBN 1073-5623

[85] Macherauch, E.: Introduction t o residual stress. In: *Advances in Surface treatments* 4 (1987), S. 1–36

[86] Magee, C. L. ; Paxton, H. W.: Transformation Kinetics, Microplasticity and Aging of Martensite in FE-31 Ni. DTIC Document, 1966. – Forschungsbericht

[87] Majorek, A.: *Der Einfluss des Wärmeübergangs auf die Eigenspannungs- und Verzugsausbildung beim Abschrecken von Stahlzylindern in verdampfenden Flüssigkeiten.* Papierflieger, 1996. – ISBN 3931986349

[88] Malvern, L. E.: *Introduction to the Mechanics of a Continuous Medium.* 1969 (Monograph). – ISBN 0134876032

[89] Manopulo, N. ; Tong, L. ; Hora, P.: An ALE based FE formulation for the 3D numerical simulation of fineblanking processes. In: *AIP Conference Proceedings* 1353 (2011), Nr. 20045, S. 1209–1214. – ISBN 9780735408005

[90] Matsuzaki, A. ; Bhadeshia, H. K. D. H. ; Harada, H.: Stress affected bainitic transformation in a FeCSiMn alloy. In: *Acta Metallurgica Et Materialia* 42 (1994), Nr. 4, S. 1081–1090. – ISBN 0956-7151

[91] Moyer, J. M. ; Ansell, G. S.: The volume expansion accompanying the martensite transformation in iron-carbon alloys. In: *Metallurgical Transactions A* 6 (1975), Nr. 9, S. 1785–1791. – ISBN 0360-2133

[92] Narazaki, M. ; Kogawara, M. ; Shirayori, A. ; Fuchizawa, S.: Evaluation of heat transfer coefficient in Jominy End-quench test. In: *Proc. of the 4th Int. Conference on Quenching and the Control of Distortion*, 2003, S. 97–104

[93] Peterli, M.: *Numerische Simulation von Feinschneiden mit gekoppelter Wärmebehandlung und experimentelle Untersuchung von Feinschneidteilen.* 2013

[94] Peterli, M. ; Manopulo, N. ; Hora, P.: Numerical Heat Treatment Modelling of Fine Blanked Sheet Metal and Experimental Validation. In: *Key Engineering Materials* 651-653 (2015), jul, S. 1531–1536. – ISBN 978-3-03835-471-0

[95] Peterli, M. ; Truong, M. ; Manopulo, N. ; Hora, P.: A new optimization procedure for the accurate characterization of thermal phase transformation curves based on controlled quenching experiments. In: *MATEC Web Conf.* 80 (2016), S. 10010

[96] Pickering, F. B.: Transformation and hardenability in steels. In: *Climax Molybdenum* (1967), S. 109

[97] Piekarska, W. ; Kubiak, M. ; Saternus, Z.: Numerical Modelling of Thermal and Structural Strain in Laser Welding Process / Modelowanie Numeryczne Odkształceń Cieplnych I Strukturalnych W Procesie Spawania Techniką Laserową. In: *Archives of Metallurgy and Materials* 57 (2012), Nr. 4. – ISSN 2300-1909

[98] Porter, D. ; Easterling, K. E. ; Sherif, M. Y.: *Phase transformations in metals and alloys*. 3rd ed. Boca Raton, FL : CRC Press, 2009. – 520 S. S. – ISBN 978-1-4200-6210-6

[99] Porter, D. A. ; Easterling, K. E.: *Phase transformations in metals*. 1992

[100] Pumphrey, W. I. ; Jones, F. W.: Inter-relation of hardenability and isothermal transformation data. In: *ISIJ* 159 (1948), S. 137–144

[101] Rose, A.: Wärmebehandelbarkeit der Stähle. In: *Stahl u. Eisen* 85 (1965), S. 1229

[102] Rose, A.: Eigenspannungen als Ergebnis von Wärmebehandlung und Umwandlungsverhalten. In: *HtM* 21 (1966), Nr. 1, S. 1–5

[103] Rose, A. ; Wiest, P. ; Orlich, J.: *Atlas Zur Wärmebehandlung Der Sähle*. Vol. 2. Düsseldorf : Verlag Stahleisen M.B.H, 1973

[104] Scheil, E.: Die Berechnung der Anzahl und Größenverteilung kugelförmiger Kristalle in undurchsichtigen Körpern mit Hilfe der durch einen ebenen Schnitt erhaltenen Schnittkreise. In: *Zeitschrift für anorganische und allgemeine Chemie* 201 (1931), Nr. 1, S. 259–264. – ISSN 1521-3749

[105] Schröder, R. ; Scholtes, B. ; Macherauch, E.: Rechnerische und röntgenographische Analyse der Eigenspannungsausbildung in abgeschreckten Stahlzylindern. In: *HTM* 39 (1984), Nr. 6, S. 280–292

[106] Shipway, P. H. ; Bhadeshia, H. K. D. H.: The effect of small stresses on the kinetics of the bainite transformation. In: *Materials*

Science and Engineering A 201 (1995), Nr. 1-2, S. 143–149. – ISSN 09215093

[107] Simsir, C. ; Gür, C. H.: 3D FEM simulation of steel quenching and investigation of the effect of asymmetric geometry on residual stress distribution. In: *Journal of Materials Processing Technology* 207 (2008), Nr. 1-3, S. 211–221. – ISSN 09240136

[108] Simsir, C. ; Gür, C. H.: A FEM based framework for simulation of thermal treatments: Application to steel quenching. In: *Computational Materials Science* 44 (2008), Nr. 2, S. 588–600. – ISBN 0927-0256

[109] Sinha, A. K.: Defects and Distortion in Heat-Treated Parts. In: *Metallography* 4 (1991), S. 601–619. – ISSN 0036-8733

[110] Stefan, J.: *Über die Beziehung zwischen der Wärmestrahlung und der Temperatur.* 1879

[111] Steven, W. ; Haynes, A.: The temperature of formation of martensite and bainite in low-alloy steels. Some effects of chemical composition. In: *JISI* 183 (1956), S. 349

[112] Thelning, K. E.: *Steel and Its Heat Treatment.* Second edi. Butterworth & Co, 1984. – ISBN 9788578110796

[113] Totten, G. E.: *Steel heat treatment.* 2nd ed. Boca Raton : CRC, 2007 (Steel heat treatment handbook). – ISBN 978-0-824-72741-3

[114] Transvalor: *General Documentation - Metallurgy.* 2016

[115] Truong, M.: *Methodik zur Optimierung der thermischen Werkstoffdaten für die simulative Gefügevorhersage beim Härten von Stahl.* 2015

[116] Tszeng, T. C. ; Wu, W. T. ; Semiatin, L.: A sensitivity study of the process model for predicting the distortion during heat treating. ASM International, Materials Park, OH (United States), 1996. – Forschungsbericht

[117] Verein Deutscher Eisenhüttenleute: *SEP 1680: Aufstellung von Zeit-Temperatur-Umwandlungsschaubildern für Eisenlegierungen.* 1990

[118] Verein Deutscher Eisenhüttenleute: *SEP 1681: Guidelines for preparation, execution and evaluation of dilatometric transformation tests on iron alloys.* 1998

[119] Videau, J.-C. ; Cailletaud, G. ; Pineau, A.: Modélisation des effets mécaniques des transformations de phases pour le calcul de structures. In: *Journal de Physique III, supplément Colloque C3* 4 (1994), S. 227–232. – ISSN 1155-4339

[120] Wang, J. ; Wolk, P. J. van der ; Zwaag, S. van der: *Determination of martensite start temperature in engineering steels Part I. empirical relations describing the effect of steel chemistry.* 2000

[121] Wesner, T.: *Virtuelle und experimentelle Methoden zur Voraussage des Prozessfensters beim Feinschneiden*, ETH Zürich, Dissertation, 2016

[122] Wriggers, P.: *Nichtlineare finite-element-methoden.* 2001. – ISBN 9783540677475

[123] Wyss, U.: Überblick über die wichtigsten Gesetzmäßigkeiten der Maßänderung von Werkstücken bei der Wärmebehandlung. In: *Die Wärmebehandlung von Bau- und Werkzeugstählen, Bd. II.* MICROTECNIC Scriptar S.A:, 1971, Kap. 22

[124] Yang, H. S. ; Bhadeshia, H. K. D. H.: Austenite grain size and the martensite-start temperature. In: *Scripta Materialia* 60 (2009), Nr. 7, S. 493–495. – ISBN 13596462

[125] Yu, H. J. ; Wolfstieg, U. ; Macherauch, E.: Calculation of residual-stresses with a special finite-element program. In: *Archiv fur das Eisenhuttenwesen* 49 (1978), Nr. 10, S. 499–504. – ISSN 0003-8962

curriculum vitae

personal details

surname and name:	**Maurice Nadim Peterli**
birth date:	13.08.1987
place of birth:	Basel, Switzerland
nationality:	Swiss

education

2013 – 2017	Doctoral student *Institute of Virtual Manufacturing, ETH Zurich, CH*
2011 – 2013	Master of science in mechanical engineering *ETH Zurich, CH*
2006 – 2011	Bachelor of science in mechanical engineering *ETH Zurich, CH*
2001 – 2006	Matura with core subject mathematics and physics *Gymnasium Kirschgarten Basel, CH*

professional experience

04/2013 – 04/2017	Scientific employee *Institute of Virtual Manufacturing, ETH Zurich, CH*
01/2012 – 09/2012	Industrial placement in process technology and control *Dr. Ing. h.c. F. Porsche AG, Stuttgart, DE*
02/2011 – 12/2011	Scientific assistant *Institute of Virtual Manufacturing, ETH Zurich, CH*
06/2001 – 12/2001	Industrial placement *Sultex AG, Zuchwil, CH*